

**Dissertation submitted to the Combined Faculties for the Natural  
Sciences and for Mathematics  
of the Ruperto–Carola University of Heidelberg, Germany  
for the degree of  
Doctor of Natural Sciences**

presented by

Diplom-Physiker: Simon Aigner

born in: Regensburg (Bavaria, Germany)

Oral examination: 31.10.2007

# **Magnetic Field Microscopy using Ultracold Atoms**

Referees: Prof. Dr. Jörg Schmiedmayer  
Priv. Doz. Dr. Maarten DeKieviet

## Zusammenfassung / Abstract

**Magnetfeldmikroskopie mit ultrakalten Atomen.** In dieser Arbeit werden die Ergebnisse der ersten systematischen Anwendung von Magnetfeldmikroskopie mit ultrakalten Atomen vorgestellt. Die Eigenschaften des Ladungstransports in polykristallinen Dünnschicht-Golddrähten werden in einem bisher nicht zugänglichen Regime untersucht. Mit Hilfe des Feldsensors auf der Basis ultrakalter Atome wird eine mikroskopische Abbildung von Richtungsänderungen des lokalen Stromverlaufs über Längenskalen zwischen  $10\mu m$  und  $600\mu m$  bei einer Winkelauflösung besser als  $10^{-5}\text{rad}$  erreicht. Die Messungen zeigen eine Orientierungspräferenz der Richtungsfluktuationen, welche innerhalb eines Ohmschen Defektmodells erklärt wird. Die Absolutgröße der Fluktuationen (rms Winkelfluktuationen zwischen  $60\mu rad$  und  $160\mu rad$ ) wird durch unterschiedliche Beiträge von Oberflächendefekten und solche des Volumenmaterials interpretiert. Die notwendige Methodik zur Implementierung und Interpretation einer quantitativen Magnetfeldmikroskopie mit ultrakalten Atomen wird eingehend dargestellt.

**Magnetic Field Microscopy using Ultracold Atoms.** In this thesis the results of the first systematic application of magnetic field microscopy using ultracold atoms are presented. The properties of charge transport in thin film polycrystalline gold wires are examined in a previously not accessible regime. The field sensor based on ultracold atoms facilitates a microscopic mapping of directional fluctuations in the local current direction at an angle resolution of  $10^{-5}\text{rad}$  over length scales between  $10\mu m$  and  $600\mu m$ . The measurements show an orientational preference in the directional fluctuations which is explained within an ohmic defect model. The absolute magnitude of the fluctuations (rms angle fluctuations between  $60\mu rad$  and  $160\mu rad$ ) are interpreted by different contributions of surface and bulk defects. The methods that are necessary for the implementation and interpretation of a quantitative magnetic field microscopy using ultracold atoms are described thoroughly.

# Contents

<b>1</b>	<b>Overview</b>	<b>1</b>
1.1	Magnetometry and Electronic Transport . . . . .	1
1.2	Magnetically Trapped Ultracold Atoms as a Sensor . . . . .	5
1.3	Outline of this Thesis . . . . .	9
<b>2</b>	<b>Transport through Thin Metal Films</b>	<b>13</b>
2.1	Introduction . . . . .	13
2.2	Preferred $45^\circ$ Fluctuations . . . . .	15
2.3	The Origin of Fluctuations . . . . .	22
2.3.1	Exact Statements from Qualitative Scans . . . . .	23
2.3.2	Surface Corrugations and Bulk Defects . . . . .	25
2.3.3	Real Space Correlation Based on Surface Roughness . . . . .	31
2.3.4	Power Spectrum . . . . .	33
2.4	Conclusion . . . . .	36
2.5	Experimental Scan Parameters and error Estimates . . . . .	37
2.5.1	Temperature measurements . . . . .	38
2.5.2	Positioning and Height calibration . . . . .	42
2.5.3	Magnetic Field . . . . .	50
2.6	Appendix . . . . .	51
2.6.1	Magnetic field of a rectangular wire . . . . .	51
2.6.2	Fourier Spectrum . . . . .	52
2.6.3	Gaussian Noise . . . . .	53
2.6.4	Error weighted mean value . . . . .	53
<b>3</b>	<b>Current Imaging and Defect Sensing</b>	<b>56</b>

3.1	Introduction . . . . .	56
3.2	Magnetic Field Propagation . . . . .	57
3.2.1	Wavepropagation: Near and Far Field . . . . .	57
3.2.2	Uniqueness of the Effective Current Reconstruction . . . . .	61
3.3	Magnetometric Defect Detection . . . . .	63
3.3.1	General properties . . . . .	63
3.3.2	Surface Defects . . . . .	67
3.3.3	Bulk Defects . . . . .	72
3.3.4	Comparison of Bulk and Surface Models . . . . .	74
3.4	Appendix . . . . .	76
3.4.1	Current-flow Around a Cylindrical Defect . . . . .	76
<b>4</b>	<b>Basic measurements on atoms</b>	<b>79</b>
4.1	Introduction . . . . .	79
4.2	Detection . . . . .	81
4.3	Density distribution . . . . .	87
4.4	Time of flight measurements . . . . .	89
4.4.1	Expansion of a thermal Cloud . . . . .	89
4.4.2	Expansion of a Thomas-Fermi Condensate . . . . .	90
4.5	Oscillations . . . . .	93
4.5.1	Center of mass oscillation . . . . .	93
4.5.2	Width oscillation . . . . .	97
4.6	Rf-Spectroscopy . . . . .	99
<b>5</b>	<b>Imaging Close to a Mirror</b>	<b>103</b>
5.1	Introduction . . . . .	103
5.2	Absorption Imaging Close to a Mirror . . . . .	105
5.3	Extraction of the Cloud Position . . . . .	111

5.4	Appendix . . . . .	114
5.4.1	Wavefront-Propagation . . . . .	114
5.4.2	Reflection by a Corrugated Mirror . . . . .	115
<b>6</b>	<b>Magnetic Trapping and Spin Dynamics</b>	<b>118</b>
6.1	Classical Motion of a Spin Particle . . . . .	118
6.2	The effective potential . . . . .	120
6.2.1	Adiabatic Potential . . . . .	120
6.2.2	Floquet Potential . . . . .	121
6.2.3	Computation of quasi energies . . . . .	123
6.2.4	Resonant Rf Potential . . . . .	124
6.3	Gradient Fields On An Atom Chip . . . . .	127
6.3.1	Symmetries the field . . . . .	127
6.4	The Stern Gerlach Beam Splitter . . . . .	130

---

# 1 Overview

---

## 1.1 Magnetometry and Electronic Transport

Any electric current distribution necessarily produces a magnetic field around it. The spatially resolved acquisition of field data is therefore exploited in many different environments for the non-invasive investigation of charge transport. The range of systems being approached by this technique covers many orders of magnitude in both spatial size and field magnitude.

Changes in the earth's magnetic field on a scale of 250nT in five years [1] accompany the evolution of the inner liquid core. Processes in the human body from muscle contraction to brain activity can be traced by minute magnetic fields that range between  $(10^{-5} - 10^1)$ nT[2]. The extension down to microscopic scales is commonly implemented along the scanning microscope paradigm. Miniature Superconducting Quantum Interference Devices (SQUIDS) [3] and Giant Magneto Resistance (GMR) sensors [4, 5] have been used as precision sensors for electronic device testing and failure analysis. In this work, a recently demonstrated [6, 7] technique has been used where trapped ultracold atoms are used as a scanning sensor. The method has been applied systematically to tackle the problem of electronic transport in thin polycrystalline gold wires.

Metallic thin films are a well established testing ground for fundamental questions of transport and scattering in the presence of static defects [8, 9, 10]. As can be seen in figure 1.1 there are two basic kinds of defects: grains inside the bulk material and surface roughness. The classical experimental technique towards the characterization of this system has been the measurement of the low temperature residual resistivity

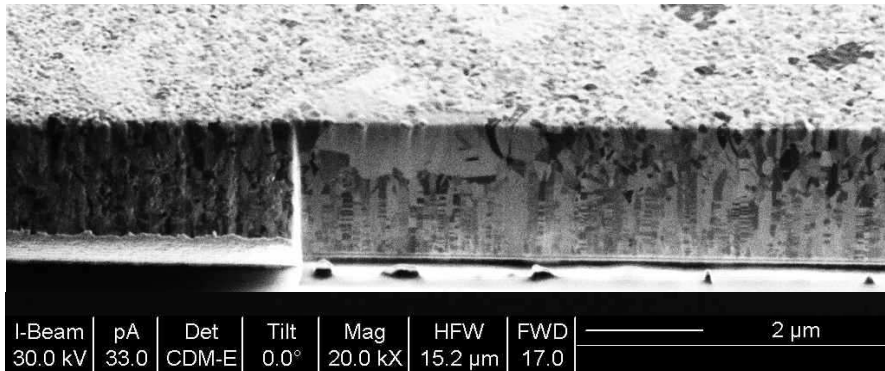


Figure 1.1: *Grain orientation and surface structure in a polycrystalline gold wire [11].* The picture shows a view onto the side of a typical polycrystalline gold wire as used in this work. In the right half of the picture the edge has been polished by a focused ion beam. For imaging, a focused ion beam of lower energy has been scanned over the sample and the backscattered electrons are focused to yield the image. The contrast reflects the local orientation of the gold grains. In the lower part of the wire up to a height of approximately  $1\mu m$ , the film grows up in columns. Above this height, larger three dimensional grains start to form which are also visible on the surface.

[12]. Scattering by phonons, which usually makes the dominant contribution to the resistivity at room temperature, is frozen out and the remaining resistance gives the overall contribution of static defect scattering. The first detailed microscopic description, of the scattering process at single grains, has been given by Landauer [13] and subsequently triggered the very successful field of transport in mesoscopic systems. He introduced the idea, that a charge dipole builds up around a static scatterer and the electric field caused by this dipole in turn allows the current to pass around the defect. This dipole charge can be directly resolved in scanning tunnelling potentiometry [14] by the accompanying step of the electrostatic potential.

Despite the ongoing interest in the field, no measurement of the primary transport quantity, namely the current density itself has been made until today. Long range correlations in the current flow, which extend well beyond the scattering source have never been addressed. Microscopy with magnetically trapped ultracold atoms offers exactly this possibility.

In the absence of any defect, the current through a straight wire just follows the wire direction. A defect however, causes a small deflection of the current density. Figure 1.2 schematically depicts the current distribution around a small disc shaped defect. The current component that is perpendicular (transverse) to the incident current direction is that quantity which is most directly related to the presence of the

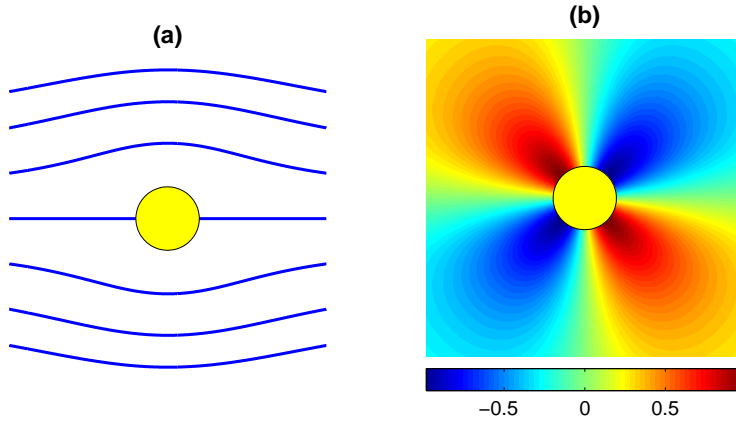


Figure 1.2: *Current flow around a small defect.* (a) Streamlines of the current flow around the defect. The current flows from left to right. When impinging on the defect in the center, a charge dipole builds up that causes a small deviation in the current density. (b) The current component perpendicular to the incident current flow has the typical behavior of an electric dipole field. This component vanishes in the absence of a defect.

defect. It is proportional to the change in conductivity and vanishes in the absence of a defect. The magnetic field that is generated directly above the wire exactly follows this characteristic behavior of the current density. For a defect in the  $x$ - $y$  plane and a mean current flowing along the  $x$ -direction the magnetic field component along the wire  $B_x(x, y)$  is approximately given by  $B_x(x, y) = \mu_0 j_y(x, y) d/2$ . This approximation is valid in the thin film limit, where the thickness of the film  $d$  is small. If also  $B_x$  is small, the change of the magnetic field direction is given by the angle

$$\beta(x, y) \approx B_x(x, y)/B_0 = j_y(x, y)/j_0 \quad (1.1)$$

where  $B_0$  and  $j_0$  are the absolute values of the field and the current density in the absence of a defect.

In order to apply this magnetic defect detection in the case of a thin gold film, the sensing scheme has to comply to several restrictive conditions. The two most important are the need for an angle resolution of  $\beta$  which has to be on the order of  $10^{-5}$  rad and a spatial resolution preferably in the micrometer range.

In this work, gold films with a thickness of  $d = 250$  nm and  $d = 2$   $\mu$ m have been used. In order to avoid local heating in the material, which results from ohmic losses and the successive material transport by electro-migration, the current density has to be kept significantly below  $10^{11}$  A/m<sup>2</sup>. For a save value of  $10^{10}$  A/m<sup>2</sup>, the absolute field amplitude above the unperturbed film ranges therefore between 16G and 130G

( $1G = 10^{-4}T$ ). The expected variations in the field component perpendicular to this main field are then between  $160\mu G$  to  $1.3mG$ . In principle, there are at least two state of the art detectors that are capable of achieving a field resolution in the  $100\mu G$  regime at the required spatial resolution. Figure 1.3 shows a comparison of several different detector types. When operated at a bandwidth of 1 Hz, at least SQUID and

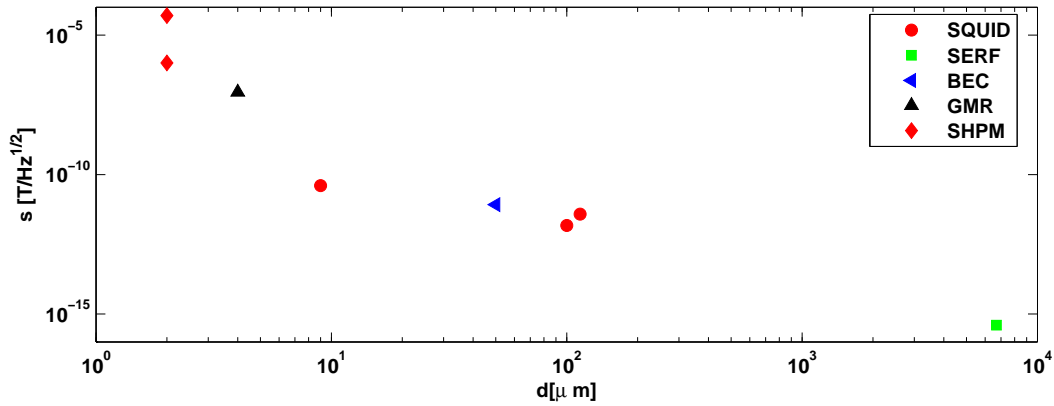


Figure 1.3: *Sensitivity versus spatial resolution in magnetometry.* The sensitivity  $s$  denotes the magnetic field standard deviation per unit bandwidth.  $d$  is the effective sensor diameter and therefore the maximal obtainable spatial resolution. The values for the scanning SQUID microscope (SQUID) are taken from [15, 16, 17]. For the optical magnetometer (SERF) from [18], for optical magnetometry at a spinor Bose Einstein Condensate (BEC) from [19], for commercially available giant magnetoresistive sensors (GMR) from [20] and for room temperature and cold Scanning Hall Probe Microscopy (SHPM) from [22, 23].

GMR sensors should be capable of the necessary field sensitivity. However, in order to achieve the required angle resolution the stability of the sensor orientation has to be significantly better than the required  $10^{-5}\text{rad}$  which is at least a challenging task. In the present work, the intrinsic stability of magnetic traps has been used to avoid this problem. The basic principle is presented in the following section.

## 1.2 Magnetically Trapped Ultracold Atoms as a Sensor

Ultracold  $^{87}\text{Rb}$  atoms in their  $F = 2$  groundstate have a magnetic moment of  $\mu = \mu_B$ . By this magnetic moment, the atoms couple to a magnetic field by the typical dipole potential  $V = \mu_B |\mathbf{B}|$  (this Formula assumes adiabatic spin dynamics). In magnetic wire traps, implemented on atom chips [24, 25], the gradient field around the current through a straight wire is used, to build a confining potential for the atoms. When the homogenous part of the magnetic field is compensated at some specific position above the wire center by the help of an additional homogenous bias field, the remaining quadrupole provides a cylindrically symmetric confinement in the plain perpendicular to the wire axis. This principle is shown for a wire of circular cross section in figure 1.4. In order stay in the regime of adiabatic spin dynamics,

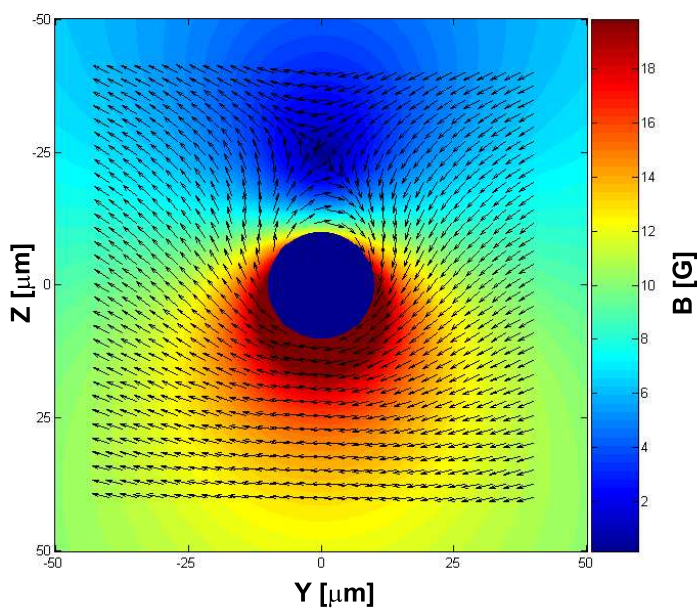


Figure 1.4: *Magnetic wiretrap*. The picture shows a magnetic trap above a wire of circular cross section. The absolute field value is encoded by the colormap. The orientation of the field, as indicated by the arrows, shows the typical quadrupole character around the trap center at  $z = -25\mu\text{m}$ ,  $y = 0$ .

a homogenous field  $B_i$  is added along the wire axis to avoid a zero in the absolute

value of the magnetic field. The total potential in the vicinity of the minimum is then given by

$$V \approx \mu_B B_i \left( 1 + \frac{1}{2} \frac{g^2}{B_i^2} r^2 \right) = \frac{m}{2} \omega^2 r^2 \quad (1.2)$$

. In this equation,  $g$  denotes the gradient of the magnetic field along one of the quadrupole's main axes,  $r = \sqrt{(y - y_0)^2 + (z - h)^2}$  is the distance from the trap center at  $(y = y_0, z = h)$  and  $\omega = \sqrt{\mu_B / B_i m} g$  is the harmonic oscillator frequency. Ultracold atoms only occupy a narrow range around the minimum of the potential so that the harmonic approximation around the trap center is usually adequate.

A perturbative analysis, of how the potential changes with small variations in the magnetic trapping field, reveals that wiretraps may be operated as highly directional field sensors. If a small variation  $\Delta \mathbf{B} = (\Delta B_x, \Delta B_y, \Delta B_z)$  is added to the trapping field, the potential changes to leading order at the trap center by  $\Delta V = \mu_B \Delta B_x + O(\Delta B^2 / B_0^2)$ . For typical variations of  $\Delta B / B_0 \approx 10^{-6} - 10^{-4}$  which have been encountered in the measurements of this thesis, the quadratic term in the expansion can be neglected, and all variations in the potential are directly related to a change of the magnetic field's x-component [26]. Under these conditions, the total potential is given by

$$V = \frac{m}{2} \omega^2 ((y - y_0)^2 + (z - h)^2) + \mu_B B_x(x, y_0, h) \quad (1.3)$$

When such a trap is filled up by ultracold atoms, the cloud typically extends over several  $100 \mu m$  along the x-direction and about  $1 \mu m$  in the y-z plane.

Variations due to the field  $B_x(x)$  cause small modulations in the density along the long axis of the cloud. In a non-degenerate ideal gas the atoms occupy a potential according to the Boltzmann distribution  $\rho \propto \exp -V/k_B T$ . An illustrative example of this relation is depicted schematically for a corrugated potential in figure 1.5. The sensitivity of the atomic density to small variations in the potential is set by the thermal energy  $k_B T$ . More quantitatively, a small variation in the field  $\Delta B_x$  causes a relative change of the density  $\Delta \rho$  by

$$\frac{\Delta \rho}{\rho} = \frac{\mu_B}{k_B T} \Delta B_x \quad (1.4)$$

. It is apparent, that for atoms at room temperature magnetic fields of reasonable size have nearly no influence on the density. The enormous variation of  $1 T$  causes a relative change of only  $\Delta \rho / \rho = 2 \cdot 10^{-3}$  in the density. At  $100 nK$  however, which is the typical temperature scale for ultra cold atoms, the situation is much more favorable. The sensitivity increases by more than nine orders of magnitude to  $\Delta \rho / \rho = 6 \cdot 10^6$ .

Once the field variation  $\Delta B_x$  is translated to a density variation it can be read out optically by absorption imaging. When illuminated by resonant laser light, the atomic distribution casts a shadow, where the absorption signal is readily converted

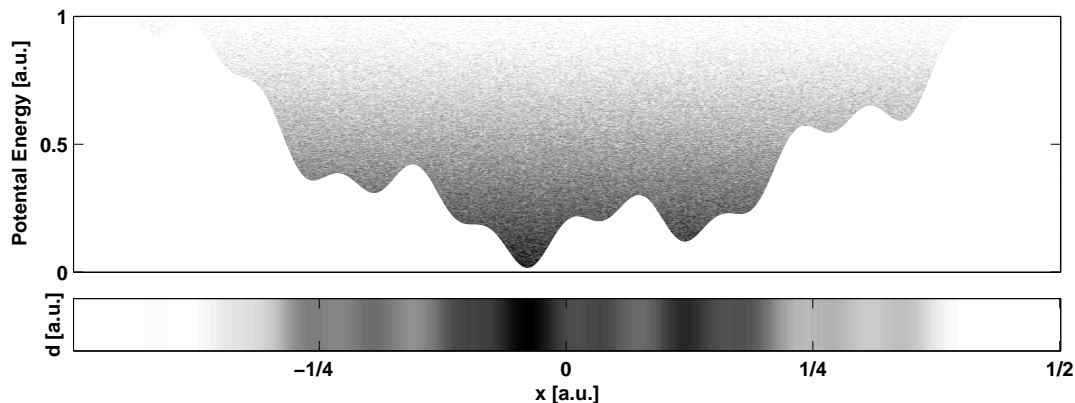


Figure 1.5: *Atoms in a random potential.* The upper panel shows, how an atomic cloud fills up a potential according to the Boltzmann distribution. The gray level is proportional to the number of atoms. The lower bar plot shows the shadow that such a distribution would cast, when illuminated by resonant laser light from the top.

to a particle density. By scanning the trap center position  $(y_0, h)$  over the wire surface, the magnetic field component along the wire axis  $B_x(x, y_0, h)$  can be mapped out via the resulting changes in the density. An example scan implementing this scheme is depicted in figure 1.6.

In conclusion, magnetically trapped atoms are uniquely adapted to the measurement of small directional variations of the magnetic field. In comparison to other techniques, no active feedback is required to keep the sensor at its working point. Cold atoms automatically gather at the trap center. There, the potential is intrinsically sensitive to variations of the field component along the wire direction only. This assures the high angular sensitivity and stability.

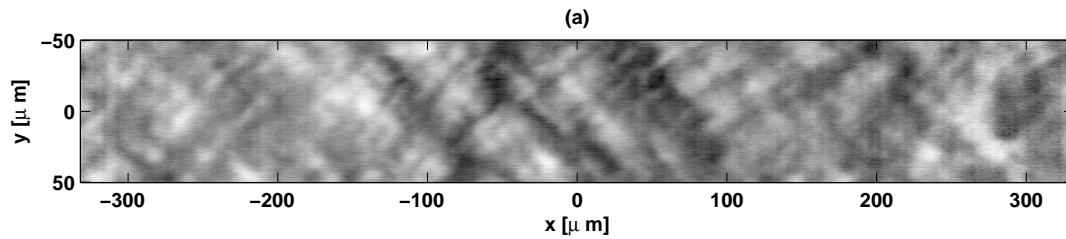


Figure 1.6: *Scan example above a thin film sample wire.* The pictures show sequentially acquired density measurements,  $3.5\mu m$  above a  $250nm$  thick wire, carrying a current of  $180mA$ . The measurements have been performed using atomic clouds at a temperature of approximately  $140nK$ . The gray level is proportional to the density. The picture is composed from 200 single rows that each present a separate measurement. The variations in the density correspond to an rms angle deviation in the current density of  $7 \cdot 10^{-4}rad$

## 1.3 Outline of this Thesis

In order to apply the ultracold magnetometry method, introduced in the last section, to the investigation of the current flow in polycrystalline gold films, precision fabricated thin film wires have been integrated on an atom chip. This chip has been realized in a collaboration with Ron Folman at the Weiss Family Laboratory for nano-Scale Systems, Ben Gurion University, Israel. A picture of the mounted chip, before its integration into the cold atoms measurement setup is shown in figure 1.7.

The remaining part of this thesis describes measurements on this sample chip, their interpretation and the detailed methodology for the implementation of a quantitative magnetic field microscopy using ultracold atoms. The chapters are organized as follows.

**Chapter two** presents the main experimental results of a systematic study on the current flow deviations in thin film metallic gold wires. The field scans are analyzed phenomenologically and interpreted with respect to different static defect scenarios of the wires. A non trivial symmetry is found in the fluctuation patterns which is explained in the context of an ohmic conductor. To the knowledge of the author these measurements present the first application of an atom chip technique to a problem outside the field of atomic physics.

**Chapter three** covers a systematic treatment of the imaging theory of magnetic fields on the basis of wave propagation in the near field regime. After the general considerations on field propagation, the theoretical background for the analysis and interpretation of current flow fluctuations in thin films is given.

**Chapter four** gives an overview of the experimental techniques that have been used directly or indirectly for the characterization and manipulation of the cold atomic clouds. They present a standard toolbox in the work with ultracold atoms.

**Chapter five** examines in detail the process of absorption imaging close to a metallic surface. This technique is fundamental for the precise positioning of the atomic sensor above the current carrying layer. Fundamental difficulties that are caused by the presence of the mirror plane are analyzed.

**Chapter six** finally is a loose collection of topics related to spin dynamics and magnetic trapping. This chapter is widely independent of the rest of this work.

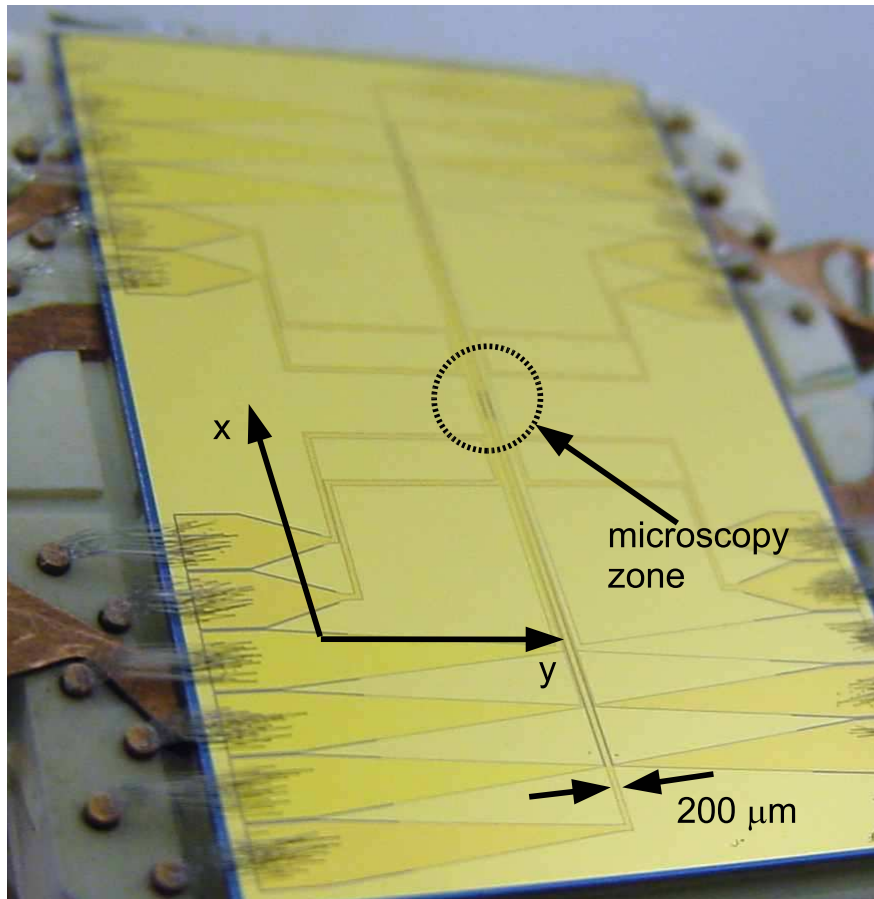


Figure 1.7: *Mounted atom chip, hosting the test wires.* The chip consists of micro-fabricated gold wires of different crystalline grain size (40 nm and 120 nm) and thickness ( $2\ \mu\text{m}$  and  $250\ \text{nm}$ ). The sample region is enclosed within the circled region. The wires that have been used for the precision scans presented here, are straight over at least 1 cm along the x-direction.

# Bibliography

- [1] Mc Lean, S. et al. The US/UK World Magnetic Model for 2005-2010. *NOAA Technical Report NESDIS/NGDC-1* (2004)
- [2] Wikswo, J.P. SQUID Magnetometers for Biomagnetism and Nondestructive Testing: Important Questions and Initial Answers. *IEEE Trans. Appl. Supercond.* **5**, 74 (1995)
- [3] Chatrathorn, S. et al. Scanning SQUID microscopy of integrated circuits. *Appl. Phys. Lett.* **76**, 2304 (2000)
- [4] Schrag, B.D. Gang, X. Submicron electrical current density imaging of embedded microstructures. *Appl. Phys. Lett.* **82**, 3272 (2003)
- [5] Schrag, B.D. et al. Current mapping and pinhole imaging in magnetic tunnel junctions via scanning magnetic microscopy. *Appl. Phys. Lett.* **84**, 2937 (2003)
- [6] Wildermuth, S. et al. Bose-Einstein condensates: Microscopic magnetic-field imaging. *Nature* **435**, 440 (2005)
- [7] Wildermuth, S. et al. Sensing electric and magnetic fields with Bose-Einstein condensates. *Appl. Phys. Lett.* **88**, 264103 (2006)
- [8] Sondheimer, E.H. The mean free path of electrons in metals. *Adv. Phys.* **1**, 1 (1952)
- [9] Chambers, R.G. The Conductivity of Thin Wires in a Magnetic Field. *Proc. R. Soc. London, Ser. A* **202**, 378 (1950)
- [10] Mayadas, A.F. Shatzkes, M. Electrical-Resistivity Model for Polycrystalline Films: the Case of Arbitrary Reflection at External Surfaces. *Phys. Rev. B* **1**, 1382 (1970)
- [11] The picture has been acquired by Henri Lezec in a collaboration with the ISIS, Universite Luis Pasteur, Strasbourg, France.
- [12] Steinhögl, et al. Size-dependent resistivity of metallic wires in the mesoscopic range. *Phys. Rev. B* **66**, 075414 (2002)
- [13] Landauer, R. Spatial Variation of Currents and Fields Due to Localized Scatterers in Metallic Conduction. *IBM J. Res. Dev.* **1**, 223 (1957)
- [14] Schneider, M.A., et al. Current transport through single grain boundaries: A scanning tunneling potentiometry study. *Appl. Phys. Lett.* **69**, 1327 (1996)

- [15] Kirtley, J.R. et al. High-resolution scanning SQUID microscope. *Appl. Phys. Lett.* **66**, 1138 (1994)
- [16] Lee, T.S. Dantsker, E. Clarke, J. High-transition temperature superconducting quantum interference device microscope. *Rev. Sci. Instr.* **67**, 4208 (1996)
- [17] Fong, L.E. et al. High-resolution room-temperature sample scanning superconducting quantum interference device microscope configurable for geological and biomagnetic applications. *Rev. Sci. Instr.* **76**, 053703 (2005)
- [18] Kominis, I.K. et al. A subfemtotesla multichannel atomic magnetometer. *Nature* **422**, 596 (2003)
- [19] Vengalattore, M. et al. High-Resolution Magnetometry with a Spinor Bose-Einstein Condensate. *Phys. Rev. Lett.* **98**, 200801 (2007)
- [20] Micro Magnetics Datasheet to the STJ-001 sensor *Micromagnetics Inc.*, 421 Carrant Road, Fall River MA 02720, <http://www.micromagnetics.com/>
- [21] Fagaly, R.L. Superconducting quantum interference device instruments and applications. *Rev. Sci. Instr.* **77**, 101101 (2006)
- [22] Pross, A. et al. Second-generation quantum-well sensors for room-temperature scanning Hall probe microscopy. *J. Appl. Phys.* **97**, 096105 (2005)
- [23] Brook, A.J. et al. Integrated piezoresistive sensors for atomic force-guided scanning Hall probe microscopy. *Appl. Phys. Lett.* **82**, 3538 (2003)
- [24] Folman, R. et al. Microscopic Atom Optics: From Wires to an Atom Chip. *Adv. At. Mol. Opt. Phys.* **48**, 263 (2002)
- [25] Fortagh, J. Zimmermann, C. Magnetic microtraps for ultracold atoms. *Rev. Mod. Phys.* **79**, 235, (2007)
- [26] Wang, D.W. Lukin, M.D. Demler, E. Disordered Bose-Einstein Condensates in Quasi-One-Dimensional Magnetic Microtraps. *Phys. Rev. Lett.* **92**, 076802 (2004)

---

# 2 Transport through Thin Metal Films

---

## 2.1 Introduction

Thin metal films are the classic environment for studying the effect of geometric constraints[1, 2] and crystal defects [3, 4] on the transport of electrons. At ambient temperature, perpetual scattering by lattice vibrations (phonons) quickly diffuses the electronic motion so that dominant effects of static defects are usually observed only on a length-scale of several nanometers [5, 6]. Here, using ultracold atom magnetometry[7] it is shown that correlations in the current flow through polycrystalline metal films exist even at room temperature and at length scales that are orders of magnitude larger than the diffusion length or the grain size. Despite the random structure inside the films, fluctuations in the local current direction form patterns oriented at  $45^\circ$  relative to the mean current flow, independent of film thickness or grain size. The amplitude of the current direction fluctuations scales contrary to what is naively expected. The thinnest film with the largest grains shows the smallest directional variations, much too small to be explained by the measured top surface roughness of the gold film alone. This study shows that directly probing the spatial current flow pattern in thin or quasi-2D structures by ultracold atom magnetometry can find long range current correlations. It might be able to shed new light on the interplay between disorder and coherent transport in a variety of other systems, ranging from high- $T_c$  superconductors[8] to 2D electron gases[9] and nanowires[10].

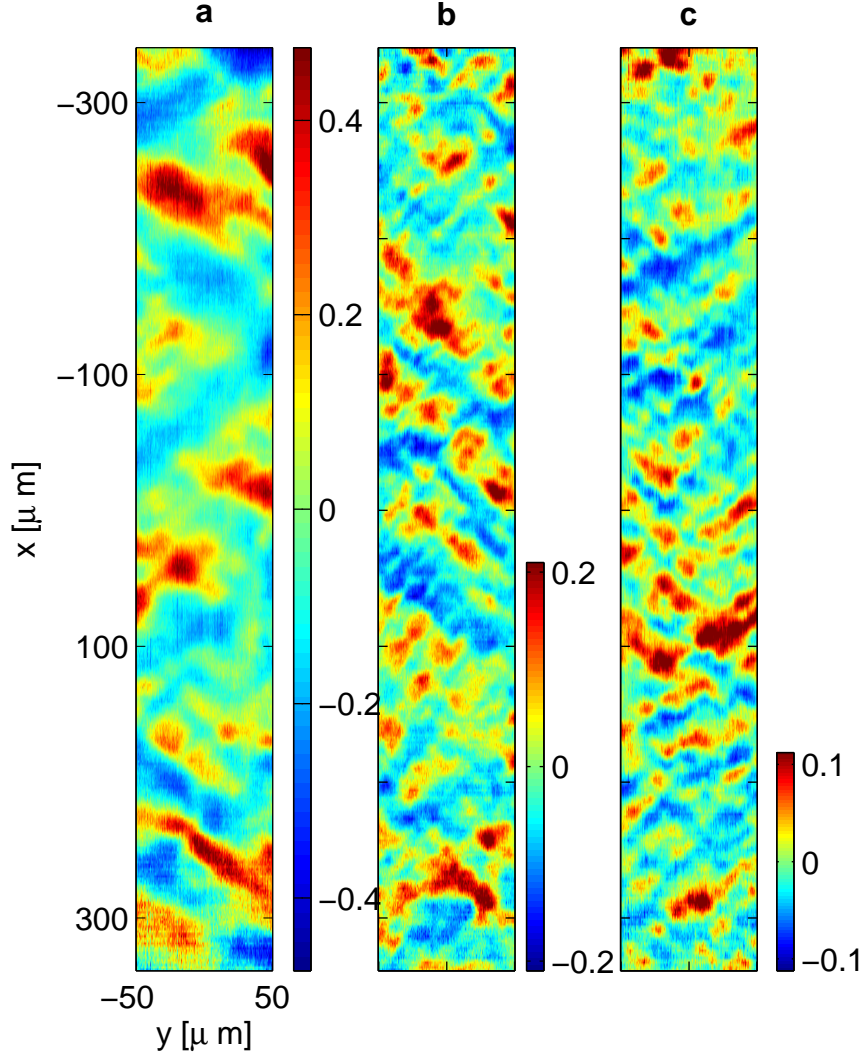


Figure 2.1: Magnetic field angle fluctuations  $\beta$ [mrad] above three different polycrystalline gold films. This angle directly maps the current direction within the films at a resolution of approximately  $8\mu m$ . The magnetic field direction is measured at a distance above the surface of  $z_{\mathbf{a}} = (3.5 \pm 0.8)\mu m$ ,  $z_{\mathbf{b}} = (3.8 \pm 0.4)\mu m$  and  $z_{\mathbf{c}} = (4.0 \pm 0.6)\mu m$  for films **a** to **c** respectively. The pictures show the central  $680\mu m \times 100\mu m$  of each of the  $200\mu m$ -wide gold wires.

## 2.2 Preferred 45° Fluctuations

In a perfectly straight wire that is free from structural defects the DC current strictly follows the wire direction. The magnetic field that accompanies this current is contained in the plane perpendicular to the wire. However, an obstacle that causes the current to change its direction will also locally rotate the magnetic field by an angle  $\beta$  in the plane parallel to the wire. Ultracold atom magnetometry allows a very sensitive microscopy of this angle  $\beta$  with  $\mu rad$  resolution. This allows to study minute current direction variations with  $\mu m$  spatial resolution over  $mm$  length scales. In this work, this technique is applied to study the current deflection in three different precision fabricated polycrystalline gold wires[11] with a rectangular cross section of  $200\mu m$  width, different thicknesses and crystalline grain size, as summarized in table 2.1 The measured maps of the magnetic field angle  $\beta(x, y) = \delta B_x(x, y)/B_y$  are

wire	<b>a</b>	<b>b</b>	<b>c</b>
thickness $H$ [ $\mu m$ ]	2.0	0.28	0.25
grain size [ $nm$ ]	40	40	120
$\delta z^{rms}/H[10^{-3}]$	0.62	1.8	2.0
$\beta^{rms}$ [ $\mu rad$ ]	157	82	58

Table 2.1: *Sample wire properties* The standard variations of the height corrugation  $\delta z^{rms}$  and the angle fluctuations  $\beta^{rms}$  have been computed for  $k$  vectors within  $2\pi/250\mu m < |\mathbf{k}| < 2\pi/10\mu m$  (See section 2.6.2 for details on the Fourier transform).

shown in figure 2.1.

The two main observations are: First, there is a peculiar tendency to form elongated regions inclined by  $\pm 45^\circ$  to the wire axis. This orientational preference is present in all the measurements, independent of wire thickness or grain size. In order to quantify the angular preference of the measured magnetic field patterns, the normalized angular power spectrum  $p(\theta) = \int dk k |\beta(k, \theta)|^2 / \max(p)$  has been analyzed. Figure 2.2 clearly shows the preference of features oriented at angles of  $\pm 45^\circ$  for all three wires. As will be shown, this correlation is not the result of a structural preference but of selective scattering at an isotropic distribution. Second, a significant difference in the magnitude and spectral composition of the magnetic field variations above wires with different thicknesses are observed. The magnitude of the fluctuations scales contrary to the magnitude of the surface corrugations relative to the thickness (table 2.1). The 280 nm thin film with the largest

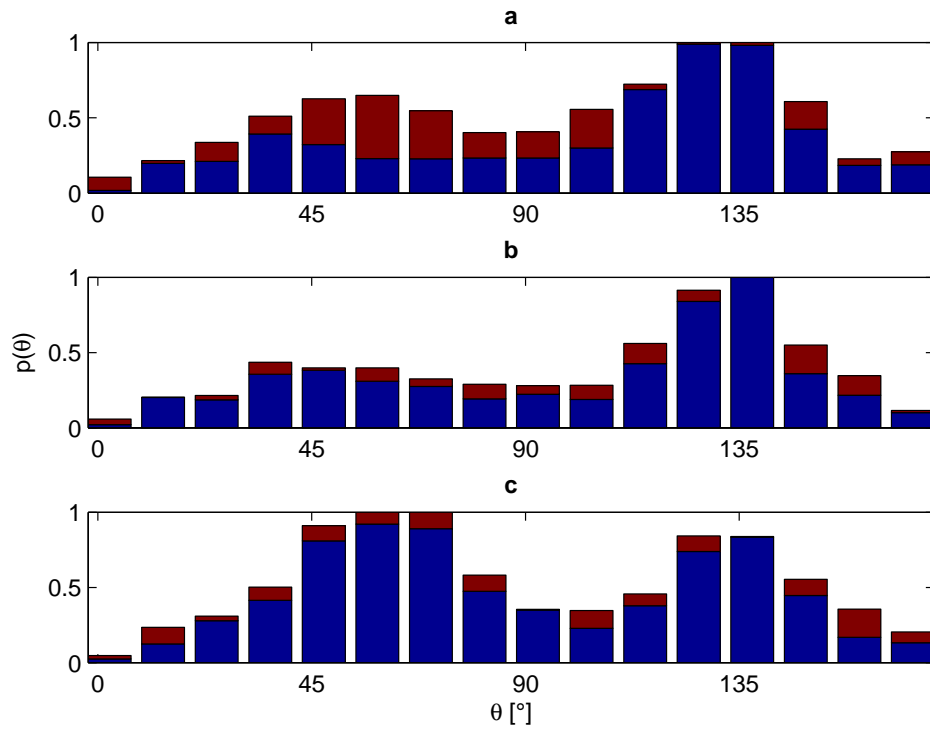


Figure 2.2: Normalized angular power density  $p(\theta)/\max(p)$  for wires **a** to **c** (top to bottom). The red bars indicate the error range based on the maximum deviations between the results obtained for periodically continued and zero padded samples.

gains (grain size 120 nm) shows the smallest directional variations of  $\beta^{\text{rms}} = 58\mu\text{rad}$ , much too small to be explained by a simple corrugation of the top surface that has a measured roughness of  $\delta z^{\text{rms}}/H = 2 \cdot 10^{-3}$ . This observation is an indication that the top surface roughness is not the dominant mechanism causing the irregular current flow.

In order to understand the underlying mechanism for the current direction variations, a simple example of a small local perturbation in the conductivity is considered first. Imagine a cylindrical volume of radius  $R$  extending from the top to the bottom surface of the wire, in which the conductivity is reduced from its bulk value  $\sigma_0$  to  $\sigma_0 + \Delta\sigma$ . The continuity equation for the current density  $\nabla \cdot \mathbf{j} = 0$  together with Ohm's law  $\mathbf{j} = \sigma \mathbf{E}$  gives rise to the following equation for the electric field

$$\nabla \cdot \mathbf{E} = -\frac{\nabla\sigma}{\sigma} \cdot \mathbf{E} \quad (2.1)$$

This equation is equivalent to the Maxwell equation  $\nabla \cdot \mathbf{E} = \frac{\rho}{\epsilon_0}$ , where  $\rho$  is the charge density. It follows that the gradient in the conductivity causes a charge density that is formed on the interface separating the regions of homogenous conductivity. This mechanism builds up a charge dipole around the defect, where the dipole moment  $\mathbf{d}$  is aligned with the incident current. If the conductivity change  $\Delta\sigma$  is small compared to the average conductivity  $\sigma_0$  the total field is made up of the main field  $E^{(0)}\mathbf{e}_x$  and a small perturbation. The dipole moment per unit length

$$d = -\frac{\epsilon_0}{\sigma_0} E^{(0)} \Delta\sigma R^2 \pi \quad (2.2)$$

generates an electric field  $\mathbf{E}^{(1)}$  around the defect. By Ohm's law, this field causes in turn an additional current component  $\mathbf{j}^{(1)}$  which is, to the first order in  $\frac{\Delta\sigma}{\sigma_0}$  given by

$$\mathbf{j}^{(1)} \approx \frac{1}{2} \frac{j_0}{\sigma_0} \frac{\Delta\sigma R^2}{r^2} (\cos 2\theta \mathbf{e}_x + \sin 2\theta \mathbf{e}_y) \quad (2.3)$$

The effect of the defect on the current density is depicted in figure 2.3. The maximal transverse current component appears at an angle of  $\theta = \pm 45^\circ$  measured towards the axis of main current flow.

This simple example is in fact a paradigmatic case that can be generalized easily to an arbitrary perturbation of the conductivity. If the limit of vanishing radius  $R \rightarrow 0$  is taken while keeping the product  $s = \Delta\sigma R^2$  constant, the above formulas can be used for a point defect. As any random distribution of scatterers, which may be interpreted as conductivity noise, can be viewed as a superposition of point like defects the effect of a general conductivity variation may be regarded as an interference of many dipole fields. Whether the effect of this interference can be directly observed in the real space distribution of the current density, mainly depends on the correlation length of the conductivity noise. Figure 2.4 shows simulated noise patterns

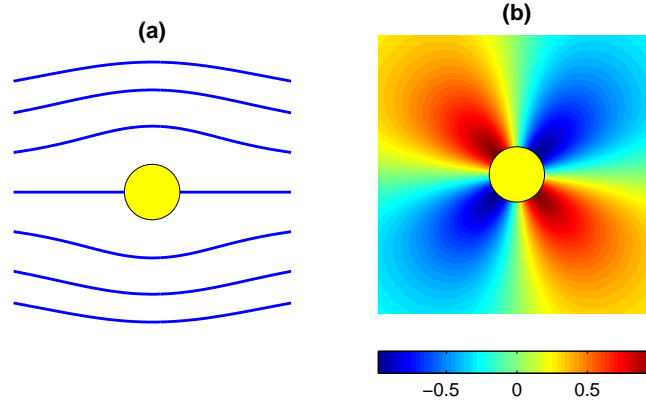


Figure 2.3: *Current flow around a small defect.* (a) Streamlines of the currentflow around the defect. The current flows from left to right. When impinging on the defect in the center a charge dipole builds up that causes a small deviation in the current density. (b) The current component perpendicular to the incident current flow has the typical behaviour of an electric dipole field. This component vanishes in the absence of a defect.

of the transverse current component  $j_y$  for Gaussian conductivity noise of different correlation lengths. A necessary condition for the observation of a  $45^\circ$  preference in real space is, that the correlation length  $l$  of the conductivity noise is large compared to the resolution limit of the detection method. The length  $l$  gives the typical size of fluctuations so that one may say alternatively, that individual fluctuations in the conductivity noise need to be resolved.

Within a small area that has a diameter smaller than the correlation length, conductivity fluctuations can be assumed in a first approximation to have the same sign and amplitude i.e. they are perfectly correlated. A simple model case for this regime is an array of equally spaced defects that can have different orientations relative to the incident current flow. This model case is pictured in figure 2.5. The large difference in amplitude of the resulting transverse current amplitude is a result of the interference between the single defects. For the orientation of  $\theta = \pm 45^\circ$  the currents interfere constructively. For  $\theta = 0^\circ/90^\circ$  the interference is destructive. This interference effect is the mechanism, that causes a high transverse current density to occur at random conductivity fluctuations that have a  $45^\circ$  orientation.

The collective effects that occur for a random conductivity distribution may be analyzed more clearly when the variations are viewed as an independent superposition

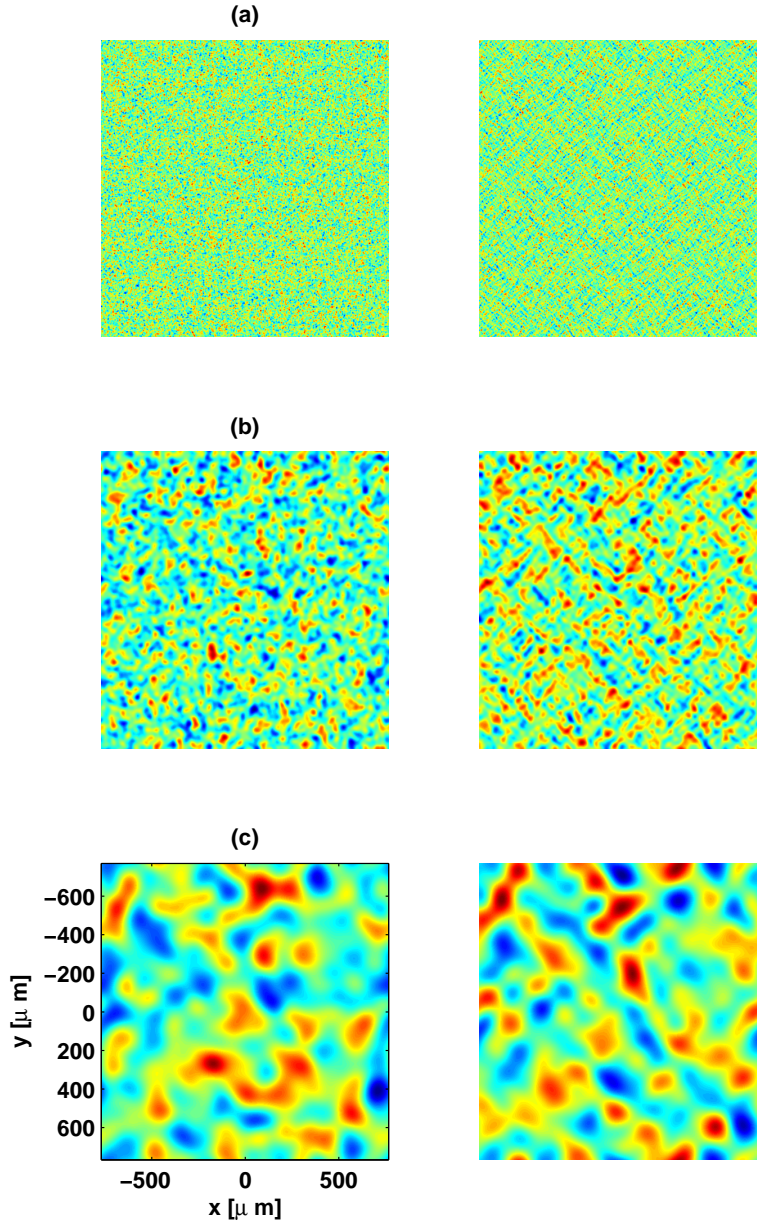


Figure 2.4: *Effect of directional filtering on noise with different correlation lengths.* The pictures show the normalized conductivity noise (left column) and the y-component of the current density  $j_y$  (right column) for conductivity noise that follows a Gaussian distribution  $\frac{\sigma_{\mathbf{k}}}{\sigma_0} = \exp(-k^2 l^2 / (2\sqrt{2})^2)$  (see section 2.6.3). The rms width of the correlation function  $g(r) = \exp(-r^2/l^2)$  is given by  $l$ . This parameter adjusts the typical spatial size of fluctuations. The values are **(a)**  $l = 10\mu m$ , **(b)**  $l = 50\mu m$  and **(c)**  $l = 200\mu m$ . The 45° preference of the current noise is clearly visible to the eye in the regime where the size of the observation region is large compared to  $l$  but small enough that individual fluctuations can be resolved.

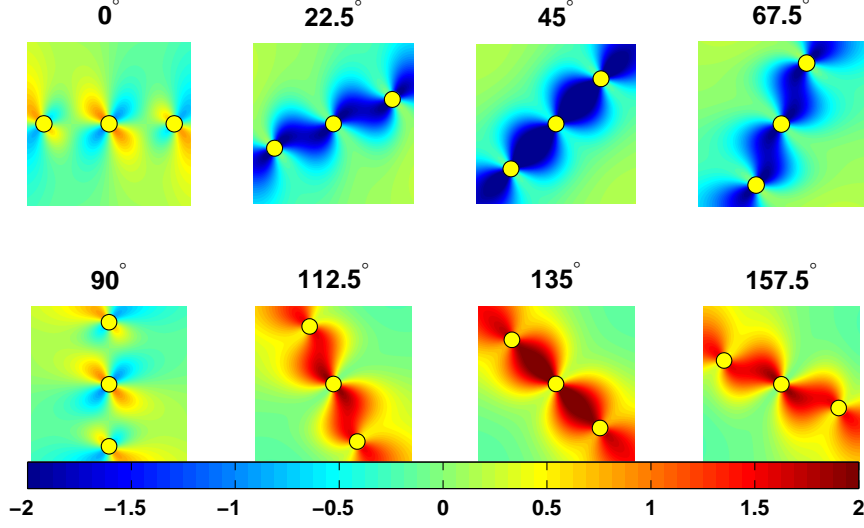


Figure 2.5: *Array of coherent defects.* The pictures show the transverse current density  $j_y$  (relative units) in the central region of an array of 65 equally spaced defects having all the same amplitude. The mean current density  $j_0 \mathbf{e}_x$  enters from the left.

of plain Fourier modes

$$\Delta\sigma = \sum_{\mathbf{k}} \Delta\sigma(\mathbf{k}) e^{i\mathbf{k}\cdot\mathbf{x}} \quad (2.4)$$

. Each harmonic term  $\Delta\sigma(\mathbf{k}) e^{i\mathbf{k}\cdot\mathbf{x}}$  produces a response in the transverse current density that has a similar orientational behavior as for the case of an array of defects. The current direction fluctuations  $\alpha(\mathbf{x}) = j_y(\mathbf{x})/j_0$  may be written in a similar way as

$$\alpha(\mathbf{x}) = \sum_{\mathbf{k}} \alpha(\mathbf{k}) e^{i\mathbf{k}\cdot\mathbf{x}} \quad (2.5)$$

where the substitution of this ansatz into equation 2.1 determines the Fourier coefficients

$$\alpha(\mathbf{k}) = -\frac{1}{2} \frac{\Delta\sigma(\mathbf{k})}{\sigma_0} \sin 2\theta \quad (2.6)$$

A major advantage of this Fourier approach is, that the computation of the magnetic field above the wire assumes a particular simple form. The angle variations of the magnetic field direction at a height  $z$  above the wire surface are, in the limit of a thin film, directly related to the directional fluctuations of the current density  $\alpha(\mathbf{k})$  by

$$\beta(\mathbf{k}, z) = e^{-kz} \alpha(\mathbf{k}) = -e^{-kz} \frac{1}{2} \frac{\Delta\sigma(\mathbf{k})}{\sigma_0} \sin 2\theta \quad (2.7)$$

which follows the angular dependence  $\beta(\mathbf{k}) \propto \sin 2\theta$ . The exponential term  $e^{-kz}$  is reminiscent of the fact that the imaging of static electromagnetic fields is inherently a near field technique. Wavelengths that are shorter than typical scale of  $2\pi z$  are significantly suppressed by the exponential and limit the resolution that is obtainable with magnetic field imaging.

In order to quantify the angular preference of the measured magnetic field maps, the normalized angular power spectrum

$$p(\theta) = \int dk k |\beta(k, \theta)|^2 / \max p(\theta) \quad (2.8)$$

is presented in figure 2.2. Using equation 2.7, this quantity is expected to behave as

$$p(\theta) = \sin^2 2\theta \quad (2.9)$$

for an isotropic noise distribution where  $\Delta\sigma(\mathbf{k}) = \Delta\sigma(k)$ . The deviations from the ideal  $\sin^2 2\theta$  behavior in the measured data can be attributed to two sources.

The first is the limited statistics that is caused by the finite sample area. This effect is most prominent for the wire (**a**) as the the spatial extent of the fluctuations is largest there. For wavelengths that are comparable to the sampling window the spectrum estimation is complicated by edge effects. An estimate of their importance has been derived by computing the Fourier spectrum once for periodic and once for zero padded boundary conditions. The resulting error is indicated by the red bars. Another statistical effect is due to the distribution itself. Even if  $\sigma(\mathbf{k})$  is isotropic in the limit of a large sample size, fluctuating anisotropies necessarily occur if the sampled area is comparable to the correlation length. This effect has been tested numerically for the already mentioned Gaussian distribution. The result is shown in figure 2.6. Besides these statistical error sources, additional anisotropic noise is introduced by the scanning technique itself. As each column in the pictures of figure 2.1 represents a separate measurement, slight variations in temperature and the total number of the atoms in the cloud lead to a statistical potential offset between the columns. This contribution is visible in the pictures as a stripe impression. The corresponding noise spectrum makes an exclusive contribution to Fourier modes that have a wave vector along the  $90^\circ$  direction. This shot to shot noise explains the finite value of  $p(\theta)$  at  $\theta = 90^\circ$ .

In order to exclude the possibility that the observed directional preference is caused by an anisotropy in the wire structure, the topography of the top surface has been measured with a Zygo interferometer (see figure 2.12). The same analysis as for the magnetic field maps showed no preferred orientation on the surface.

The interpretation and the model that has been introduced up to this point, focused exclusively on the case where changes in the current flow are caused by changes in the bulk conductivity of the film. The presented symmetry is however not specifically linked to this perturbation. For example, a variation of the wire thickness by  $\delta H/H$

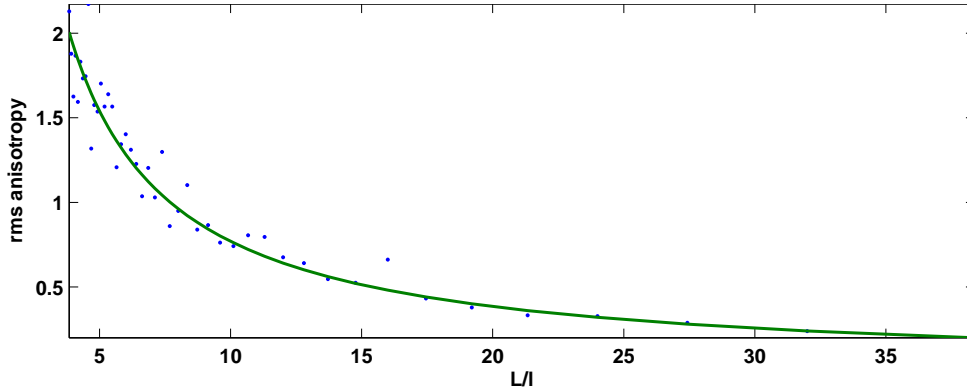


Figure 2.6: *Isotropy fluctuations.* An isotropic Gaussian distribution of variable correlation length  $l$  has been sampled on a finite window of size  $L \times L$ . The rms anisotropy  $\langle (p(\theta) - \langle p(\theta) \rangle)^2 \rangle^{1/2} / \langle p(\theta) \rangle$  is found to scale inversely proportional to the sample size  $L/l$  which is indicated by the green line.

has the same effect as a relative change in the conductivity by  $\delta\sigma/\sigma$ . In order to find the specific origin of fluctuations the magnitude and finally the spectral composition of the measured  $\beta$  spectrum has to be compared to some model, based on independently measured material properties. The details of the defect models can be found in section 3.3.

## 2.3 The Origin of Fluctuations

There are two immediate observations that are apparent without any further analysis. First, the spatial size of fluctuations above wire **(a)** is significantly larger compared to wires **(b)** and **(c)** and second, the rms amplitude of fluctuations above wire **(a)** is significantly larger than above wire **(b)** and **(c)** (see table 2.1). In order to emphasize that these observations are not artefacts, introduced by some experimental inaccuracy either in the height positioning above the wire surface or errors in the temperature calibration for the thermal clouds, two microscopy measurements using Bose-Einstein Condensates will be presented now.

### 2.3.1 Exact Statements from Qualitative Scans

According to equation 2.7 the spatial resolution that is obtained in magnetometry depends on the distance of the measurement plane to the current carrying layer. A series of microscopy scans using condensates at different height levels above wire **a** have been conducted to exclude a low pass filtering of the image by this effect. Figure 2.7 shows for comparison the  $\beta$  map and the condensate density at the same height of  $z = 4\mu\text{m}$  above the wire. The condensate fills up the minima of the potential i.e. the regions of negative  $\beta$  (see section 4.3). This density does not easily

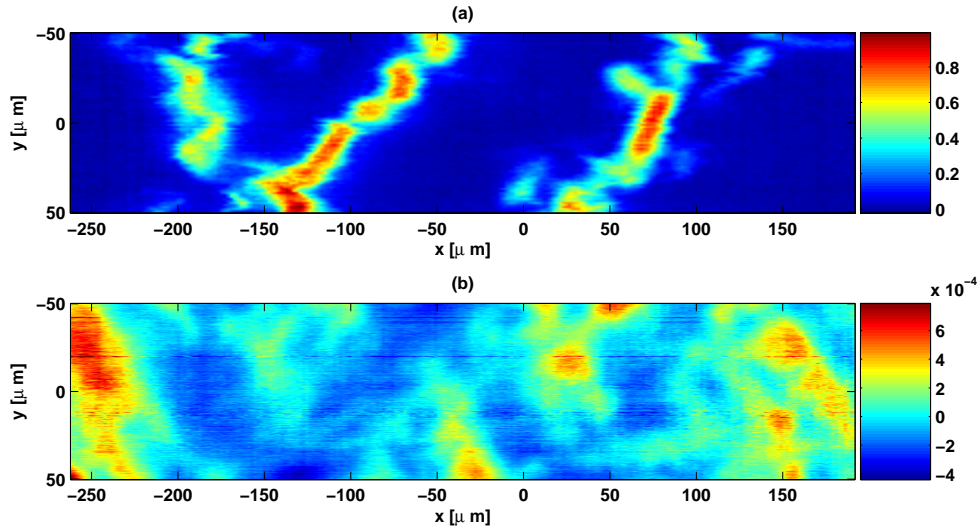


Figure 2.7: *Condensate Density.* (a) Condensate density in arbitrary units (b) Corresponding map of  $\beta$  in units of rad. The condensate fills up the regions of low potential i.e. small  $\beta$ .

allow to reconstruct a full potential, because there are large regions, where the density vanishes and no information on the potential is gathered. It allows however a better resolution of small local features. Approximately, the response of the density  $n$  to the potential is given by  $V - \mu \propto \sqrt{n}$ , where the chemical potential  $\mu$  can be different for each separated condensate.

Using a series of condensate scans, the effect of different measurement height levels on the observed patterns above wire **a** is shown in figure 2.8. As the inaccuracy in the determination of the absolute position above the surface is about  $0.5\mu\text{m} - 1\mu\text{m}$ ,

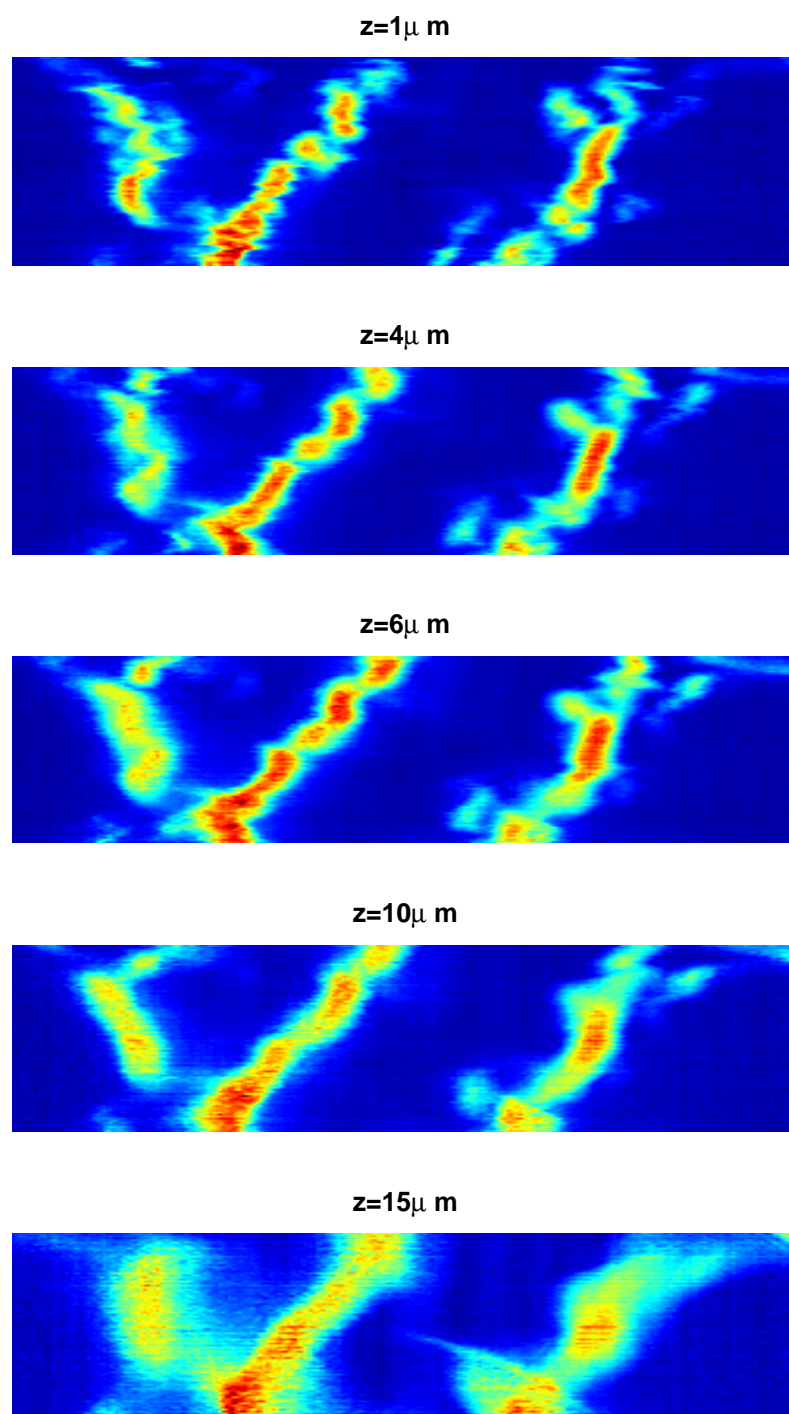


Figure 2.8: *Condensate density at different heights above wire (a).* The colormap and scaling of the axis are the same as in figure 2.7 (a)

the first picture of this series, which has been acquired at a nominal distance of  $z = 1\mu m$  above the surface, is actually to be interpreted as the closest possible measurement distance above the surface, before the atomic cloud is attracted by the van-der-Waals potential. Even at this distance of closest approach, first local losses may be observed that are presumably due to a local protrusion like a grain of dust.

The important qualitative information from this series of pictures is that even at the closest accessible height level, the potential is dominated by the same large scale perturbations that are already visible at a distance of around  $h = 10\mu m$ . The large scale structures are therefore inherent to the specific current distribution of wire **a** and can not be caused by low pass filtering due to a positioning error of the cloud.

A second qualitative test with condensates has been performed to compare the magnitude of fluctuations between the different wires. Figure 2.9 shows the result of condensate scans that have been acquired with the same parameters as the thermal scans of figure 2.1. The total number of atoms is approximately equal for all the scans. For the wires **b** and **c** the condensate covers a much larger area nearly continuously then for wire **a**. At the same total number of atoms, trap frequency and height above the surface, this is a clear qualitative indication that the current fluctuations in wires **b** and **c** are significantly smaller than in wire **a**.

### 2.3.2 Surface Corrugations and Bulk Defects

The sample wires have been carefully implemented to show extremely low surface and edge roughness. The edge roughness as determined from SEM pictures (see figure 2.10 for an example) is on the level of few nanometers. As the magnetic field measurements are conducted only in the central half of the wire, close to its surface, this roughness has negligible influence. Edge effects would be revealed by an increase of the fluctuations towards the wire edge. Such a behavior is not visible in the scans of figure 2.1.

However, the surface roughness of the wires, together with bulk defects, is expected to make a major contribution in the observed current density (see section 3.3). The bulk structure of a typical wire can be seen in figure 2.11. The picture shows the local crystal orientation for a cross section of a  $2\mu m$  thick wire. The orientational sensitivity makes it possible to obtain high contrast differences between single crystalline grains. The transition between two different growth regimes is visible in this picture. Up to a thickness of approximately  $1\mu m$  the grains grow up as columns.

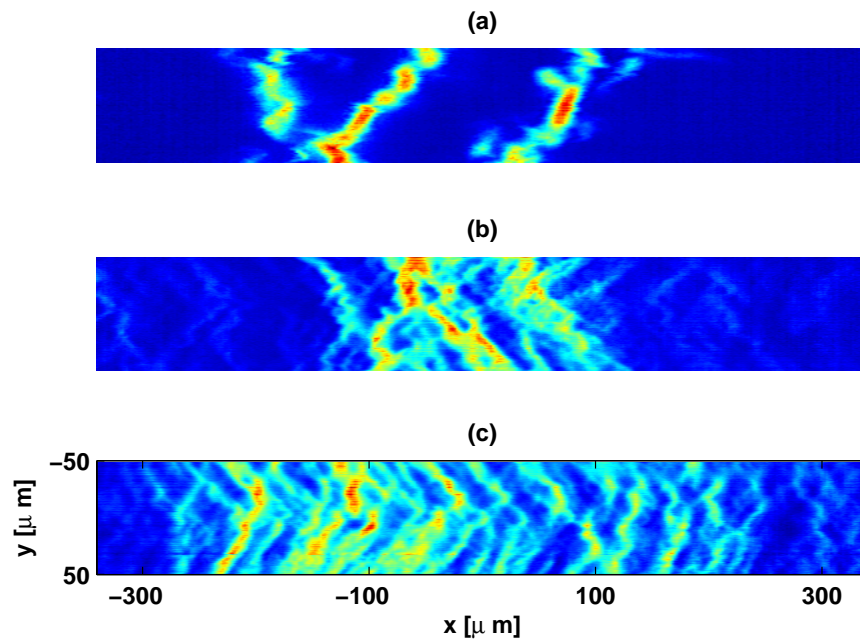


Figure 2.9: *Condensate density above the test wires.* The scan conditions are the same as for the thermal scans. The colormap encodes the atomic density in relative units. The total number of atoms is approximately equal for all the scans.

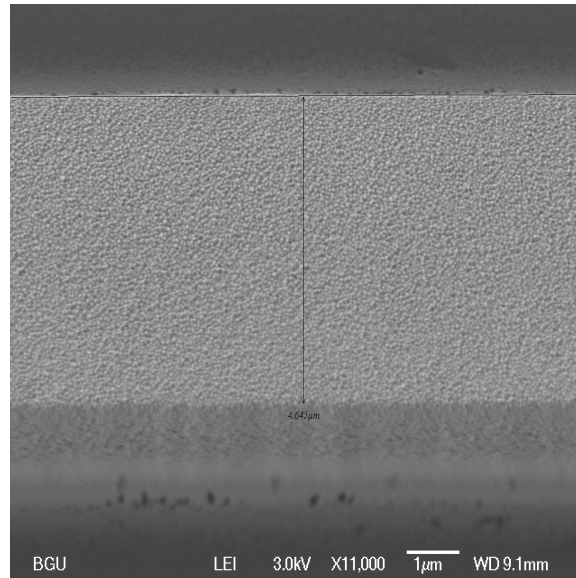


Figure 2.10: *Polycrystalline test wire*: SEM picture of a test wire under a tilt angle of  $\theta = 24^\circ$ . The picture has been acquired at Ben-Gurion-University for a test wire fabricated by a similar process as wire **a**.

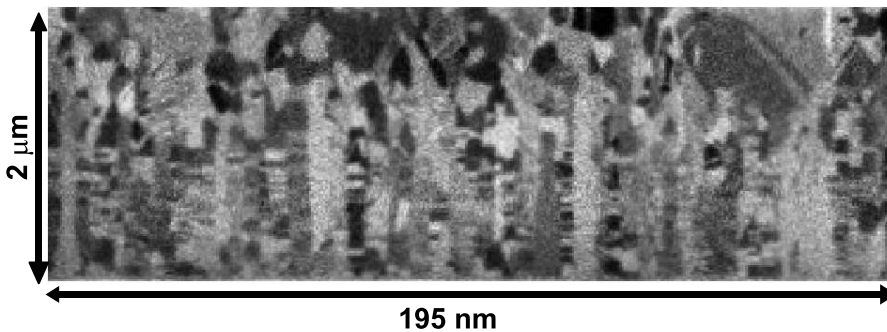


Figure 2.11: *Typical grain structure of the polycrystalline test wires*. Secondary electron Image from Focused Ion Beam etching. The image shows the grain structure of a wire as seen from the side. The contrast is proportional to the local ion etching rate which depends on the angle between grain surface and incident ion beam. The grains grow up in columns up to a maximum height of approximately  $2\mu m$ . Beyond this height bulk effects set in and tend to break the two dimensional symmetry. The picture shows a test wire on a different atom chip that has been produced by a process similar to wire **a**. It has been acquired at the ISIS, Universite Louis Pasteur, Strasbourg.

Above this thickness the two dimensional symmetry starts to break and the grains grow in all spatial directions.

Transferring this picture to the test wires used for the magnetometry scans, wire **a** with a thickness of  $2\mu m$  already has a large contribution of bulk grains. The thin wires **b** and **c**, with a thickness of 250 nm are on the other hand in the thin film regime of columnar grain growth.

A different type of defect is presented by surface roughness. It influences the current flow mainly by variations in the wire thickness that are induced by the corrugations (see section 3.3). In order to allow a direct comparison of the surface roughness with the measured field maps, it is necessary to know the surface topography not on the level of single grains, as can be easily obtained by AFM, but over the same length scales that are sampled by the atoms.

The most suitable method for this purpose is optical interferometry. A Zygo white light interferometer with a transverse resolution of approximately  $0.5\mu m$  and a field of view of about  $50\mu m$  has been used for this task. The sample chip hosting the test wires has been analyzed after the atom magnetometry measurements at Ben Gurion University. Each wire has been scanned in 15 overlapping frames. The resulting pictures, stitched together into a single view for each wire are shown in figure 2.12. From the difference of two pictures in the overlapping regions the noise level of the method has been estimated to an rms height resolution of  $h^{\text{rms}} = 3.5A$ . The height histogram above all three wires follows a Gaussian distribution (figure 2.13). From these, the rms height variations of wires **b** and **c** are seen to be approximately  $6A$  and  $16A$  for the thick wire **a**. After correcting for the noise contribution by the Zygo, the net rms height variations of the thin wires are approximately  $5A$ . The relative rms thickness variations for the thin wires **b** and **c** are therefore by a factor of approximately 2.5 larger than for the thick wire **a**. This tendency clearly contradicts the behavior of the rms  $\beta$  variations. These are largest for the thick wire (see table 2.1 for the comparison). This discrepancy can be resolved, if a variation of the wires' bottom surface is taken into account. If the top surface follows exactly the movement of the bottom surface, there is no net thickness variation of the wire and the influence of the corrugations on the current flow becomes negligible (see section 3.3). Such a mechanism is likely to be the more efficient the thinner the wires are. In the beginning of the wire growth, the gold film follows the large scale fluctuations of the substrate. With growing thickness, the top surface loses correlation with the substrate. This loss of coherence can be expected to be even stronger when the film enters the bulk growth regime above the  $1\mu m$  thickness. In order to give further support to this idea, the topography data has been analyzed quantitatively in two different ways as will be explained now.

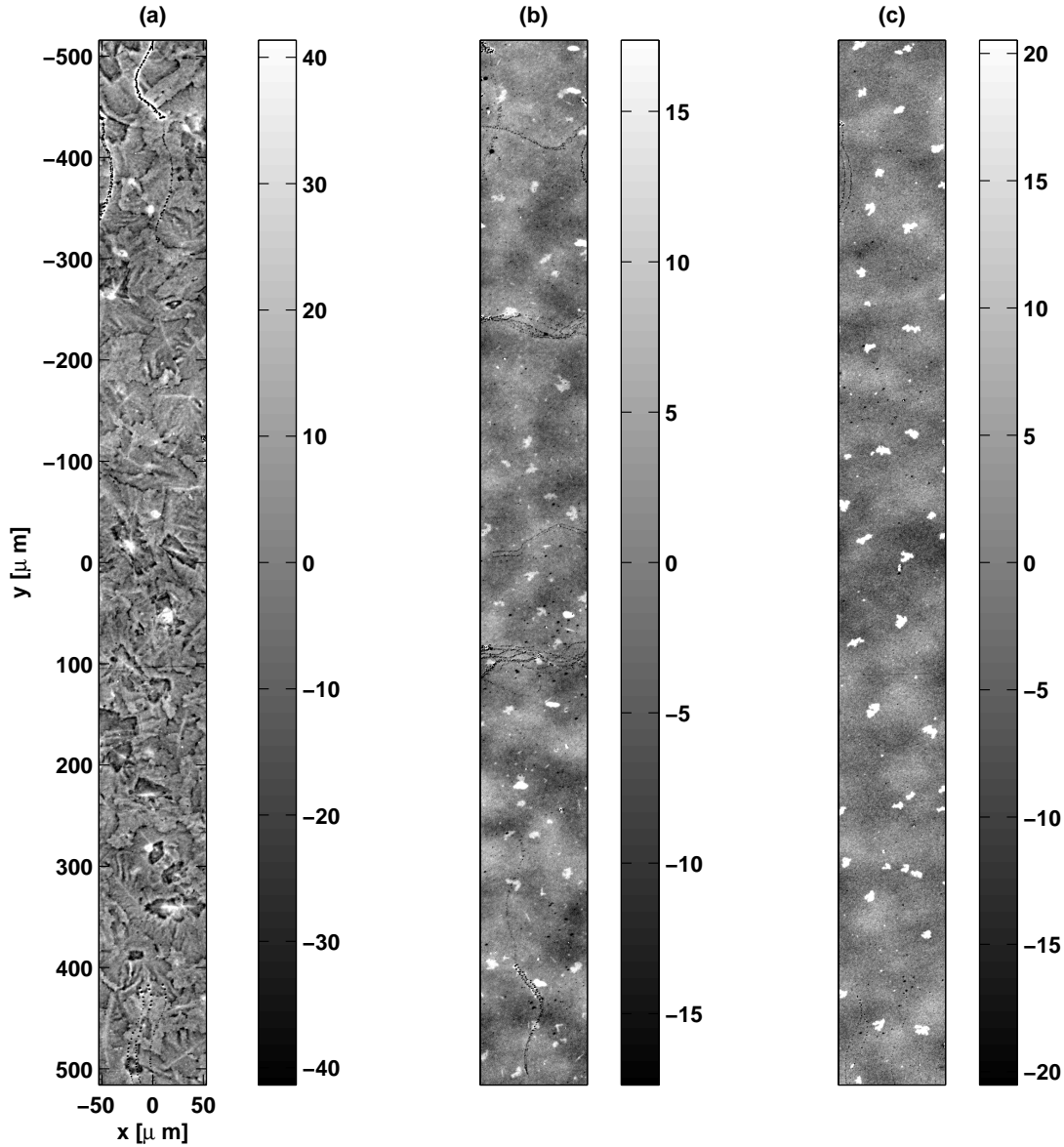


Figure 2.12: *Interferometric height profiles.* The pictures show the surface profile of the three wires (a to c from left to right) that have been examined before by atomic magnetometry. Each picture is stitched together from 15 separate acquisitions. The color scale is labeled in units of  $A$ . The data have been acquired at Ben-Gurion-University by a Zygo interferometer after the magnetometry scans.

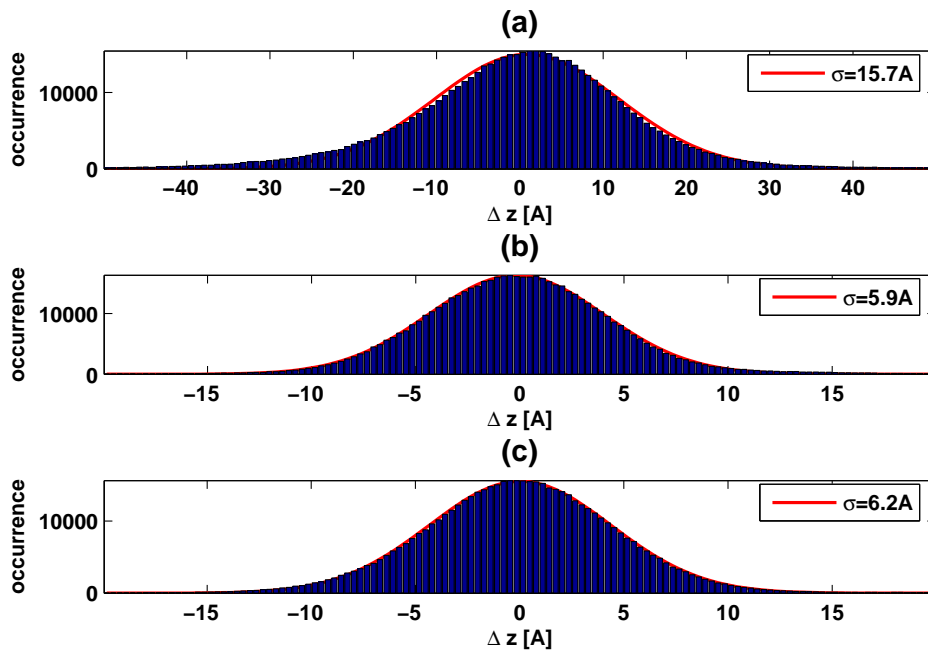


Figure 2.13: *Height variations on wires (a) to (c) as measured by interferometry.* For wires (b) and (c) the gaussian part of the histogram covers over 95% of the data points. The small islands that are visible in the real space pictures of figure 2.12 are not included into the standard deviation. The noise level of the measurements has been estimated from two successive images with an overlapping region. The difference of the two images gives a gaussian distribution which corresponds to a height error of  $\sigma = 3.5 \text{ \AA}$

### 2.3.3 Real Space Correlation Based on Surface Roughness

Assuming, that the top surface roughness makes some finite contribution to the current fluctuations by inducing thickness variations on the wires, a certain correlation between the surface topography and the magnetometry data has to exist. If only the surface roughness would exist, the magnetic field angle variations induced by these corrugations are described analogously to equation 2.7 by

$$\beta(\mathbf{k}) = f(k) \sin 2\theta \delta z(\mathbf{k}). \quad (2.10)$$

(See also equation 3.53 for the exact result.) Here,  $f(k)$  denotes some filter function that depends on the measurement height above the surface and the thickness of the wire.  $\delta z(\mathbf{k})$  is the spectrum of the surface corrugations. This equation is in fact much more general than required by a simple thickness modulation model. As can be induced from figure 1.1, the top surface corrugations may also be linked to the internal growth structure of the wire. If this is the case, there will still be a linear dependence between the surface corrugations and the current fluctuations. The filter function  $f(k)$  will however depend on the range over which the defects extend into the wire and on the exact details of the scattering mechanism.

In order to allow for the most general linear model, where the structure on the top surface is still linked to the current fluctuations, the amplitude of the Fourier coefficients  $\beta(\mathbf{k})$ , calculated on the basis of the surface structure, has been replaced by the amplitude of the measured fluctuation spectrum  $\beta^{\text{meas}}(\mathbf{k})$

$$\beta'(\mathbf{k}) = |\beta^{\text{meas}}(\mathbf{k})| e^{i\phi_z(\mathbf{k})} \quad (2.11)$$

where  $\phi_z(\mathbf{k}) = \arg \delta z(\mathbf{k})$ . After applying an inverse Fourier transform (see 2.6.2), the expected fluctuations  $\beta'(\mathbf{x})$  have been correlated with the measured fluctuations  $\beta(\mathbf{x})$ . As there have been no explicit alignment marks on the wires, the correlation coefficient  $c$  has been calculated for different shifts along the x axis  $\Delta x$  by

$$c(\Delta x) = \frac{\int dx \int dy \beta^{\text{meas}}(x + \Delta x, y) \beta'(x, y)}{\beta_{\text{rms}}^{\text{meas}} \beta'_{\text{rms}}} \quad (2.12)$$

In figure 2.14 the resulting correlation functions are shown for the different wires. The significance of the correlation values has been evaluated by comparison with a phase noise model. The simulated  $\beta'$  spectrum has been generated by adding to the measured phase  $\phi_{\text{meas}}(\mathbf{k})$  a certain relative amount  $r$  of white phase noise  $\phi_{\text{rand}}(\mathbf{k})$

$$\beta'(\mathbf{k}) = |\beta^{\text{meas}}(\mathbf{k})| \exp [i((1 - r)\phi_{\text{meas}}(\mathbf{k}) + r\phi_{\text{rand}}(\mathbf{k}))] \quad (2.13)$$

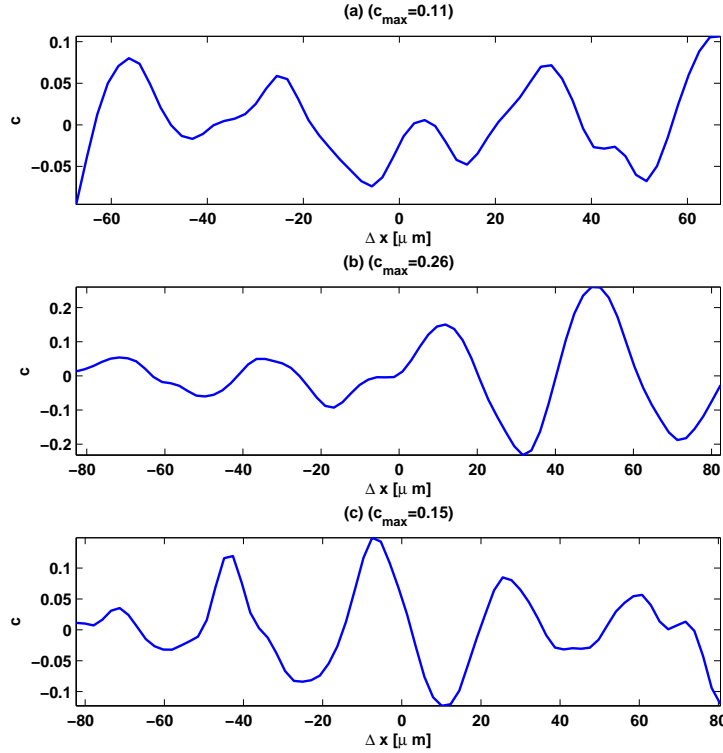


Figure 2.14: *Correlation function between  $\beta^{\text{meas}}$  and  $\beta'$ .* The correlation coefficient  $c$  is computed between  $\beta'$  and a copy of  $\beta^{\text{meas}}$  that has been shifted by  $\Delta x$  along the x-axis. The only correlation value which is significantly larger than 0 (probability 99.5%) occurs for wire **b** where  $c_{\text{max}} = 0.26$

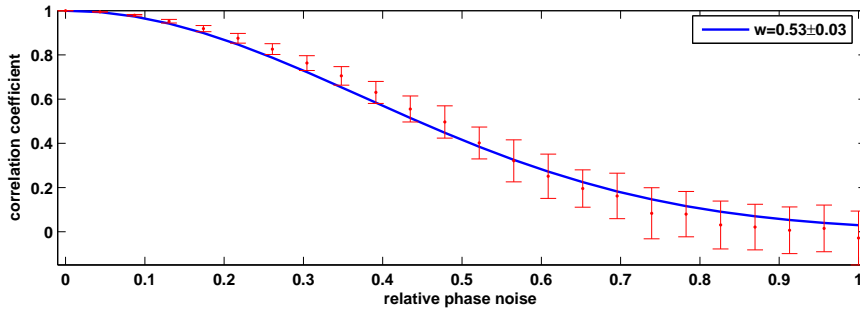


Figure 2.15: *Correlation dependence on phase noise.* The correlation coefficient is calculated between the measured data  $\beta^{\text{meas}}$  and the same data after a phase noise contribution of relative amount  $r$  has been applied. The errorbars indicate the range of  $\pm$  one rms variation between several realizations of the same noise amplitude

For the spectra  $\beta'$  simulated in this way, the correlation coefficient with the measured data  $\beta^{\text{meas}}$  has been calculated. Figure 2.15 shows the result of this simulation for wire **b**. The curves are however similar for all the wires. The errorbars indicate the range of  $\pm$  one rms variation between several realizations of the same noise amplitude. This simulation shows, that a measured correlation value of approximately 0.2 is needed to establish a correlation significantly different from 0 ( the propability for c to be larger then zero is than 99.5%). This criterion can only be met for wire **b**. However, the absence of a correlation for the other two wires does not firmly establish the absence of correlation between the magnetic field fluctuations and the surface structure. As there have been no explicit alignment marks on the wires, the absolute position of the regions scanned by the atoms and by the interferometer is not known exactly.

Figure 2.16 shows the measured fluctuations  $\beta^{\text{meas}}$ , the expected fluctuations based on the Zygo measurements  $\beta'$  and the original wire topography for the region of maximum correlation above wire **b**.

### 2.3.4 Power Spectrum

In a different approach, that does not rely on the exact positioning of the topography data relative to the magnetic field maps, the surface measurements are used to extract not the phase information but the power spectrum. Detailed calculations of the spectra, assuming a combination of top/bottom surface corrugations and bulk fluctuations have been carried out by Y.Jaffa at Ben Gurion University [12]. The results are summarized in figure 2.17 which shows a comparison of measured and calculated Fourier spectra. In contrast to the two dimensional approach presented above, the longitudinal power spectrum  $P_1(k_x) = \sum_{k_y} |\beta(k_x, k_y)|^2$  is used here.

Two main results can be deduced from these calculations. For the thick wire **a** pure surface corrugations alone can not explain the observed magnitude of field fluctuations. Some bulk contribution has to be assumed to explain the spectra measured by the atoms. For wires **b** and **c** on the other hand, the observed fluctuations are significantly smaller then what would be expected from pure top surface corrugations and significantly larger then expected for a model where the top surface follows the bottom surface without thickness modulations of the wire.

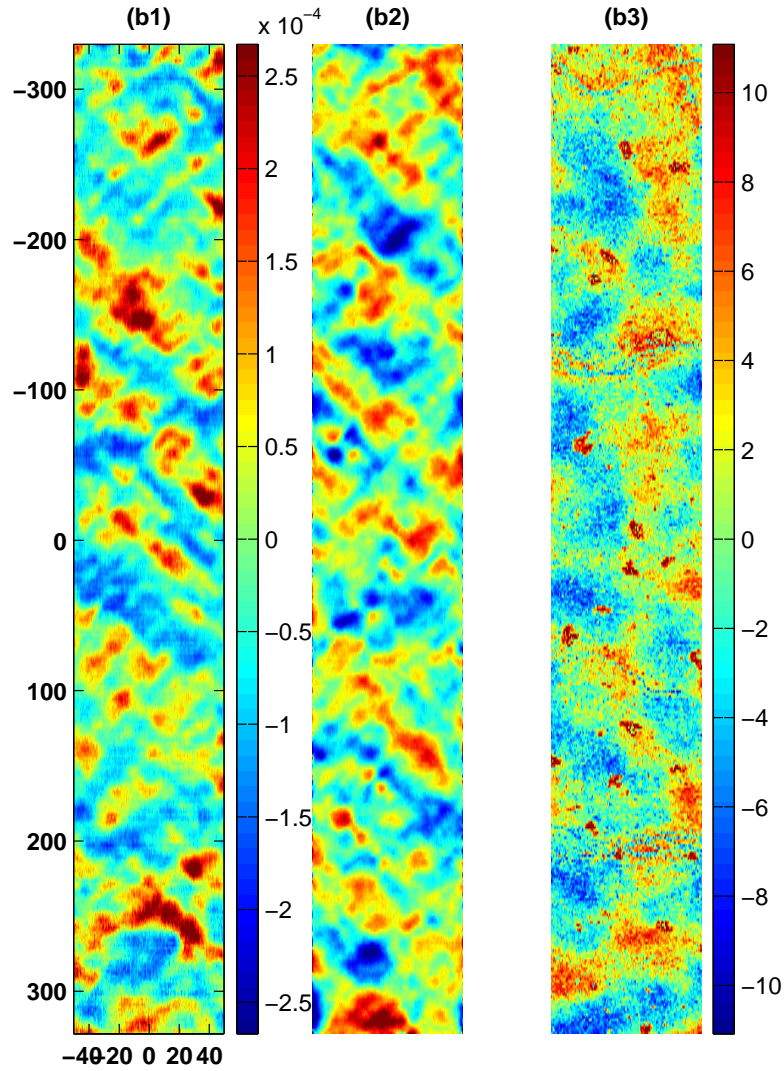


Figure 2.16: *Correlated regions of field fluctuations and surface topography.* The pictures show the region of maximum correlation coefficient  $c_{\max} = 0.26$  between measured and expected angle variations for wire **b**. **b1**: measured angle variations  $\beta^{\text{meas}}$  in units of rad. **b2**: expected angle variations  $\beta'$  based on the surface topography. **b3**: measured surface topography in units of  $A$ .

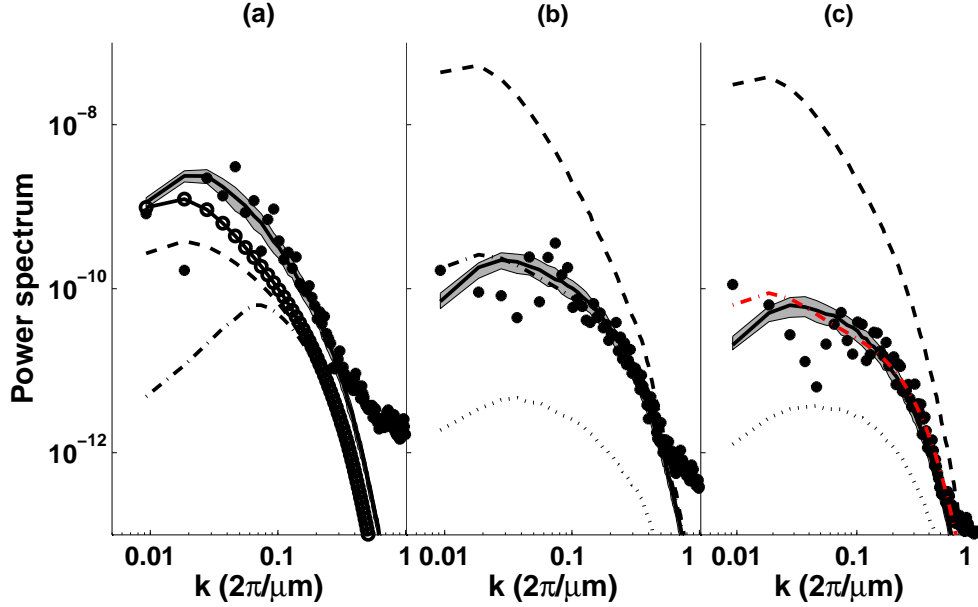


Figure 2.17: Longitudinal power spectrum  $P_1(k_x)$ . (Summary of the calculations by Y.Jaffa at Ben-Gurion -University [12]) Solid line: a fit to a model assuming bulk conductivity fluctuations  $\delta\sigma(k)/\sigma_0 = (\delta\sigma(k_0)/\sigma_0)(k_0/k)^\nu$ , with  $\nu = 1$  for wire **a** and  $\nu = 1/2$  for wires **b** and **c**,  $\delta\sigma(k_0)/\sigma_0$  for  $k_0 = 2\pi/680\mu m$  is  $3.33 \cdot 10^{-4}$ ,  $4.32 \cdot 10^{-5}$  and  $2.32 \cdot 10^{-5}$ , for wires **a**, **b** and **c** respectively. The shaded area represents a one standard deviation range obtained by varying the relative phases of different spectral components  $\delta\sigma(k_x, k_y)$ . Dashed line: expected power spectrum from the measured top surface  $\delta z_+ = \delta z$  and flat bottom surface  $\delta z_- = 0$ . Dotted line: Expected power spectrum for the case where the bottom surface varies exactly in the same way as the top surface  $\delta z_+ = \delta z_-$  (no thickness variations). Dashed-dotted line: a combined model assuming  $\delta z_-(k) = A\delta z_+(k)e^{-(k/k_c)^2}$ , where  $A = 0.998$  and  $k_c = 0.764\mu m^{-1}$  for wire **b** and  $A = 0.999$  and  $k_0 = 1.548\mu m^{-1}$  for wire **c**. For the thick wire **a** it is assumed that the spectrum of the bottom surface (substrate)  $\delta z_-(k)$  is similar to that of wire **b**. The line with circles in figure (a) represents a model assuming uncorrelated top and bottom surfaces  $\delta z_+$  and  $\delta z_-$ . All the surface models underestimate the measured magnetic field fluctuations for the thick wire **a**.

## 2.4 Conclusion

In conclusion it has been shown in this study that cold atom magnetometry is a sensitive tool that is ideally suited to study long range transport phenomena in quasi-two-dimensional solid state systems.

It has been found that angle variations of the current density in thin polycrystalline gold films tend to form correlated patches that are oriented by  $\pm 45^\circ$  towards the axis of main current flow. This phenomenon has been explained in terms of selective scattering at an isotropic defect distribution. The origin of defects has been shown to have at least two different contributions, namely bulk and surface defects. For the case of the 250nm thin wires a quantitative comparison with the measured surface corrugations forces one to assume that the top surface follows the bottom surface of the wire to a significant extent. For the  $2\mu m$  thick wire, all surface effects taken together cannot explain the observed significantly larger fluctuation magnitude. In this case bulk defects have to make a contribution.

Taken together, the results may be interpreted within a picture of thin film growth, where the top surface of the film initially follows the substrate surface, and then slowly loses correlation to the bottom layer. Starting from a thickness of about  $1\mu m$  the wire enters a bulk growth regime where the two dimensional symmetry of columnar grain growth is broken. This effect may be connected to the significant bulk defect contribution in the thick wire.

This study has been the first real space observation of long range current scattering at static defects. It complements the information that can be obtained from low temperature conductance measurements [5] and scanning tunneling potentiometry [6]. It gives direct insight into the collective effect of Landauer's residual resistivity dipoles [4].

## 2.5 Experimental Scan Parameters and error Estimates

The ultra cold atomic samples used to probe the magnetic field landscape above the sample wires are prepared in the setup described in [13].  $^{87}\text{Rb}$  atoms are first laser cooled, then optically pumped into the  $|F = 2, m_F = 2\rangle$  state and in 20s of forced evaporation in a magnetic trap of transverse and longitudinal trapping frequency  $\omega_{\perp} = 2\pi \times 840\text{Hz}$  and  $\omega_x = 2\pi \times 21\text{Hz}$  (see section 4.5 for measurements) cooled to a temperature  $\sim 1\mu\text{K}$ . From this trap which is situated at  $100\mu\text{m}$  above the chip surface, the atoms are transferred within a typical time of 800ms to the measurement location and further cooled to the final temperature selected to optimally measure the magnetic field variations. The resulting atom cloud is then typically  $600\mu\text{m}$  long trapped in a quasi one dimensional geometry with a transverse trapping frequency of  $\omega_{\perp} = 2\pi \times 500\text{Hz}$  and longitudinal trapping frequencies of  $\omega_x = 2\pi \times 2.5\text{Hz}$  for wire **a** and  $\omega_x = 2\pi \times 0.9\text{Hz}$  for wire **b** and **c**. The current through the sample wires has been adjusted to 180mA in each case. The atomic density has been detected by resonant absorption imaging after  $\approx 1\text{ms}$  time of flight. For imaging (see section 4.2), a  $50\mu\text{s}$  pulse of linear out of plane polarized light at an intensity below 10% of the saturation intensity has been used. Employing diffraction limited optics, an optical resolution of  $\sim 3\mu\text{m}$  is achieved. The magnetic field angle variations have been extracted from a measurement of potential variations, through changes in the density of a Boltzmann distributed thermal cloud (see section 1.2). Expressed by the experimentally accessed parameters, the field angle fluctuations of a single scan line are determined by

$$\beta(x) = - (k_B T / \mu_B B_y) \log n_1(x) \quad (2.14)$$

where  $n_1$  is the line density (atoms/m) of the atomic cloud,  $B_y$  the transverse magnetic field produced by the homogenous part of the current density in the wire and  $T$  the temperature of the cloud. Small fluctuations in the total number of atoms between single scan lines result to first order only in a constant offset of the whole line. If the density is normalized separately for each line this effect can be largely suppressed. The most critical parameter that contributes to the noise and systematic uncertainty in this expression is the temperature. The homogenous magnetic field on the other hand is not particularly sensitive and presents no further difficulties.

A second quantity that is crucial in magnetic field microscopy is the exact height level above the chip surface. As the Fourier components of  $\beta$  drops off exponentially with  $e^{-kz}$  the exact positioning is very important for the exact quantification of high

spatial frequencies.

The calibration measurements for the temperature and the height level above the chip surface will now be presented. The estimated errors are summarized in table 2.2.

wire	<b>a</b>	<b>b</b>	<b>c</b>
Temperature T [nK]	$286 \pm 15$	$173 \pm 2$	$92 \pm 7$
Scan height [ $\mu m$ ]	$3.5 \pm 0.8$	$3.8 \pm 0.4$	$4.0 \pm 0.6$
y center offset [ $\mu m$ ]	$\pm 2\mu m$	$\pm 2\mu m$	$\pm 2\mu m$
approx. y scaling error	$\pm 10\%$	$\pm 10\%$	$\pm 10\%$

Table 2.2: *Error estimates for the magnetometry scans.*

## 2.5.1 Temperature measurements

The temperature has been determined by a series of time of flight measurements (see section 4.4). Figure 2.18 shows the atomic density distribution at increasing time intervals after turning off the trapping potential. From such a series of measurements two parameters can be extracted. The center of mass motion follows a free fall parabola trajectory. Comparison with the known gravitational acceleration allows the calibration of the length scale independently of any knowledge about the imaging optics. The second parameter is the expansion speed of the cloud i.e. the increase of the cloud's width. The kinetic energy that is contained in this relative motion allows to directly measure the temperature by

$$k_B T = \frac{m}{2} v_{\perp}^2 \quad (2.15)$$

where  $v_{\perp} = \frac{dw_{\perp}}{dt}$  and  $w_{\perp}$  is the Gaussian width of the density distribution  $d(z) = d_0 \exp -\frac{z^2}{w_{\perp}^2}$ . An error estimate on the length scale calibration can be directly obtained from the center of mass motion and is taken into account in all the calibrations. Figure 2.19 shows the estimated parameters from a least square fit to the transverse density profile averaged over a small region of the cloud. In order to estimate the influence of noise and possible density induced interaction effects, the temperature has been extracted from the expansion series in two different ways. As the cloud extends over a larger range in the x-direction, the Gaussian fit can either be applied to the mean profile, averaged over the longitudinal direction, or to each separate section at a fixed  $x$  position. A typical result of these two methods is shown

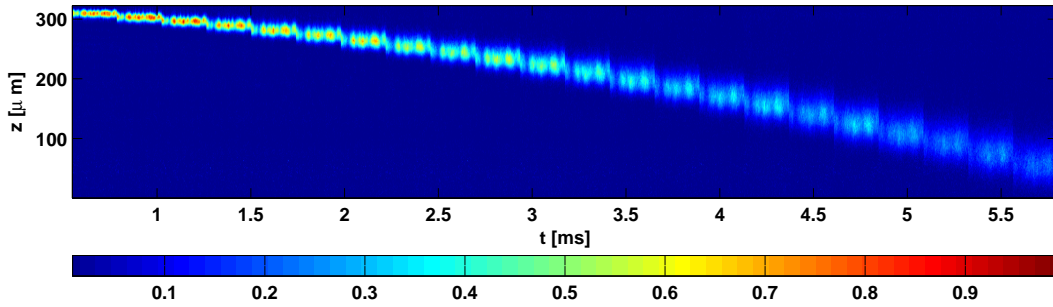


Figure 2.18: *Temperature and length scale from time of flight expansion.* A series of density distributions are acquired for different expansion times (time after switching of the trapping potential). The center of mass motion follows a free fall parabola, while the transverse expansion speed of the cloud is a measure of the temperature.

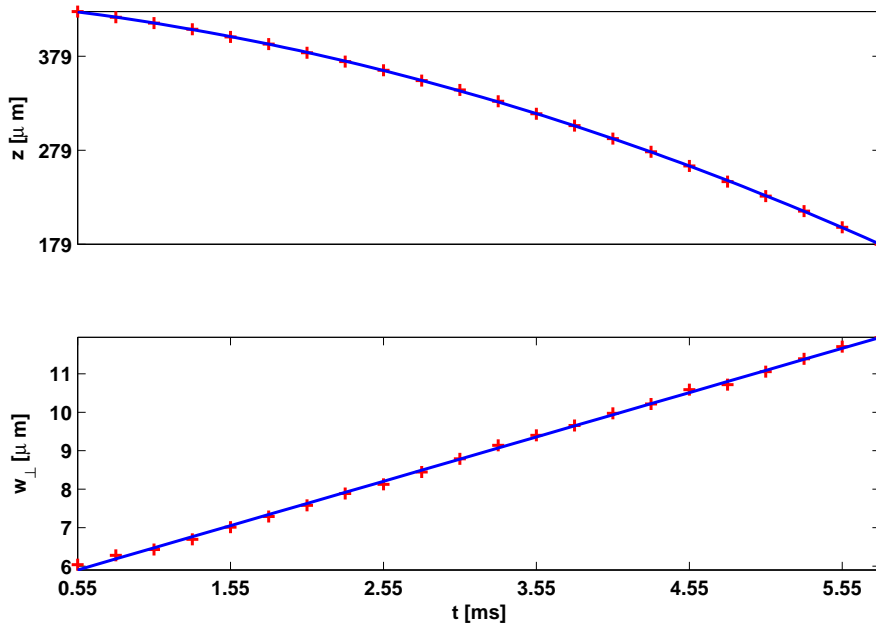


Figure 2.19: . **Upper panel** length scaling  $s = 1 \pm 0.02$  **Lower panel** Velocity from the mean profile  $v_{\perp} = (5.76 \pm 0.09) \frac{\text{mm}}{\text{s}}$

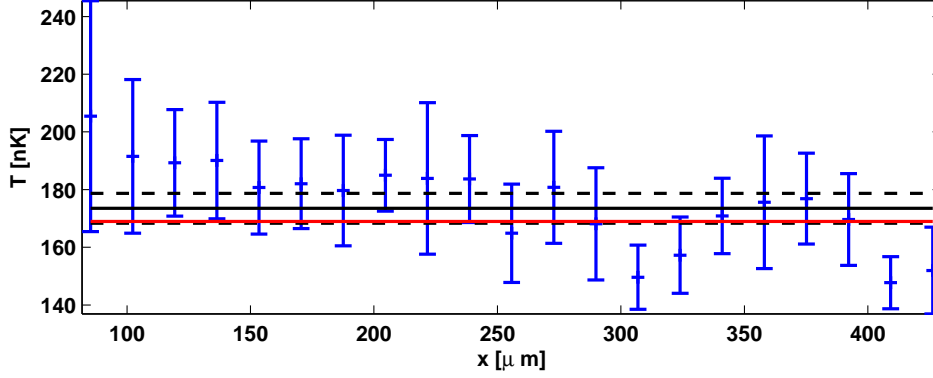


Figure 2.20: *Fit of the mean profile in comparison to fitting separate sections.* Temperature from mean profile  $T_m = (173.5 \pm 5)\text{nK}$ , average temperature for single section fits  $T_s = 169\text{nK}$

in figure 2.20. These two methods agreed within the statistical error range. As no larger deviations in the two methods have been observed, density and noise effects are assumed to have no significant influence on the temperature estimation.

For the energy calibration of the microscopy scans the temperature has been measured at least at five equally space transverse positions within the scanned area to exclude variations of the temperature with the scan position. The resulting values are shown for wire **a** to **c** in figure 2.21 to 2.23. The red lines show the average temperature, based on fits along single sections whereas the blue lines indicate the temperature due to a fit to the average profile. The adopted temperature value is an error weighted average (see section 2.6.4) of these two values. The results for wires **a** to **c** are  $T = 286 \pm 15\text{nK}$ ,  $T = 173 \pm 2\text{nK}$  and  $T = 92 \pm 7\text{nK}$  respectively.

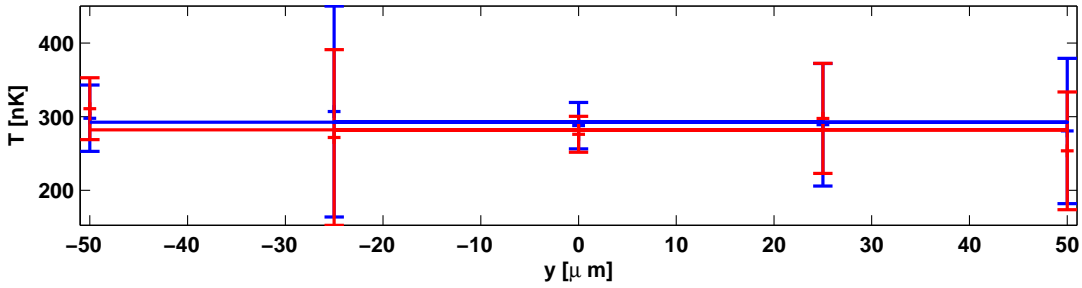


Figure 2.21: Wire **a**. Mean temperature from mean profile  $T_m = (290 \pm 24)$  nK, max/min values 307nK,281nK. Mean temperature from single shots  $T_s = (284 \pm 19)$ , max/min values 311nK, 254nK Adopted Value:  $286 \pm 15$ nK

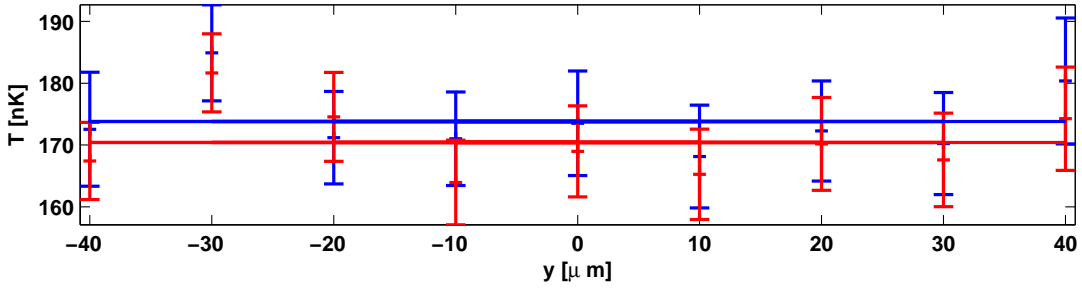


Figure 2.22: Wire **b**. Mean temperature from mean profile  $T_m = (174 \pm 3)$  nK, max/min values 185nK, 168nK. Mean temperature from single shots  $T_s = (171 \pm 3)$ , max/min values 182nK, 164nK Adopted Value:  $173 \pm 2$ nK

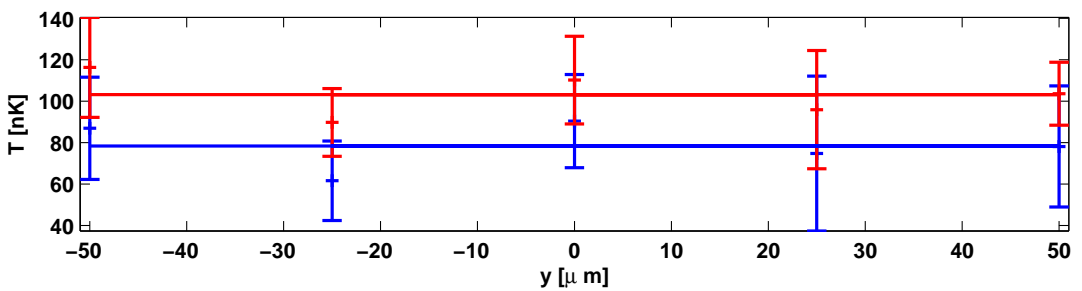


Figure 2.23: Wire **c**. Mean temperature from mean profile  $T_m = (77 \pm 11)$  nK, max/min values 90nK, 62nK. Mean temperature from single shots  $T_s = (102 \pm 9)$ , max/min values 117nK, 90nK Adopted Value:  $92 \pm 7$ nK

## 2.5.2 Positioning and Height calibration

For the scanning microscopy the magnetic gradient field, produced by the homogenous part of the current density has been used to provide the magnetic trapping potential. A minimum in the absolute value of the magnetic field is established by compensating the homogenous part of the wire field by homogenous external bias fields. The spatial position of the minimum in the  $y - z$  plane is adjusted by compensating the wire field at exactly the demanded scan position  $(y_0, z_0)$ . For the gradients used in this work, the additional influence of gravity is negligible. In this way the two orthogonal homogeneous bias fields  $B_y$  and  $B_z$  have been used to position the trap minimum. Initially, the absolute magnitude of these bias fields is not known. They are however proportional to the current  $I_y/I_z$  through the coils so that  $B_{y/z} = B_{y/z}^o + \alpha_{y/z}I_{y/z}$ . The scan position in the  $y - z$  plane is then determined in terms of the experimental parameters by

$$\begin{aligned} B_y^w(y_0, z_0) &= B_y^o + \alpha_y I_y \\ B_z^w(y_0, z_0) &= B_z^o + \alpha_z I_z \end{aligned}$$

. By these equations the position calibration is reduced to the calibration of the bias field parameters. For a scan height  $h$  close to the wire surface  $z = 0$  and a symmetric scan range around the wire center  $y = 0$  the equations can be linearized and the response between the change in the position coordinates and the bias field currents is seen to be diagonal

$$\begin{aligned} gz + B_y(z = 0) &= B_y^o + \alpha_y I_y \\ gy &= B_z^o + \alpha_z I_z \end{aligned}$$

Here,  $g$  is the gradient strength of the quadrupole field  $g = \frac{\partial B_y}{\partial z} = \frac{\partial B_z}{\partial y}$  above the wire center. The trap position is therefore given in terms of the experimentally determined parameters by

$$\begin{aligned} z &= (B_y^o - B_y(z = 0)) / g + \alpha_y / g I_y \\ y &= B_z^o / g + \alpha_z / g I_z \end{aligned}$$

The determination of the field constants has been done in three steps. First, the center position  $y = 0$  is determined at a height  $z$  of  $\approx 20\mu\text{m}$ . As the imaging setup that has been used only had a view on the  $y - z$  plane, a direct measurement of the  $y$  position is not possible. Instead, the change of the gradient strength  $g$  with the  $y$  position has been used. Due to the mirror symmetry of the rectangular wire, the magnetic field gradient  $g(y)$  is a symmetric function. As

the gradient is directly proportional to the transverse oscillator frequency of the trapping potential  $\omega_{\perp}$ , small changes in the gradient can be probed by transverse center of mass oscillations of a trapped condensate (see section 4.5). This oscillation mode has an extremely high quality factor and is therefore well suited for precision measurements. In order to resolve small changes in the oscillator frequency  $\omega(g)$  an oscillation has been excited at different positions  $y$  and the amplitude  $A(T)$  has been detected after a fixed time  $T$ . A change in the amplitude  $A(T)$  is then related to a change in the frequency by  $A(T, g) = A_0 \cos(\omega(g)T)$ . The phase change of the cosine function can be directly related to the trap frequency

$$\omega(g) = \frac{1}{T} \arccos \frac{A(T, g)}{A_0} \quad (2.16)$$

The experimental result of this procedure is shown in figure 2.24.

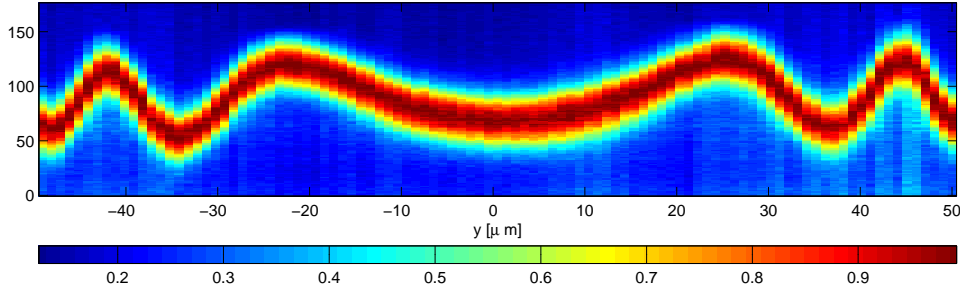


Figure 2.24: *Change in amplitude of a transverse oscillation due to a change of the  $y$  position.* The signal encoded by the colormap is obtained from an average of the atomic column density over the longitudinal direction after  $\approx 8$ ms time of flight. The oscillation time is  $T = 9$ ms at a distance of  $h \approx 20\mu\text{m}$  above wire **a** which was driven with 400mA.

From a quadratic fit to the phase change of the oscillation amplitude, the center position above the wire can be determined. The fit to the data of figure 2.24 is shown in figure 2.25. By this analysis the position of the wire center has been determined with an accuracy of  $\pm 2\mu\text{m}$ .

In the second step of the position calibration, the absolute height above the wire center has been measured for a series of different magnetic bias fields  $B_y$  by a reflection measurement, using the gold surface as a mirror (see chapter 5). When illuminating the absorbing cloud by a collimated beam that is slightly inclined towards the mirror plane, an imaging system after the mirror that is focused on the plane containing the atomic cloud and the center of the test wire will generate two focused images of the object. The relevant beam paths are sketched in figure 2.26 a. For the first image, the illuminating wave is first reflected by the mirror surface and then passes

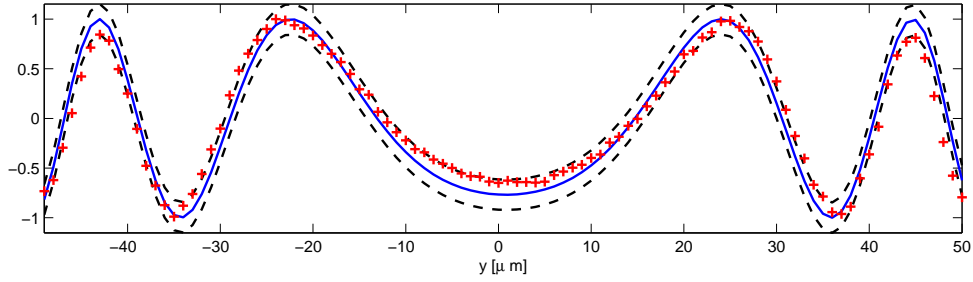


Figure 2.25: *Quadratic phase change.* Model fitted to the center of mass position (blue line) of the data (red crosses) in figure 2.24:  $A(y) = \cos a + by + cy^2$ . Obtained parameters  $a = -8.72 \pm 0.06$ ,  $b = (-7.4 \pm 1.46)10^{-3} \mu\text{m}^{-1}$ ,  $c = (4.5 \pm 0.3)10^{-3} \mu\text{m}^{-2}$ . Resulting error in the center position  $\pm 2 \mu\text{m}$ .

through the absorber (blue rays). For the second, the illuminating wave first passes the absorber and then reflects from the surface (black rays). Of these two images, one shows the cloud at a distance  $h$  above the surface, the other at a distance  $h$  below. The separation between the two corresponds to twice the distance of the atomic cloud above the surface.

However, as this procedure measures the position of the cloud relative to the surface height level, where the mirror image is reflected, the topography of the chip surface has to be taken into account. The changing height level between adjacent wires results in a discontinuous jump of the image position when the point of reflection moves over such an edge. This transition occurs for wires **a** and **b** in the situation sketched by figure 2.26 a and b (black beam paths). Additionally, shadowing and diffraction by wire edges causes blind areas where the beam that is reflected by the surface before passing the cloud is blocked by the obstacles. This situation is encountered for wires **a** and **c** in the geometry sketched by 2.26 a and c (blue beam paths). A height calibration scheme taking into account all these complications has been implemented as follows.

Absorption images have been acquired for a series of distances  $h$  above the chip surface. The normalized difference  $c(x, z)$  between an image with  $I'(x, z)$ , and without  $I_0(x, z)$  the cloud is calculated  $c = (I_0 - I')/I_0$ . A transverse section through such a picture clearly shows two maxima in the absorption signal resulting from the two images of the cloud. A typical section is shown in figure 2.27. The peaks around the maxima do not necessarily have a Gaussian shape. As the chip surface acts as an aperture which blocks an entire half space diffraction cannot be avoided for imaging close to the mirror surface. Instead of assuming a particular model that predicts the exact peak shape, an intuitive and largely model free approach may be used for the determination of the distance between the two maxima. The left half of the cross section data is moved over the right half of the same data set until the two subsets

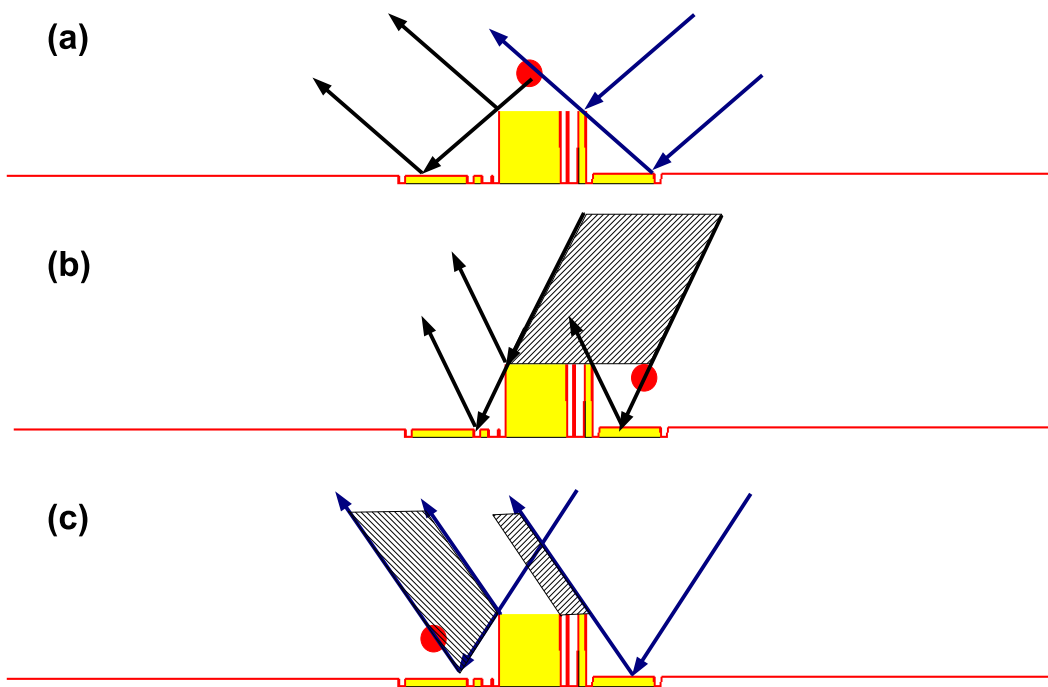


Figure 2.26: *Reflection imaging above different wires.* The figure shows a side view onto the cloud which is colored in red. The x axis (longitudinal scan direction) runs into the depicted cross-sectional plane. The wire layout of the chip is drawn in yellow. The imaging beam enters from right and is detected by an imaging system on the left.

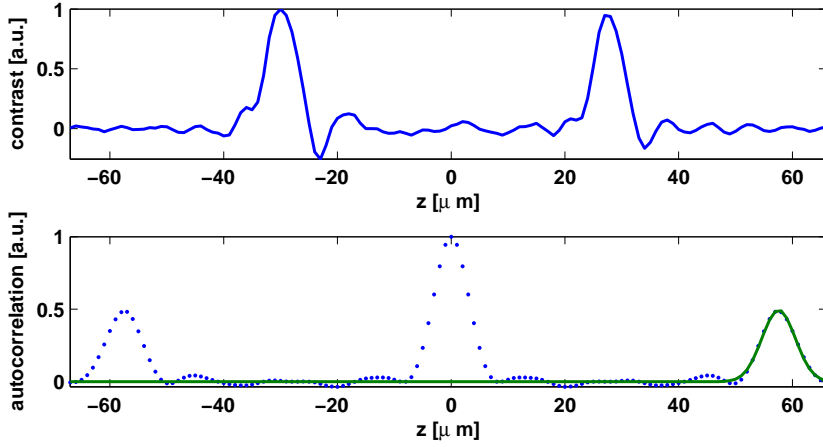


Figure 2.27: *Transverse section of an absorption picture and its autocorrelation function.* **Top panel:** Transverse cross section through an absorption picture. The absorption contrast  $c = (I_0 - I')/I_0$  is scaled to a maximum value of one. **bottom panel:** Autocorrelation signal of the absorption signal in the top panel.

have the best overlap. This procedure only relies on a symmetry of the left and the right half of the data which is secured by the mirror geometry. Formally, the autocorrelation function of the signal is computed. Figure 2.27 shows this function in the lower panel for the signal which graph is shown in the panel above. In contrast to the absorption signal itself the autocorrelation function has a nearly Gaussian shaped maximum, also in the presence of diffraction. A Gaussian fit has been used to determine the position of the side maximum which then corresponds to the height of the cloud.

The autocorrelation method fails however as soon as the two peaks in the absorption signal start to overlap. A transverse section in this regime is shown in figure 2.28. In this regime a sum of two Gaussian functions has been fitted to the double peak structure.

The transverse profile data for different height levels above the three test wires are shown, assembled into three pictures, in figure 2.29. In these pictures there are two different kinds of breaks visible in the straight lines that are formed by the absorption maxima. The maxima on the left hand side of the pictures correspond to the beam path, where the imaging light is reflected by the surface before encountering the cloud. For such a path only shadowing of the image, but no jump in the maximum position occurs. The breaks in the lines of the top and bottom picture are consistent with the surface structure depicted in figure 2.26 for an incident beam that hits the surface under an angle of  $\theta = 6.5^\circ$  measured towards the chip sur-

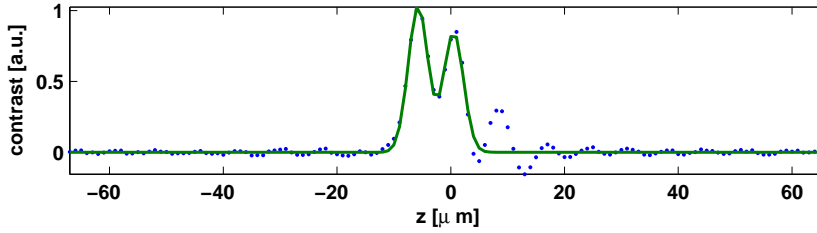


Figure 2.28: *Overlapping absorption maxima.* In the regime of overlapping peaks a sum of two Gaussian curves has been fitted to the data.

face. (Expected break points from geometric optics at  $h = 21\mu m$  for wire **a** and at  $h = 56\mu m$  and  $h = 23\mu m$  for wire **c**). The maxima on the right hand side belong to the imaging geometry, where the imaging beam enters the cloud before being reflected. In this situation a jump in the apparent height occurs when the point of reflection moves across a discontinuity in the surface height. (Expected jumps at  $h = 11\mu m$  for wire **a**, at  $h = 26\mu m$  and  $h = 6\mu m$  for wire **b**.)

These data sets have been used for the height calibration of the microscopy scans. For each wire, the height has been extracted by the autocorrelation procedure in the regime where the maxima are clearly separable. A straight line has been fitted to the and the resulting slope has then been used as a constraint for a straight line fit in the regime where the double Gaussian method has been used. By this combined procedure the position of the magnetometry scans has been determined to be  $h = (3.5 \pm 0.8)\mu m$ ,  $h = (3.8 \pm 0.4)\mu m$  and  $h = (4.0 \pm 0.6)\mu m$  for wires **a** to **c**. The indicated errors are  $1\sigma$  ranges taking into account statistical errors only. The combined result of both methods is shown in figures 2.30 to 2.32.

In the third and last step of the position calibration, the full magnetic field formula above a rectangular wire has been implemented (see section 2.6.1) to compute the appropriate bias field values also far from the constant gradient regime in the trap center. The bias field constant  $\alpha_z$  which controls the scaling of the  $z$  axis has been determined indirectly by adjusting it to a value that the scan height of  $\approx 4\mu m$  does not differ close to the wire edge ( $\approx 90\mu m$  from the center) from the value at the wire center. This procedure uses the fast rotation of the quadrupole axis close to the wire edge. Directly above the edge the height is determined nearly entirely by the  $z$  component of the bias field which translates a change in  $B_z$  into a measurable response of the height level. The error in the magnetic field  $\Delta B_z$  can be determined there from the error in the height level  $\Delta z$  by  $\Delta B_z = \frac{\partial B_z}{\partial z} \Delta z$ . Assuming the magnetic field of a rectangular wire the computed gradients  $g' = \frac{\partial B_z}{\partial z}$  close to the wire edge and  $g = \frac{\partial B_z}{\partial y}$  above the wire center have been used to estimate a relative error of the  $y$  position in the center of the wire to about 10%. A more precise error

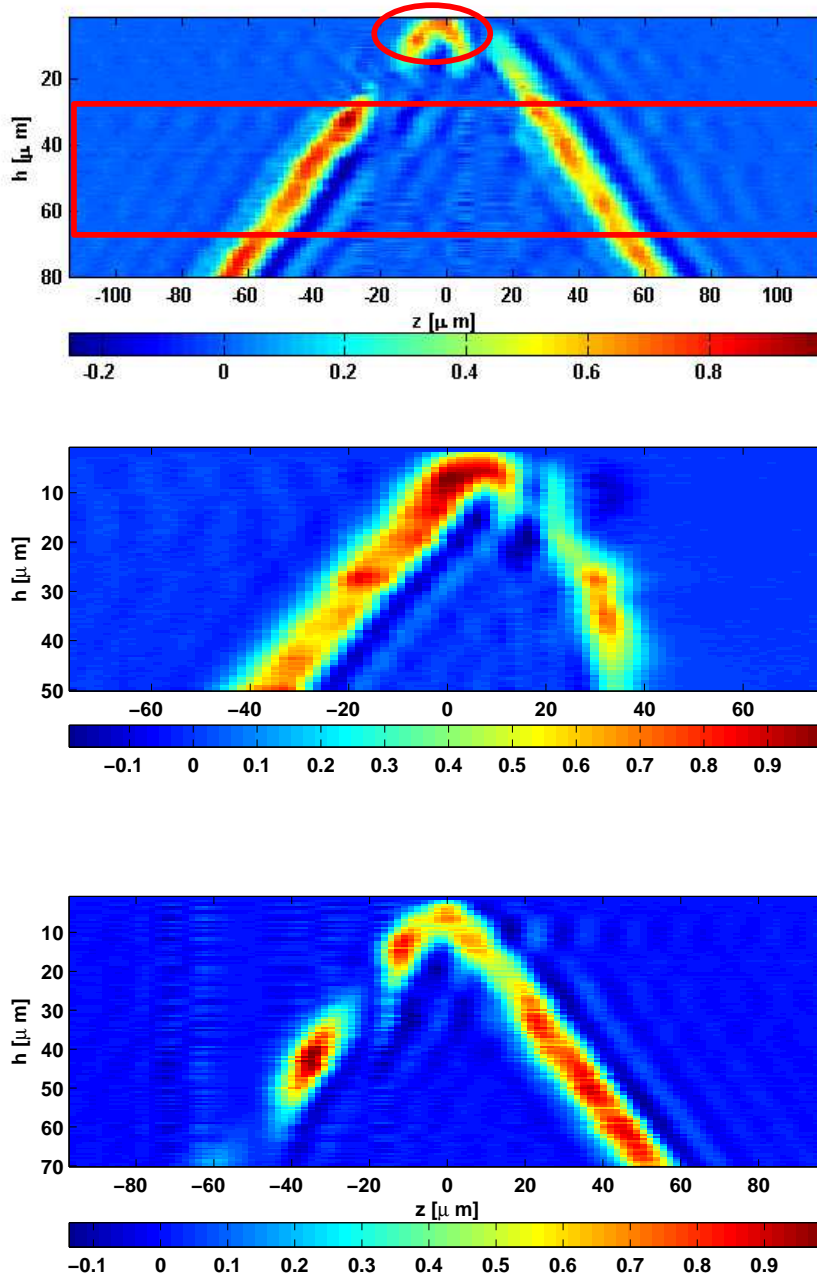


Figure 2.29: *Transverse absorption profile for a series of different distances above the three test wires.* The colormap encodes the absorption contrast  $c$  in arbitrary units. The  $h$  coordinate is the experimentally controlled parameter that adjusts the height of the magnetic trap by appropriate homogenous magnetic fields. The  $z$  coordinate is the length scale in the acquired absorption pictures. The images correspond to the wires **a** to **c** from top to bottom.

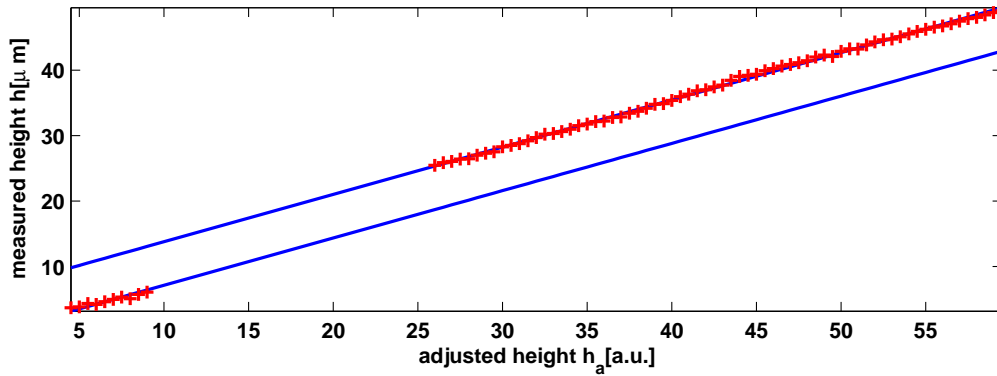


Figure 2.30: Wire **a**. Autocorrelation height  $h = ah_a + b$ ,  $a = 0.72 \pm 0.07$ ,  $b = (6.6 \pm 0.3)\mu m$ . Gaussian height  $h = ah_a + b$ ,  $b = (-0.1 \pm 0.3)\mu m$ . Scan position (adjusted height 5)  $h = (3.5 \pm 0.8)\mu m$  (statistical error).

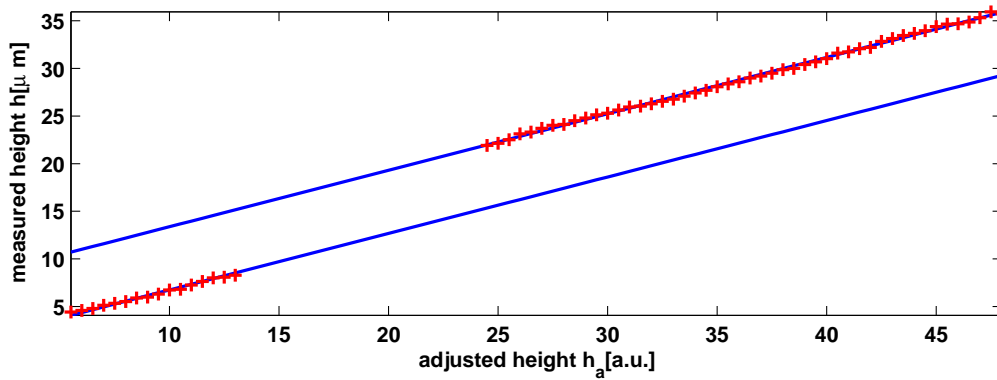


Figure 2.31: Wire **b**. Autocorrelation height  $h = ah_a + b$ ,  $a = 0.59 \pm 0.01$ ,  $b = (7.5 \pm 0.3)\mu m$ . Gaussian height  $h = ah_a + b$ ,  $b = (0.8 \pm 0.1)\mu m$ . Scan position (adjusted height 5)  $h = (3.8 \pm 0.4)\mu m$  (statistical error).

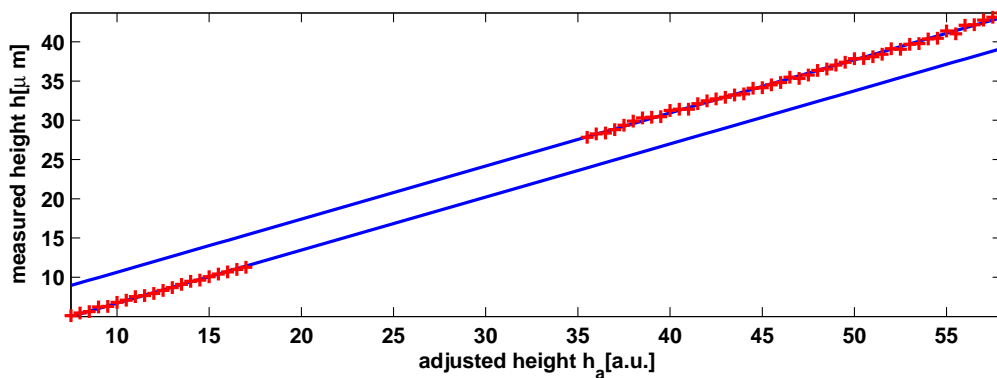


Figure 2.32: Wire **c**. Autocorrelation height  $h = ah_a + b$ ,  $a = 0.68 \pm 0.01$ ,  $b = (3.88 \pm 0.5)\mu m$ . Gaussian height  $h = ah_a + b$ ,  $b = (-0.07 \pm 0.05)\mu m$ . Scan position (adjusted height 6)  $h = (4.0 \pm 0.6)\mu m$  (statistical error).

estimation is not possible by this method, as  $g'$  depends sensitively on the  $y$  position close to the wire edge.

### 2.5.3 Magnetic Field

The last quantity that is needed for a calibrated magnetometry is the magnetic field value  $B_y$  which is produced by the homogenous part of the current density. Two possible error source for the exact determination of this quantity have been taken into account. An inaccuracy in the positioning of the cloud will lead to a wrong estimate. Figure 2.33 shows the relative change of the magnetic field magnitude with the displacement from the central scan position at  $h = 3.5\mu\text{m}$  above the wire center. Over the whole scan range, the field changes by less than 5%. As this error

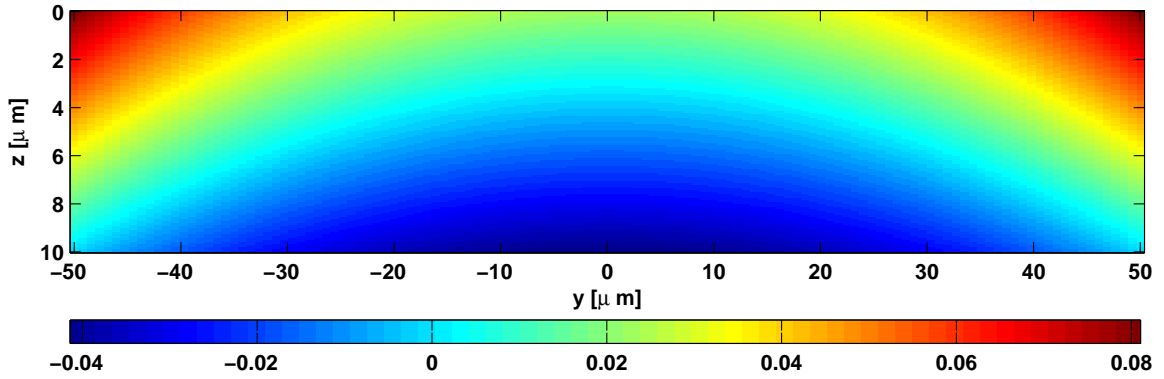


Figure 2.33: *Relative field strength variation at the scan height.*  $\Delta B/B$  for the scan center at  $h = 3.5\mu\text{m}$  above the center of a  $2.5\mu\text{m}$  thick wire. The relative change is approximately the same for a  $0.250\mu\text{m}$  thick wire. The absolute field values at the scan center are 5.48G 5.52G respectively for  $I_{\text{Chip}} = 180\text{mA}$ . (For the magnetic field of the rectangular wire see section 2.6.1)

does significantly deteriorate the total error of the magnetic field angle the the bias field has been assumed to be a constant.

## 2.6 Appendix

### 2.6.1 Magnetic field of a rectangular wire

The magnetic field produced by a wire of rectangular cross section may be directly computed by Biot-Savart's law. This is equivalent to partitioning the wire into many thin wires and summing up their contributions to the total field. For a wire of width  $w$  and height  $h$  centered at  $x = 0$ ,  $y = 0$  and running along the  $z$  direction the magnetic field calculated from

$$\mathbf{B}(y, z) = \frac{\mu_0 j}{2\pi} \int_{-\frac{h}{2}}^{\frac{h}{2}} dz' \int_{-\frac{w}{2}}^{\frac{w}{2}} dy' \frac{-(z - z')\mathbf{e}_y + (y - y')\mathbf{e}_z}{(y - y')^2 + (z - z')^2} \quad (2.17)$$

yields the two components

$$\begin{aligned} B_x(x, y) = \frac{\mu_0 I}{4\pi w h} & \left( 2 \left( y - \frac{h}{2} \right) \left( \arctan \frac{x + \frac{w}{2}}{y - \frac{h}{2}} - \arctan \frac{x - \frac{w}{2}}{y - \frac{h}{2}} \right) - \right. \\ & 2 \left( y + \frac{h}{2} \right) \left( \arctan \frac{x + \frac{w}{2}}{y + \frac{h}{2}} - \arctan \frac{x - \frac{w}{2}}{y + \frac{h}{2}} \right) + \\ & \left( x - \frac{w}{2} \right) \log \frac{(x - \frac{w}{2})^2 + (y + \frac{h}{2})^2}{(x - \frac{w}{2})^2 + (y - \frac{h}{2})^2} + \\ & \left. \left( x + \frac{w}{2} \right) \log \frac{(x + \frac{w}{2})^2 + (y - \frac{h}{2})^2}{(x + \frac{w}{2})^2 + (y + \frac{h}{2})^2} \right) \end{aligned} \quad (2.18)$$

and  $B_y(x, y)$  which is obtained from  $B_x$  by the following substitution rule

$$\begin{aligned} x & \rightarrow y \\ y & \rightarrow x \\ B_x & \rightarrow -B_y \end{aligned} \quad (2.19)$$

. The gradient components of the field are

$$\frac{\partial B_x}{\partial y} = \frac{\mu_0 j}{2\pi} \left( \arctan \frac{x - \frac{w}{2}}{y - \frac{h}{2}} - \arctan \frac{x + \frac{w}{2}}{y - \frac{h}{2}} - \arctan \frac{x - \frac{w}{2}}{y + \frac{h}{2}} + \arctan \frac{x + \frac{w}{2}}{y + \frac{h}{2}} \right) \quad (2.20)$$

$$\frac{\partial B_x}{\partial z} = \frac{\mu_0 j}{4\pi} \left( \log \frac{(w - 2x)^2 + (h + 2y)^2}{(w - 2x)^2 + (h - 2y)^2} + \log \frac{(w + 2x)^2 + (h - 2y)^2}{(w + 2x)^2 + (h + 2y)^2} \right) \quad (2.21)$$

from which the quadrupole strength can be extracted by

$$g = \sqrt{\left( \frac{\partial B_x}{\partial x} \right)^2 + \left( \frac{\partial B_x}{\partial y} \right)^2} \quad (2.22)$$

In the limit of a thin wire ( $h \rightarrow 0$ ) the field reduces to

$$B_x(x, y) = -\frac{\mu_0 I}{2\pi w} \left( \arctan \frac{x + \frac{w}{2}}{y} - \arctan \frac{x - \frac{w}{2}}{y} \right) \quad (2.23)$$

$$B_y(x, y) = \frac{\mu_0 I}{2\pi w} \frac{1}{2} \log \frac{(x + \frac{w}{2})^2 + y^2}{(x - \frac{w}{2})^2 + y^2} \quad (2.24)$$

## 2.6.2 Fourier Spectrum

The function  $\beta(x, y)$  defined on the rectangle  $[-L_x/2 < x < L_x/2] \times [-L_y/2 < y < L_y/2]$  can be expanded into a sum of plain waves

$$\beta(x, y) = \frac{L_x L_y}{(2\pi)^2} \int_{-\pi/\Delta x}^{\pi/\Delta x} dk_x \int_{-\pi/\Delta y}^{\pi/\Delta y} dk_y \exp [i(k_x x + k_y y)] \beta(k_x, k_y) \quad (2.25)$$

$$\beta(k_x, k_y) = \frac{1}{L_x L_y} \int_{-L_x/2}^{L_x/2} dx \int_{-L_y/2}^{L_y/2} dy \exp [-i(k_x x + k_y y)] \beta(x, y)$$

In the case of a bandwidth limited function,  $f(x, y)$  is completely defined by its values at  $x = \Delta x n$  and  $y = \Delta y l$  with  $-N_x/2 < n < N_x/2 - 1$  and  $-N_y/2 < l < N_y/2 - 1$  and the Fourier transform is given by the discrete sum

$$\beta(m, k) = \frac{1}{N_x N_y} \sum_{n=-N_x/2}^{N_x/2-1} \sum_{l=-N_y/2}^{N_y/2-1} \exp \left[ -i \left( \frac{\Delta x 2\pi}{L_x} m n + \frac{\Delta y 2\pi}{L_y} k l \right) \right] \beta(x, y) \quad (2.26)$$

The total variance  $\beta_{\text{rms}}^2$  of  $\beta(x, y)$  can be computed equivalently in Fourier and real space (Parseval's theorem)

$$\begin{aligned}
\beta_{\text{rms}}^2 &= \frac{1}{L_x L_y} \int_{-L_x/2}^{L_x/2} dx \int_{-L_y/2}^{L_y/2} dy |\beta(x, y)|^2 \\
&= \frac{1}{N_x N_y} \sum_{n=-N_x/2}^{N_x/2-1} \sum_{l=-N_y/2}^{N_y/2-1} |\beta(n, l)|^2 \\
&= \sum_{m=-N_x/2}^{N_x/2-1} \sum_{k=-N_y/2}^{N_y/2-1} |\beta(m, k)|^2 \\
&= \frac{L_x L_y}{(2\pi)^2} \int_{-\pi/\Delta x}^{\pi/\Delta x} dk_x \int_{-\pi/\Delta y}^{\pi/\Delta y} dk_y |\beta(k_x, k_y)|^2
\end{aligned} \tag{2.27}$$

### 2.6.3 Gaussian Noise

The current density is determined by

$$j_y(\mathbf{k})/j_0 = -\frac{1}{2} \frac{\sigma_{\mathbf{k}}}{\sigma_0} \sin 2\theta \tag{2.28}$$

assuming the noise model  $\frac{\sigma_{\mathbf{k}}}{\sigma} = \exp(-k^2(l/2\sqrt{2})^2)$ , the normalized correlation function is given by

$$g(r) = \exp\left(-\frac{r^2}{l^2}\right) \tag{2.29}$$

which has the correlation length

$$\left(\int d^2\mathbf{x} g(|\mathbf{x}|) |\mathbf{x}|^2\right)^{1/2} = l \tag{2.30}$$

### 2.6.4 Error weighted mean value

Assume a set of  $N$  measurements  $x_i$  of known error  $\sigma_i$ . From these an estimate of the mean value that has the smallest error shall be constructed. The general mean value

$$\bar{x} = \sum_i c_i x_i \tag{2.31}$$

has the error

$$\sigma^2 = \sum_i c_i^2 \sigma_i^2 \quad (2.32)$$

where the coefficients  $c_i$  are restricted by  $\sum c_i = 1$ . In order for the total error to be minimal the equation

$$\frac{\partial}{\partial c_i} \left( \sigma^2 - \lambda \sum_i c_i \right) = 0 \quad (2.33)$$

has to be fulfilled which amounts to

$$c_i = \frac{\lambda}{2\sigma_i^2} = \frac{1}{\sigma_i^2} / \sum_i \frac{1}{\sigma_i^2} \quad (2.34)$$

. For this choice of coefficients the error of the mean value is given by

$$\sigma^2 = \sum_i \frac{1}{\sigma_i^4} \sigma_i^2 / \left( \sum_i \frac{1}{\sigma_i^2} \right)^2 = 1 / \sum_i \frac{1}{\sigma_i^2} \quad (2.35)$$

# Bibliography

- [1] Sondheimer,E.H. The mean free path of electrons in metals. *Adv. Phys.* **1**, 1 (1952)
- [2] Chambers,R.G. The Conductivity of Thin Wires in a Magnetic Field. *Proc. R. Soc. London, Ser. A* **202**, 378 (1950)
- [3] Mayadas,A.F. Shatzkes,M. Electrical-Resistivity Model for Polycrystalline Films: the Case of Arbitrary Reflection at External Surfaces. *Phys. Rev. B* **1**,1382 (1970)
- [4] Landauer,R. Spatial Variation of Currents and Fields Due to Localized Scatterers in Metallic Conduction. *IBM J.Res. Dev.* **1**, 223 (1957)
- [5] Steinhögl,W. et al. Size-dependent resistivity of metallic wires in the mesoscopic range. *Phys. Rev. B* **66**, 075414 (2002)
- [6] Schneider,M.A. et al. Current transport through single grain boundaries: A scanning tunneling potentiometry study. *Appl. Phys. Lett.* **69**, 1327 (1996)
- [7] Wildermuth,S. et al. Microscopic magnetic-field imaging. *Nature* **435**, 440 (2005)
- [8] Bonn,D.A. Are high-temperature superconductors exotic? *Nature Physics* **2**, 159 (2006)
- [9] Ilani,S. et. al Microscopic Structure of the Metal-Insulator Transition in Two Dimensions. *Science* **292**, 1354 (2001)
- [10] Feist,J. et al. Nanowires with Surface Disorder: Giant Localization Lengths and Quantum-to-Classical Crossover. *Phys. Rev. Lett.* **97**, 116804 (2006)
- [11] The chip was fabricated at The Weiss Family Laboratory for nano-Scale Systems at Ben-Gurion University, Israel, [www.bgu.ac.il/nanofabrication](http://www.bgu.ac.il/nanofabrication).
- [12] Japha,Y. et al. *submitted to PRL*
- [13] Schneider,S. et al. Bose-Einstein condensation in a simple microtrap. *Phys. Rev. A* **67**, 023612 (2003)

---

## 3 Current Imaging and Defect Sensing

---

### 3.1 Introduction

Any oscillating charge or current distribution radiates electromagnetic waves that carry characteristic information about the source distribution. In general, imaging is nothing but the reconstruction of the generating charge or current density from the radiated wave-field. This concept and the underlying principles cover a much broader range than just the optical frequency domain. Even static sources produce an electromagnetic field that can be treated within the same framework as the fields in the optical case. Major differences come into play only with the availability of optical elements like lenses or mirrors and detectors.

In this spirit the imaging of static currents in a thin metallic film will be examined in this chapter. The first section is concerned with the generation of the magnetic field, its free space propagation and the question what information may be retrieved from a field measurement outside the metallic film. The treatment has been inspired by [1]. The picture presented here is however much more general and substantially different from this early treatment.

In the second section, several models for the sources of current deviations in a grainy film will be developed. These models allow to link magnetic field measurements to those material properties that influence the charge transport. For the thin (1-D) wire geometry treatments taking into account boundary corrugations have already been given by [2, 3]. However, here the focus is on the thin films, which are the relevant case for spatially resolved current microscopy. An extension to the model

presented here that also takes into account the finite width of the thin film wires has been developed by [4].

## 3.2 Magnetic Field Propagation

A quasi-static current density flowing inside a metal-sheet can be traced from outside in two possible ways. By scanning the surface with a voltage probe information on the local charge distribution may be obtained. Assuming a diffusion driven transport the current density can be linked to gradients in the charge density. Such a procedure is indirect and relying on a specific transport model. The most immediate connection to the current density is provided by the magnetic field. Any current distribution generates a characteristic field independently of the material and its specific kind of transport mechanism. This very favorable property provokes the question in how far a complete reconstruction of the current density is possible once the magnetic field outside the conductor is known. The quantitative answer to this question will be given in the following section.

### 3.2.1 Wavepropagation: Near and Far Field

Maxwell's equations imply that each magnetic field  $\mathbf{B}$  is generated by a current density  $\mathbf{j}$  according to the wave equation

$$\nabla^2 \mathbf{B} - \frac{1}{c^2} \frac{\partial^2 \mathbf{B}}{\partial t^2} = -\mu_0 \nabla \times \mathbf{j} \quad (3.1)$$

As any time dependence of the fields may be represented by a linear superposition of harmonic functions it is no restriction to assume a harmonic time dependence from the beginning

$$\begin{aligned} \mathbf{B}(\mathbf{x}, t) &= \mathbf{B}(\mathbf{x}) e^{i\omega t} \\ \mathbf{j}(\mathbf{x}, t) &= \mathbf{j}(\mathbf{x}) e^{i\omega t} \end{aligned}$$

Substitution of this specific form into the wave equation reduces it to the Helmholtz equation

$$\nabla^2 \mathbf{B} + \kappa^2 \mathbf{B} = -\mu_0 \nabla \times \mathbf{j} \quad (3.2)$$

where  $\kappa = \frac{\omega}{c}$ . The main emphasis in the treatment will be put on the thin film geometry. It is assumed that the current density is confined to a thin conductive layer of thickness  $d$  that is centered around the  $z = 0$  plain. The magnetic field is measured in the detection plain at  $z = h$ . The propagation process from the source to this plain can be formulated most clearly if both field and current density are decomposed into a superposition of plane (2D) Fourier modes

$$\begin{aligned}\mathbf{j}(\mathbf{x}, z) &= \frac{1}{2\pi} \int d^2\mathbf{k} \mathbf{j}_{\mathbf{k}}(z) e^{i\mathbf{k}\cdot\mathbf{x}} \\ \mathbf{B}(\mathbf{x}, z) &= \frac{1}{2\pi} \int d^2\mathbf{k} \mathbf{B}_{\mathbf{k}}(z) e^{i\mathbf{k}\cdot\mathbf{x}}\end{aligned}$$

.  $\mathbf{x}$  and  $\mathbf{k}$  are two-component vectors, specifying position and wavevector in the  $x$ - $y$  plain. In order to find the relation between current and field modes the Fourier decomposition is substituted into the Helmholtz equation

$$\left( \kappa^2 - k^2 + \frac{\partial^2}{\partial z^2} \right) \mathbf{B}_{\mathbf{k}}(z) = -\mu_0 \left( i\mathbf{k} \times \mathbf{j}_{\mathbf{k}}(z) + \mathbf{e}_z \frac{\partial \mathbf{j}_{\mathbf{k}}(z)}{\partial z} \right) \quad (3.3)$$

. This is a linear, ordinary, inhomogeneous differential equation. Its solution can be formulated in terms of a Greens function  $G(z, z_0)$  that is determined by the response to a delta function source term

$$\left( \kappa^2 - k^2 + \frac{\partial^2}{\partial z^2} \right) G(z, z_0) = -\delta(z - z_0)$$

and appropriate boundary conditions. For  $z \neq z_0$  the right hand side vanishes and the Greens function must be a linear superposition of exponentials. If we further restrict the solutions to those physically meaningful cases where  $G(., .)$  remains finite for any  $k$  and  $|z| \rightarrow \infty$  the Greens function must be of the form

$$G(z, z_0) = \begin{cases} a_k e^{i\sqrt{\kappa^2 - k^2}(z - z_0)} & \text{for } z \geq z_0 \\ b_k e^{-i\sqrt{\kappa^2 - k^2}(z - z_0)} & \text{for } z < z_0 \end{cases}$$

These two solutions have to be joined at  $z = z_0$  in a way that results in the demanded  $\delta$ -function of the second derivative. This can be accomplished by

$$G(z, z_0) = -\frac{e^{i\sqrt{\kappa^2 - k^2}|z - z_0|}}{2i\sqrt{\kappa^2 - k^2}} \quad (3.4)$$

Using this Greens function the solution to (3.3) for a general source term can now be written in terms of the linear superposition of shifted Greens functions

$$\begin{aligned}\mathbf{B}_{\mathbf{k}}(z) &= -\frac{\mu_0 i\mathbf{k}}{2i\sqrt{\kappa^2 - k^2}} \times \int_{-\frac{d}{2}}^{\frac{d}{2}} dz_0 \mathbf{j}_{\mathbf{k}}(z_0) e^{i\sqrt{\kappa^2 - k^2}|z - z_0|} \\ &- \frac{\mu_0 \mathbf{e}_z}{2i\sqrt{\kappa^2 - k^2}} \times \int_{-\frac{d}{2}}^{\frac{d}{2}} dz_0 \frac{\partial \mathbf{j}_{\mathbf{k}}(z_0)}{\partial z_0} e^{i\sqrt{\kappa^2 - k^2}|z - z_0|}\end{aligned}$$

Integration by parts in the second term allows the simplification

$$\begin{aligned} \mathbf{B}_{\mathbf{k}}(z) &= -\frac{\mu_0 i \mathbf{k}}{2i\sqrt{\kappa^2 - k^2}} \times \int_{-\frac{d}{2}}^{\frac{d}{2}} dz_0 \mathbf{j}_{\mathbf{k}}(z_0) e^{i\sqrt{\kappa^2 - k^2}|z - z_0|} \\ &\quad - \frac{\mu_0 \mathbf{e}_z}{2} \times \int_{-\frac{d}{2}}^{\frac{d}{2}} dz_0 \mathbf{j}_{\mathbf{k}}(z_0) \text{sign}(z - z_0) e^{i\sqrt{\kappa^2 - k^2}|z - z_0|} \end{aligned}$$

For an observation point above the slab ( $z > z_0$ ) the sign-function in the second term may be skipped and the expression further simplifies to

$$\mathbf{B}_{\mathbf{k}}(z) = -\frac{\mu_0 d}{2} \left( \frac{\mathbf{k}}{\sqrt{\kappa^2 - k^2}} + \mathbf{e}_z \right) \times \bar{\mathbf{j}}_{\mathbf{k}} e^{i\sqrt{\kappa^2 - k^2}(z - \frac{d}{2})} \quad (3.5)$$

where the effective two dimensional current density has been introduced as

$$\bar{\mathbf{j}}_{\mathbf{k}} = \frac{1}{d} \int_{-\frac{d}{2}}^{\frac{d}{2}} dz_0 \mathbf{j}_{\mathbf{k}}(z_0) e^{i\sqrt{\kappa^2 - k^2}(\frac{d}{2} - z_0)} \quad (3.6)$$

. These are the key equations that relate the detected field to the source current density. They are the starting point for a spatial reconstruction or imaging of a current density.

Considering the spatial dependence of  $\mathbf{B}_{\mathbf{k}}(z)$ , the connection from the current density to the magnetic field can be viewed as a two step process. First, a local magnetic field is generated directly above the current layer

$$\mathbf{B}_{\mathbf{k}}(d/2) = -\frac{\mu_0 d}{2} \left( \frac{\mathbf{k}}{\sqrt{\kappa^2 - k^2}} + \mathbf{e}_z \right) \times \bar{\mathbf{j}}_{\mathbf{k}}$$

and second, this field propagates from the source to the detection plain

$$\mathbf{B}_{\mathbf{k}}(z) = \mathbf{B}_{\mathbf{k}}(d/2) e^{i\sqrt{\kappa^2 - k^2}(z - \frac{d}{2})}$$

Both, generation and propagation show two different regimes depending on whether the plain wave modes have a wave vector  $|\mathbf{k}| < \kappa$  or  $|\mathbf{k}| > \kappa$ . For the first case, the propagation is described by a pure phase factor. For the second, the exponential turns into a real valued damping term.

This qualitative difference marks the border between propagating waves that travel away from the source and evanescent waves that are bound to the near field. The usual optical imaging is performed in the far field. In this regime the propagation just results in a unitary transformation of the wavefront. Such a transformation has a unique inverse and the propagation can be reversed by a lens or mirror system. In the near field case, the propagation process is non unitary. The exponential decay term performs an irreversible low pass filter on the wavefront. Spatial information is

lost with increasing distance to the source plain. The cross over point between the two regimes is tuned by the angular frequency  $\omega$ . The case of static fields is obtained by the limiting procedure  $\omega \rightarrow 0$  which has the consequence that all modes become evanescent. Figure (3.1) depicts the cross over between the near and far field regime for the magnetic field above a thin rectangular wire. As the near field regime is

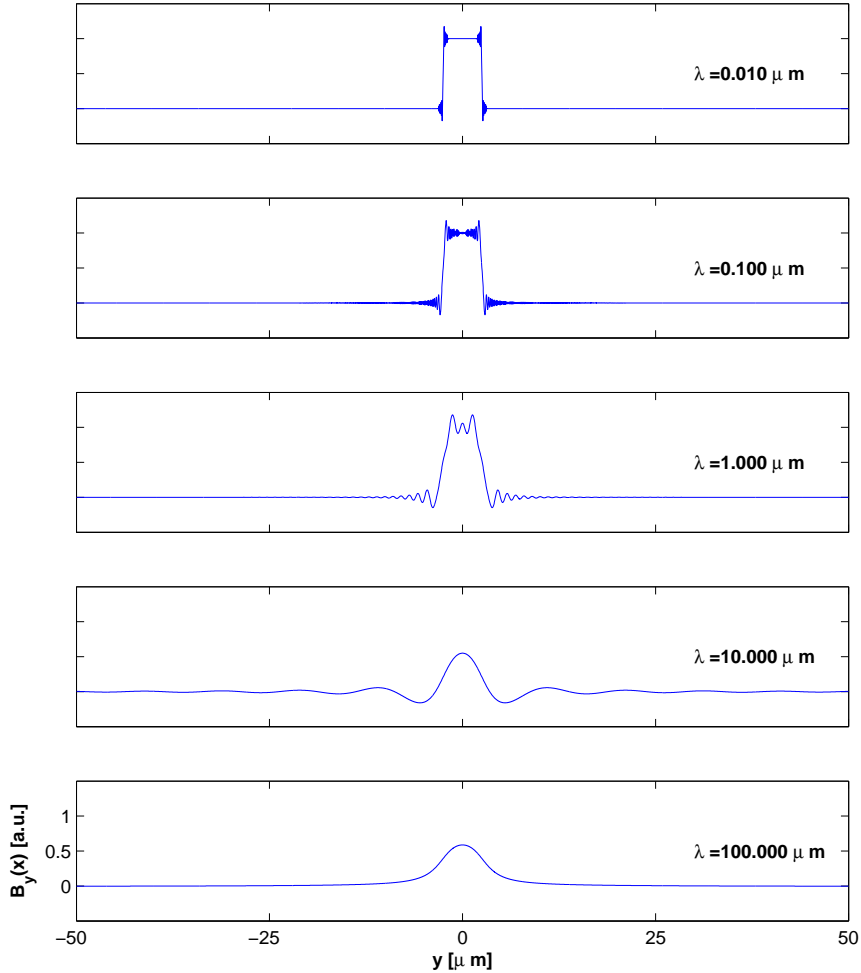


Figure 3.1: *Imaging from near to far field domain.* The series of figures shows the  $y$  component of the magnetic field  $2\mu\text{m}$  above a thin rectangular wire of  $5\mu\text{m}$  width that runs along the  $x$  direction. By changing  $\lambda = \frac{2\pi}{\kappa}$  at a fixed observation height, the detected field crosses from the far to the near field regime from top to bottom.

approached the typical diffraction pattern disappears where the phase factor turns into a real valued damping term.

It has been shown now that the imaging of static currents may be conceived as a special kind of near field microscopy. As this domain will be of exclusive concern in

the following discussions the imaging relations are restated for this case explicitly

$$\mathbf{B}_{\mathbf{k}}(z) = \frac{\mu_0 d}{2} \left( i \frac{\mathbf{k}}{k} - \mathbf{e}_z \right) \times \bar{\mathbf{j}}_{\mathbf{k}} e^{-k(z-\frac{d}{2})} \quad (3.7)$$

where

$$\bar{\mathbf{j}}_{\mathbf{k}} = \frac{1}{d} \int_{-\frac{d}{2}}^{\frac{d}{2}} dz_0 \mathbf{j}_{\mathbf{k}}(z_0) e^{-k(\frac{d}{2}-z_0)} \quad (3.8)$$

Returning to the question of the feasibility of a complete current reconstruction from the measured magnetic field, one can make out three potential obstacles.

The exponential decay term, introduced by the propagation process, can be, at least in principle, avoided by measuring the magnetic field close enough to the source plane that it can be neglected for the length scales of interest. A more fundamental limit is set by the thickness of the metallic film. As the magnetic field can only be probed outside the material the detected signal is always an average over the fields produced by the current at different height levels  $z$  within the wire. In order to resolve this ambiguous situation a specific model for the current flow inside the wire has to be assumed. This modelling that connects the effective current density to the real current density will be the concern of section 3.3. The third problem for a reconstruction is the appearance of the cross product between the effective current density and the vector  $(-i\frac{\mathbf{k}}{k} + \mathbf{e}_z)$ . A current component parallel to this vector does not generate a magnetic field. The next section shows how this problem can be resolved.

### 3.2.2 Uniqueness of the Effective Current Reconstruction

Judging from equation (3.7) alone one could be let to the conclusion that the connection between the magnetic field and the effective current density is not a one to one correspondence. This would mean that there are current distributions that result in no magnetic field. These zero field currents  $\bar{\mathbf{j}}_{\mathbf{k}}^0$  would be parallel to the vector  $(i\frac{\mathbf{k}}{k} - \mathbf{e}_z)$ . However, any current distribution has the additional restriction that it has to fulfill the charge conservation

$$\nabla \cdot \mathbf{j} = 0$$

. Translating it into Fourier space results in

$$i\mathbf{k} \cdot \mathbf{j}_{\mathbf{k}}(z) + \frac{\partial j_{\mathbf{k}}^z(z)}{\partial z} = 0$$

which can be integrated to yield the corresponding expression for the effective current density

$$\left( i \frac{\mathbf{k}}{k} - \mathbf{e}_z \right) \cdot \bar{\mathbf{j}}_{\mathbf{k}} = 0 \quad (3.9)$$

A zero field current density  $\bar{\mathbf{j}}_{\mathbf{k}}^0$  does therefore not exist.

This shows that the unique reconstruction of the effective current density is possible, if the magnetic field directly above the source plain is known. It is explicitly given by

$$\boxed{\bar{\mathbf{j}}_{\mathbf{k}} = \frac{2}{\mu_0 d} \frac{i\mathbf{k}}{k} \times \mathbf{B}_{\mathbf{k}}(d/2)} \quad (3.10)$$

Which can be checked by substitution into equation 3.7 and using the Maxwell equation  $\nabla \cdot \mathbf{B} = 0$ .

The only fundamental ambiguity of the current detection by magnetometry that can not be resolved in principle is the averaging procedure that reduces the current density to the effective two dimensional current density. In order to invert this relation and to obtain information on the transverse distribution of the current density inside the thin film, additional model assumptions on the current flow have to be made. In this spirit, the influence of different defects on the current density will now be presented in the following section.

## 3.3 Magnetometric Defect Detection

In a straight completely homogenous wire the current flow follows uniformly the wire direction. However, such a completely homogenous system is rarely encountered in the real world. Faults in the crystal structure and corrugations of the surface cause the current to deviate from its ideal path. The straight wire geometry is ideal to study such material defects. In the absence of any fluctuations in the current density, the magnetic field, generated by a straight wire points strictly perpendicular to the wire axis. A magnetic field sensor that is only sensitive to the field component along the wire axis can therefore detect a background free signal that is directly related to a local change of the current direction.

In the following section different perturbation scenarios will be discussed in detail and their influence on the local current direction is considered.

The adopted geometry that is assumed in this treatment is depicted in figure 3.2. A flat wire of thickness  $d$  is centered at  $z = 0$  and runs along the x-direction. The width

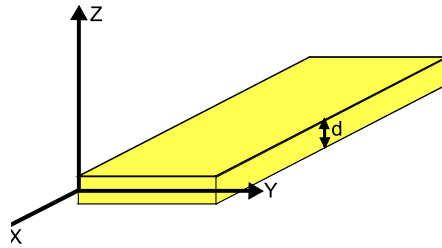


Figure 3.2: Choice of axis directions for the modelled chip wire.

of the wire shell be large compared to the thickness, so that the wire approximates the limiting case of a thin film. Effects that are connected to the finite width are assumed to be small and will be neglected throughout.

### 3.3.1 General properties

On macroscopic length scales the collective effect of many defects may be described by an effective ohmic conductivity that shows small spatial variations around the value of the homogenous bulk material. The current flow in such a system is deter-

mined by three equations:

$$\begin{aligned} \mathbf{j} &= \sigma \mathbf{E} \\ \nabla \cdot \mathbf{j} &= 0 \\ \nabla \times \mathbf{E} &= 0 \end{aligned} \tag{3.11}$$

the first is Ohm's law, the second expresses charge conservation and the third is a static Maxwell equation. In order to illustrate the interplay of these equations two simple examples will now be presented, before the general defect models are discussed.

Maybe the simplest non trivial situation is that of a sudden jump in the conductivity across a plane surface. In this model the conductivity of the material plays a similar role for the current density as the index of refraction does for an electromagnetic wave. The geometry of the problem is depicted schematically in figure 3.3. A thin plane parallel layer of conductivity  $\sigma + \Delta\sigma$  is embedded into the otherwise

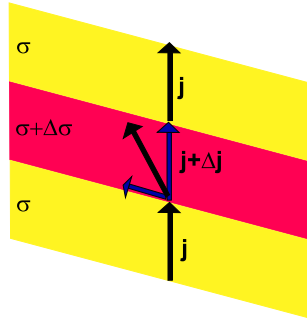


Figure 3.3: *Refraction of the current density.* Two regions of bulk conductivity  $\sigma$  are separated by a thin layer of lower conductivity  $\sigma + \Delta\sigma$ . This results in a refraction of the current density.

unperturbed bulk material of conductivity  $\sigma$ .

The equations 3.11 enforce certain continuity conditions on the current density and the electric field that have to hold across the discontinuous change in conductivity. Charge conservation demands continuity of the current density component that is normal to the interface  $j_{\perp}$  and the static Maxwell equation forces the parallel component of the electric field  $E_{\parallel} = j_{\parallel}/\sigma$  to be continuous :

$$\begin{aligned} j_{\perp} &= j'_{\perp} \\ j_{\parallel}/\sigma &= j'_{\parallel}/(\sigma + \Delta\sigma) \end{aligned} \tag{3.12}$$

The quantities within the perturbed layer are denoted by primed symbols in these equations. As the normal component of the current density is continuous, the normal component of the electric field experiences a jump  $E'_\perp = \sigma/\sigma' E_\perp$  which is caused by surface charge on the interfaces. These charge layers produce an electric field that is perpendicular to the interface and that causes by Ohm's law a deflection of the current. Using the surface normal vector  $\mathbf{n}$ , the continuity conditions may be combined into a single vector equation for the change of the current density  $\Delta\mathbf{j} = \mathbf{j}' - \mathbf{j}$

$$\Delta\mathbf{j} = \frac{\Delta\sigma}{\sigma}\mathbf{n} \times (\mathbf{j} \times \mathbf{n}) \quad (3.13)$$

If the current variation is small the dominant effect of the conductivity perturbation is to induce a change in the current direction. Assuming an incident current flowing along the x-axis  $\mathbf{j} = j\mathbf{e}_x$  and a normal vector in the x-y plane  $\mathbf{n} = \cos\theta\mathbf{e}_x + \sin\theta\mathbf{e}_y$  the deflection angle of the current density  $\alpha \approx \Delta j_y/j$  is approximately given by

$$\alpha \approx -\frac{1}{2}\frac{\Delta\sigma}{\sigma}\sin 2\theta \quad (3.14)$$

Depending on the direction of the normal vector, the defect layer has a different efficiency for deflecting the current density. The direction of a current that impinges upon the layer under normal incidence or parallel to it will not be altered. The defect is most efficient for  $\theta = \pm 45^\circ$ .

The same kind of symmetry can be directly visualized when a cylindrical defect in the film is considered. A small localized change in the conductivity leads to a pile up of charge in front of the obstacle and a depletion behind it. Assume the homogenous current  $\mathbf{j}_0 = j_0\mathbf{e}_x$  impinging on a cylindrical shaped defect of radius  $R$ , where the conductivity is reduced from its bulk value  $\sigma$  to  $\sigma + \Delta\sigma$ . The potential produced by the defect is that of a charge dipole, which is aligned along the axis of incident current flow  $\mathbf{j}_0 = \sigma\mathbf{E}_0$ . The electric field of this dipole induces by Ohms' law a small deflection  $\alpha \approx j_y/j_0$  of the current density. The angle can be expanded to first order in  $\Delta\sigma/\sigma$  as

$$\alpha = \begin{cases} \frac{1}{2}\frac{R^2\Delta\sigma}{\sigma}\frac{\sin 2\theta}{r^2} & \text{for } r > R \\ 0 & \text{for } r \leq R \end{cases} \quad (3.15)$$

(See section 3.4.1 for the exact result.) This distribution is depicted in figure 3.3.1. As the cylindrical surface combines all possible directions of the surface normal vector  $\mathbf{n}$  one can interpret the observed symmetry in the current flow as showing the response to plane like defects of different orientation.

In order to develop a formalism that is able to treat the general case of an arbitrarily varying conductivity one can proceed along the same physical picture that has been followed in the example cases. A change in the conductivity induces

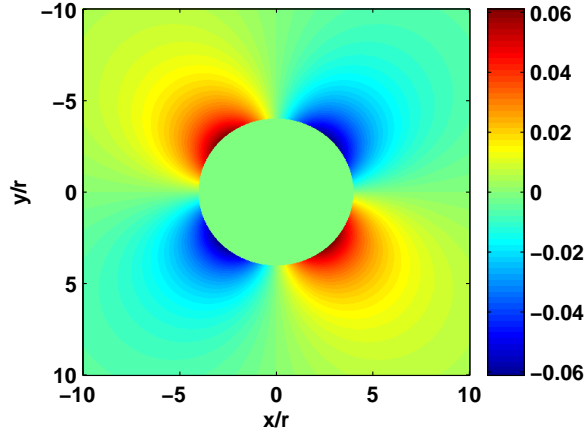


Figure 3.4: Angle deviation of the current density  $\beta$  in the flow around a cylindrical defect. The current impinges on the hole from the left. The length is measured relative to the defect radius  $R$ , and the angle  $\beta$  in arbitrary units.

a charge density  $\rho$  which can be computed from the Maxwell equation  $\nabla \cdot \mathbf{E} = \rho/\epsilon_0$  and Ohm's law

$$\rho = -\epsilon_0 \frac{\nabla \sigma}{\sigma^2} \cdot \mathbf{j} \approx -\epsilon_0 \frac{\nabla \sigma}{\sigma^2} \cdot \mathbf{j}_0 \quad (3.16)$$

In the approximation, the exact current density  $\mathbf{j}$  is replaced by the homogenous part  $\mathbf{j}_0$  which is the current density in the absence of defects. This perturbative treatment is well justified for the measurements of this thesis, as the fluctuations in the current density are extremely small. Using this charge density, the electric potential  $\phi$  due to the perturbation may be computed from the Poisson equation

$$-\nabla^2 \phi = -\frac{\nabla \sigma}{\sigma^2} \cdot \mathbf{j}_0 \quad (3.17)$$

so that the angle deflections  $\alpha_y = j_y/j_0$  and  $\alpha_z = j_z/j_0$  are given by

$$\alpha_{y/z} = -\nabla \phi / E_0 \quad (3.18)$$

Using this approach the effect of surface roughness and bulk defects will now be analyzed.

### 3.3.2 Surface Defects

The conductivity model that has been introduced in the last section also covers the effect of surface corrugations. The boundary surface is nothing but a sharp jump in conductivity and is therefore included by the model. However, the current density may be found more easily for this case by directly considering the boundary conditions on the electric potential. It is assumed that the dominating part of the electric field is the homogenous component along the wire direction  $E_0 = j_0/\sigma$ . The total electric field can be decomposed into the homogenous part and the fluctuating part that is described by the electric potential  $\phi$

$$\mathbf{E} = \frac{j_0}{\sigma} \mathbf{e}_x - \nabla \phi \quad (3.19)$$

The normal component of the current density is continuous across the boundary surface. As there is no current flow on the outside the normal component also has to vanish on the inside of the boundary. By Ohm's law the current density is proportional to the electric field. Therefore, also the normal component of the electric field has to vanish on the boundary

$$\mathbf{n} \cdot \mathbf{E} = 0 \quad (3.20)$$

The surface normal  $\mathbf{n}$  itself is not directly accessible by the standard methods of surface characterization, like interferometry or scanning probe techniques. In these cases the surface topography of the top and bottom surface  $h^{t/b}(\mathbf{x})$  can be used for the calculation of the normal vector. For small variation amplitudes, the normal is given by

$$\mathbf{n} \approx \mathbf{e}_z - \nabla h \quad (3.21)$$

The leading order effect on the electric field and therefore on the current density is contained in the changing surface normal. The actual variations in the surface position are small and its influence will be neglected compared to the effect of the changing normal vector. It will therefore be assumed that the boundary surfaces are sill positioned at  $z = \pm d/2$ .

The boundary condition on the electric field can now be translated to the electric potential  $\phi$

$$\frac{\partial \phi}{\partial z}(z = \pm d/2) = -\frac{\partial h^{t/b}}{\partial x} E_0 + \nabla h^{t/b} \cdot \nabla \phi \approx -\frac{\partial h^{t/b}}{\partial x} E_0 \quad (3.22)$$

the term that has been skipped in the last approximation contains a product of two small amplitudes and is therefore neglected.

Inside the bulk of the wire where no perturbations are assumed, the potential has to fulfill the Laplace equation

$$-\nabla^2\phi = 0 \quad (3.23)$$

In a similar way as for the calculations of the magnetic field in the previous section, the problem is greatly simplified by using a decomposition of the potential into plain Fourier modes

$$\phi(\mathbf{x}, z) = \sum_{\mathbf{k}} E_{\mathbf{k}} f_{\mathbf{k}}(z) e^{i\mathbf{k}\cdot\mathbf{x}} \quad (3.24)$$

In order for this Ansatz to fulfill the Laplace equation, the transverse mode function  $f_{\mathbf{k}}(z)$  has to be a linear combination of exponentials

$$f_{\mathbf{k}}(z) = a_+ e^{kz} + a_- e^{-kz} \quad (3.25)$$

The coefficients  $a_{\pm}$  allow to accommodate for different boundary conditions. Assuming that the corrugations of the top and bottom surface are represented by the Fourier decomposition

$$h^{t/b}(\mathbf{x}) = \sum_{\mathbf{k}} h_{\mathbf{k}}^{t/b} e^{i\mathbf{k}\cdot\mathbf{x}} \quad (3.26)$$

the boundary condition of equation 3.22 translates into an equation for the Fourier coefficients

$$E_{\mathbf{k}} \frac{\partial f_{\mathbf{k}}}{\partial z}(z = \pm d/2) = -E_0 i k_x h_{\mathbf{k}}^{t/b}. \quad (3.27)$$

Assuming two transverse mode functions  $f_{\mathbf{k}}^{t/b}(z)$  that fulfill

$$\begin{aligned} \frac{\partial f_{\mathbf{k}}^t}{\partial z}(z = d/2) &= 1 & \frac{\partial f_{\mathbf{k}}^t}{\partial z}(z = -d/2) &= 0 \\ \frac{\partial f_{\mathbf{k}}^b}{\partial z}(z = d/2) &= 0 & \frac{\partial f_{\mathbf{k}}^b}{\partial z}(z = -d/2) &= -1 \end{aligned} \quad (3.28)$$

the Fourier coefficients for the potential and the corresponding transverse mode functions can be written as

$$\begin{aligned} E_{\mathbf{k}} &= -ik_x d E_0 \\ f_{\mathbf{k}}(z) &= \frac{h_{\mathbf{k}}^t}{d} f_{\mathbf{k}}^t(z) + \frac{h_{\mathbf{k}}^b}{d} f_{\mathbf{k}}^b(z) \end{aligned} \quad (3.29)$$

By construction, this combination fulfills the boundary conditions on both, top and bottom surface.

Alternatively it is possible to write the height corrugations in terms of thickness and center modulations of the wire which correspond to symmetric and antisymmetric combinations of the top and bottom layer roughness

$$\begin{aligned} \frac{h_{\mathbf{k}}^s}{d} &= \frac{1}{2} \left( \frac{h_{\mathbf{k}}^t}{d} + \frac{h_{\mathbf{k}}^b}{d} \right) \\ \frac{h_{\mathbf{k}}^a}{d} &= \frac{1}{2} \left( \frac{h_{\mathbf{k}}^t}{d} - \frac{h_{\mathbf{k}}^b}{d} \right) \end{aligned} \quad (3.30)$$

Thickness variations  $\Delta d$  of the wire are related to the asymmetric amplitude by  $\Delta d = 2h^a$ . The four different fundamental cases of top surface corrugations only ( $h^b = 0$ ), bottom surface corrugations only ( $h^t = 0$ ), symmetric modulations of both top and bottom layer ( $h^t = h^b$ ) and antisymmetric thickness modulations ( $h^t = -h^b$ ) are summarized for comparison in figure(3.5).

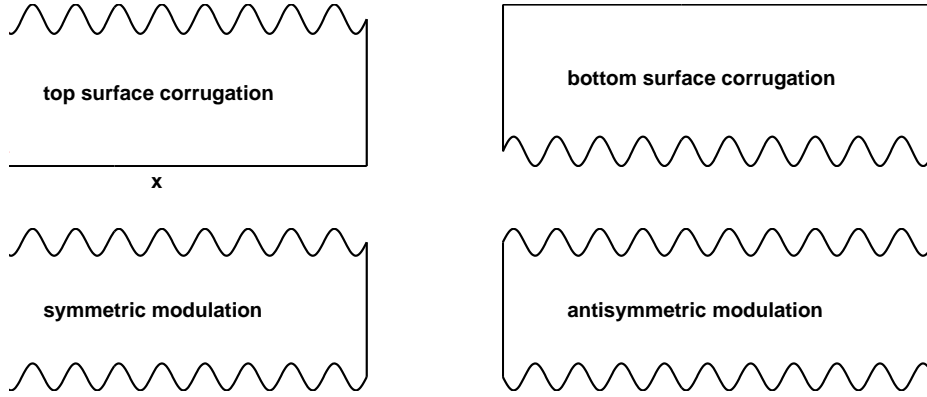


Figure 3.5: *The different basic types of surface modulation.*(**top left**) Top surface corrugations. (**top left**) Bottom surface corrugations.(**bottom left**) Wire center modulations. (**bottom right**) Thickness modulation

Using the description in terms of thickness and center modulations, the Fourier coefficients and the mode functions of the potential become

$$\begin{aligned} E_{\mathbf{k}} &= -ik_x d E_0 \\ f_{\mathbf{k}}(z) &= h_{\mathbf{k}}^s f_{\mathbf{k}}^s(z) h_{\mathbf{k}}^a f_{\mathbf{k}}^a(z) \end{aligned} \quad (3.31)$$

where

$$\begin{aligned} f_{\mathbf{k}}^s(z) &= f^t_{\mathbf{k}}(z) + f^b_{\mathbf{k}}(z) \\ f_{\mathbf{k}}^a(z) &= f^t_{\mathbf{k}}(z) - f^b_{\mathbf{k}}(z) \end{aligned} \quad (3.32)$$

In principle both, the separate description of the surfaces or of the wire thickness and center position are equivalent pictures. The latter however is more convenient as it decomposes the modulations in terms of quantities that are immediately connected to the average response of the current density.

The symmetric and antisymmetric mode functions are given explicitly by

$$\begin{aligned} f_{\mathbf{k}}^s(z) &= \frac{d}{\kappa} \tanh \frac{\kappa}{2} \frac{\sinh \kappa \frac{z}{d}}{\sinh \frac{\kappa}{2}} \\ f_{\mathbf{k}}^a(z) &= \frac{d}{\kappa} \coth \frac{\kappa}{2} \frac{\cosh \kappa \frac{z}{d}}{\cosh \frac{\kappa}{2}} \end{aligned} \quad (3.33)$$

where  $\kappa = kd$ . The spatial dependence of the various mode functions is compared in figure (3.6) for different values of  $k$ . Two qualitatively different regimes can

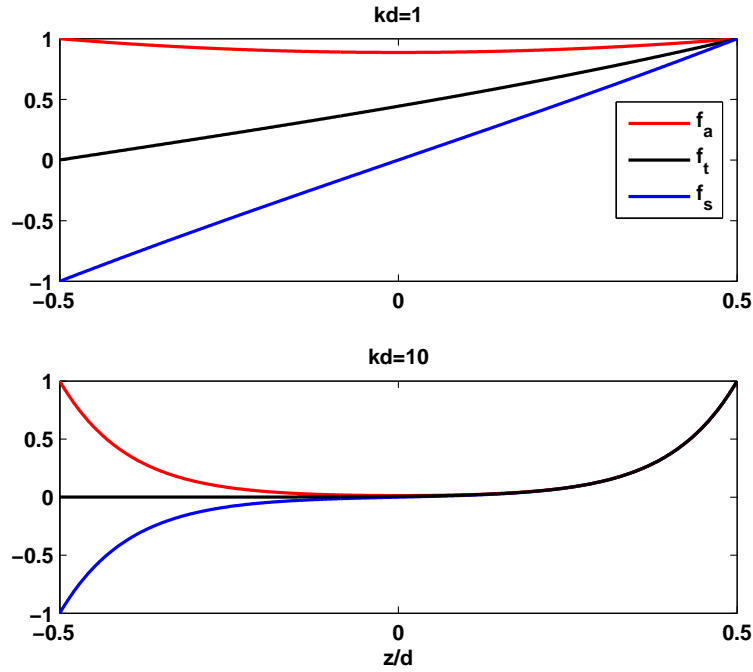


Figure 3.6: *Transverse mode functions*  $f_k(z)$ . The symmetric, antisymmetric and top mode function are shown for different values of  $kd$ . (**top panel**): Small  $kd$  regime. Only the symmetric contribution of the mode functions makes a significant contribution to the average current. (**bottom panel**): Large  $kd$  regime. The modes behave like surface waves where the current is localized close to the boundaries.

be discerned according to the degree of localization of the functions. For small wavevectors  $kd \ll 1$ , the current extends over the full thickness of the wire. In the opposite limit of  $kd \gg 1$  the current is localized to the source of the perturbation i.e. at the surfaces and drops off exponentially into the bulk. In this regime the modes behave like typical surface waves. For the experiments that have been performed in

this work this regime cannot be resolved. As the thickness of the wires is  $\leq 2\mu m$  the optical resolution of approximately  $3\mu m$  is not good enough to resolve these length scales.

It is a simple matter of taking the gradient of the potential, to obtain the electric field and therefore also the current fluctuations

$$\Delta \mathbf{j} = -\sigma \nabla \phi = j_0 \sum_{\mathbf{k}} ik_x d \left( \frac{\partial f_{\mathbf{k}}}{\partial z}(z) \mathbf{e}_z + i\mathbf{k} f_{\mathbf{k}}(z) \right) e^{i\mathbf{k}\cdot\mathbf{x}} \quad (3.34)$$

. The explicit expressions in terms of symmetric and asymmetric modulations are given by

$$\Delta \mathbf{j}_{\mathbf{k}}^s = j_0 ik_x d \frac{h_{\mathbf{k}}^s}{d} \left[ \frac{\cosh \kappa \frac{z}{d}}{\cosh \frac{\kappa}{2}} \mathbf{e}_z + i \frac{\mathbf{k}d}{\kappa} \tanh \frac{\kappa}{2} \frac{\sinh \kappa \frac{z}{d}}{\sinh \frac{\kappa}{2}} \right] \quad (3.35)$$

$$\Delta \mathbf{j}_{\mathbf{k}}^a = j_0 ik_x d \frac{h_{\mathbf{k}}^a}{d} \left[ \frac{\sinh \kappa \frac{z}{d}}{\sinh \frac{\kappa}{2}} \mathbf{e}_z + i \frac{\mathbf{k}d}{\kappa} \coth \frac{\kappa}{2} \frac{\cosh \kappa \frac{z}{d}}{\cosh \frac{\kappa}{2}} \right] \quad (3.36)$$

These expressions now characterize the current flow inside the wire in terms of measurable surface variations. The magnetic field that is produced by them can be calculated using equation 3.7. Substituting the current density into this equation results in the magnetic field angle deviations  $B_x/B_0$

$$\beta(\mathbf{x}, z) = - \sum_{\mathbf{k}} e^{i\mathbf{k}\cdot\mathbf{x}} \frac{k_x k_y}{k^2} \frac{2h_{\mathbf{k}}^s}{d} w^s(\kappa) e^{-k(z-d/2)} \quad (3.37)$$

$$\beta(\mathbf{x}, z) = - \sum_{\mathbf{k}} e^{i\mathbf{k}\cdot\mathbf{x}} \frac{k_x k_y}{k^2} \frac{2h_{\mathbf{k}}^a}{d} w^a(\kappa) e^{-k(z-d/2)} \quad (3.38)$$

where the weight factors are given by  $w^s(\kappa)$  and  $w^a(\kappa)$  are given by

$$\begin{aligned} w_s &= \frac{1}{d} \int_{-\frac{d}{2}}^{\frac{d}{2}} dz' e^{-k(d/2-z)} \frac{\kappa}{2} \left( \frac{\cosh \kappa \frac{z'}{d}}{\cosh \frac{\kappa}{2}} + \tanh \kappa/2 \frac{\sinh \kappa \frac{z'}{d}}{\sinh \frac{\kappa}{2}} \right) \\ &= \frac{1}{2} (1 - e^{-\kappa}) \end{aligned} \quad (3.39)$$

and

$$\begin{aligned} w_a &= \frac{1}{d} \int_{-\frac{d}{2}}^{\frac{d}{2}} dz' e^{-k(d/2-z)} \frac{\kappa}{2} \left( \frac{\sinh \kappa \frac{z'}{d}}{\sinh \frac{\kappa}{2}} + \coth \kappa/2 \frac{\cosh \kappa \frac{z'}{d}}{\cosh \frac{\kappa}{2}} \right) \\ &= \frac{1}{2} (1 + e^{-\kappa}) \end{aligned} \quad (3.40)$$

### 3.3.3 Bulk Defects

In the same way as corrugations in the external boundaries can induce deviations in the current path, internal boundaries between different crystalline regions can act in a similar way. Depending on how the single grains group together, the electrical contact between them may change. On a larger scale, the accumulated effect of many grain defects may be described by the effective conductivity  $\sigma(\mathbf{x})$ .

It will be assumed that all the defects reach down straight from the top to the bottom surface. The situation is depicted schematically in figure (3.7). As only

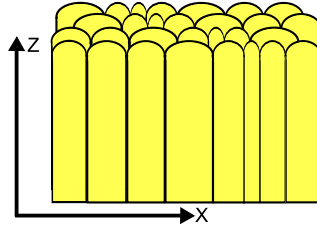


Figure 3.7: Symmetry of the grain structure in thin film wires.

bulk effect defects are considered now, the boundaries are assumed to be completely flat which forces the  $z$ -component of the current density to have a zero at the surface. In contrast to the case of boundary corrugations, the source for the fluctuations sits now inside the bulk material and may be incorporated explicitly by a source term in the poisson equation 3.17.

As in the case of boundary corrugations the situation may be analyzed most easily by a decomposition of the electrical potential in terms of plain Fourier modes

$$\phi(\mathbf{x}, z) = \sum_{\mathbf{k}} E_{\mathbf{k}} f_{\mathbf{k}}(z) e^{i\mathbf{k}\cdot\mathbf{x}} \quad (3.41)$$

. In the present case however, a source term is added to the Laplace equation in the bulk

$$\nabla^2 \phi = \frac{j_0}{\sigma_0^2} \frac{\partial \sigma}{\partial x} \quad (3.42)$$

In general, any conductivity may be decomposed into plane Fourier modes on each vertical section

$$\sigma(\mathbf{x}, z) = \int dz_0 \sum_{\mathbf{k}} \sigma_{\mathbf{k}}(z_0) \delta(z - z_0) e^{i\mathbf{k}\cdot\mathbf{x}} \quad (3.43)$$

Once the Poisson equation is solved for a single mode in this decomposition, the general solution may be composed by superposition. Let's consider therefore the equation for the generic source mode

$$\nabla g_{\mathbf{k},z_0} = \frac{j_0}{\sigma_0^2} i k_x \sigma_{\mathbf{k}} \delta(z - z_0) e^{i\mathbf{k}\cdot\mathbf{x}} \quad (3.44)$$

the particular solution to this equation is given by

$$g_{\mathbf{k},z_0}^i(\mathbf{x}, z) = -\frac{j_0}{\sigma_0^2} i k_x \sigma_{\mathbf{k}} \frac{e^{-k|z-z_0|}}{2k} e^{i\mathbf{k}\cdot\mathbf{x}} \quad (3.45)$$

in order to fulfill the boundary conditions the normal derivative has to vanish on the top and bottom surface. The boundary terms of the particular solution

$$\frac{\partial g_{\mathbf{k},z_0}^i}{\partial z}(z = \pm d/2) = \mp k g_{\mathbf{k},z_0}^i(z = \pm d/2) \quad (3.46)$$

may be compensated by an appropriate homogenous solution. The total solution, fulfilling the boundary conditions is therefore given by

$$g_{\mathbf{k},z_0}(\mathbf{x}, z) = -i \frac{j_0}{\sigma_0^2} \frac{k_x}{2k} \sigma_{\mathbf{k}} \times \quad (3.47)$$

$$\left[ e^{-k|z-z_0|} + e^{-kd/2} \left( \sinh kz_0 \frac{\sinh kz}{\cosh kd/2} + \cosh kz_0 \frac{\cosh kz}{\sinh kd/2} \right) \right] e^{i\mathbf{k}\cdot\mathbf{x}}$$

The potential for an arbitrary conductivity fluctuation is composed of these modes by

$$\phi(\mathbf{x}, z) = \sum_{\mathbf{k}} \int dz_0 g_{\mathbf{k},z_0}(\mathbf{x}, z) e^{i\mathbf{k}\cdot\mathbf{x}} \quad (3.48)$$

If the conductivity does not change along the vertical direction, the integral over the transverse direction may be carried out separately. The formula simplifies then to

$$\phi(\mathbf{x}, z) = -i \frac{j_0}{\sigma_0^2} \sum_{\mathbf{k}} e^{i\mathbf{k}\cdot\mathbf{x}} \frac{k_x}{k^2} \sigma_{\mathbf{k}} \quad (3.49)$$

which results in the current deviation

$$\Delta j_y = -j_0 \sum_{\mathbf{k}} e^{i\mathbf{k}\cdot\mathbf{x}} \frac{k_y k_x}{k^2} \frac{\sigma_{\mathbf{k}}}{\sigma_0} \quad (3.50)$$

from this expression the magnetic field may be evaluated according to equation 3.7 as

$$B_x = \frac{\mu_0 d j_0}{2} \sum_{\mathbf{k}} e^{i\mathbf{k}\cdot\mathbf{x}} \frac{k_x k_y}{k^2} \frac{\sigma_{\mathbf{k}}}{\sigma_0} w_k^b \quad (3.51)$$

where the mode weighting factor is given by

$$w_k^b = \frac{1}{d} \int_{-\frac{d}{2}}^{\frac{d}{2}} e^{-k(d/2-z)} dz = \frac{1 - e^{-kd}}{kd} \quad (3.52)$$

### 3.3.4 Comparison of Bulk and Surface Models

When comparing the formulas for the magnetic field that is produced by the different defect types, it becomes apparent that all the models may be written in terms of an effective conductivity

$$B_x(\mathbf{x}, z) = \frac{\mu_0 d j_0}{2} \sum_{\mathbf{k}} e^{i\mathbf{k}\cdot\mathbf{x}} \frac{k_x k_y}{k^2} \frac{\sigma_{\mathbf{k}}^{\text{eff}}}{\sigma_0} w_{\mathbf{k}} \quad (3.53)$$

Depending on the explicit model, the relative fluctuations of the conductivity are either related to thickness fluctuations, center fluctuations or directly to real conductivity variations. The only difference between the defect scenarios is the different spectral weighting factor for each model.

A feature that all models have in common is the peculiar symmetry introduced by the  $k_x k_y / k^2$  factor. If the polar coordinates  $(k_x, k_y) = k(\cos \theta, \sin \theta)$  are introduced in  $\mathbf{k}$  space this factor equals the already familiar  $1/2 \sin 2\theta$  dependence. For an isotropic effective conductivity this factor leads to a power spectrum which is concentrated around the  $\pm 45^\circ$  directions.

For a comparison of the model dependent properties the different parameters are summarized in tabular 3.1. The graphs of the spectral weighting factors  $w_{\mathbf{k}}$  are

defect type	$\sigma_{\mathbf{k}}^{\text{eff}}/\sigma_0$	$w_{\mathbf{k}}$
thickness	$2h_{\mathbf{k}}^a/d$	$(1 + e^{-kd})/2$
bulk	$\sigma_{\mathbf{k}}/\sigma_0$	$(1 - e^{-kd})/kd$
center	$2h_{\mathbf{k}}^s/d$	$(1 - e^{-kd})/2$

Table 3.1: *Spectral weighting factors of different defect types.* ( $h^a$  and  $h^s$  are related to the top and bottom surface corrugations  $h^t, h^b$  by  $h^a = 1/2(h^t - h^b)$  and  $h^s = 1/2(h^t + h^b)$ .)

plotted in figure (3.8). Experimentally most relevant is the limit of  $kd \rightarrow 0$ . In this regime bulk and thickness modulations converge to a single model equation if the substitution  $\sigma_{\mathbf{k}}^{\text{eff}}/\sigma_0 = \sigma_{\mathbf{k}}/\sigma_0 = 2h_{\mathbf{k}}^a/d$  is made. The influence of modulations in the wire center position however are strongly suppressed.

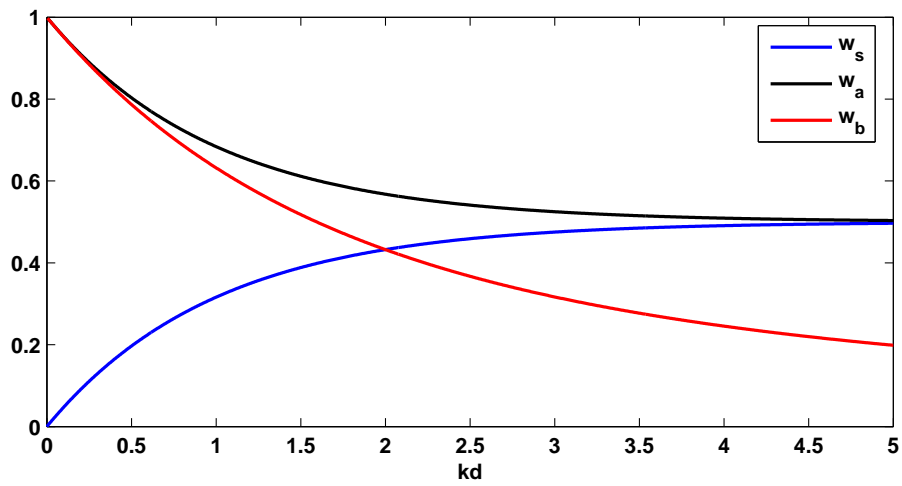


Figure 3.8: Weighting factors of the various current modes  $w_a$ : thickness modulation,  $w_s$ : wire center modulation,  $w_b$ : bulk conductivity modulation.

## 3.4 Appendix

### 3.4.1 Current-flow Around a Cylindrical Defect

A cylindrical defect of radius  $R$ , extending over the whole thickness of a thin film, in which the conductivity is reduced from its bulk value  $\sigma$  to  $\sigma + \Delta\sigma$ , causes a deflection of the current density  $j_0\mathbf{e}_x$  impinging on the defect. The current density on the outside is given by

$$j_x = j_0 \left( 1 + \frac{\Delta\sigma}{2\sigma + \Delta\sigma} \frac{\cos 2\theta}{(r/R)^2} \right) \quad (3.54)$$

$$j_y = j_0 \frac{\Delta\sigma}{2\sigma + \Delta\sigma} \frac{\sin 2\theta}{(r/R)^2} \quad (3.55)$$

and on the inside by

$$j_x = j_0 \frac{2\sigma + 2\Delta\sigma}{2\sigma + \Delta\sigma} \mathbf{e}_x \quad (3.56)$$

$$j_y = 0 \quad (3.57)$$

It is obvious that all components fulfill the two dimensional Laplace equation  $\nabla^2\mathbf{j} = 0$  separately. They also satisfy the charge conservation  $\nabla \cdot \mathbf{j} = 0$  and the static Maxwell equation  $\nabla \times \mathbf{E} = 0$  in each domain of constant conductivity. In order to show that the solution is also valid on the interface, the normal component of the current density and the parallel component of the electric field have to be continuous across the discontinuity. These conditions will be checked now.

The normal component of the current density is given on the outside by

$$j_n = j_0 \cos \theta \left( 1 + \frac{\Delta\sigma}{2\sigma + \Delta\sigma} \frac{1}{(r/R)^2} \right) \quad (3.58)$$

and on the inside by

$$j_n = j_0 \cos \theta \frac{2\sigma + 2\Delta\sigma}{2\sigma + \Delta\sigma}. \quad (3.59)$$

At the interface, where  $r = R$  the two expression coincide and the boundary condition is satisfied.

The parallel component of the electric field is given on the outside by

$$E_{\parallel} = -E_0 \sin \theta \left( 1 - \frac{\Delta\sigma}{2\sigma + \Delta\sigma} \frac{1}{(r/R)^2} \right) \quad (3.60)$$

and on the inside by

$$E_{\parallel} = -E_0 \sin \theta \frac{2\sigma + 2\Delta\sigma}{2\sigma + \Delta\sigma} \frac{\sigma}{\sigma + \Delta\sigma} \quad (3.61)$$

Also here both expressions coincide for  $r = R$ . The solution given above is therefore valid everywhere.

# Bibliography

- [1] Roth,B.J Sepulveda,N.G. Wikswo,J.P. Using a magnetometer to image a two-dimensional current distribution. *J. Appl. Phys.* **65**, 361 (1989)
- [2] Wang,D.-W. Lukin,M.D. Demler,E. Disordered Bose-Einstein Condensates in Quasi-One-Dimensional Magnetic Microtraps. *Phys. Rev. Lett.* **92**, 076802 (2004)
- [3] Schumm,T. Atom chips in the reals world: the effects of wire corrugation. *Eur. Phys. J. D*, **32**, 171 (2005)
- [4] Japha,Y. et al. *submitted to PRL*

---

# 4 BASIC MEASUREMENTS ON ULTRACOLD ATOMS

---

## 4.1 Introduction

An ideal gas consists by definition of atoms that do not interact with each other. However, despite the absence of any physical interaction, the total quantum mechanical state describing the gas must show a definite symmetry under the interchange of any two particles in the system. It has to be either symmetric for Bosons, or antisymmetric for Fermions. The symmetry makes it possible for many Bosons to occupy a single energetically favorable quantum state, whereas for Fermions this situation is forbidden by the Pauli principle. For a gas at room temperature a distinction between the two kinds of particles makes no large difference. The number of states that are energetically allowed by the Boltzmann distribution is much larger than the number of atoms competing for their occupation. If however both numbers become close to equal Bosons start to condense in the same ground state. This phase transition has already been predicted in 1925 by A. Einstein in analogy to a novel treatment of the black body radiation introduced by S. Bose [1, 2]. This mechanism is a key ingredient in the superfluidity of  $^4\text{He}$  [3] and superconductivity [4]. However, as the phase transition is of second order, there is no separation of the condensed from the uncondensed phase in homogenous solid state systems.

For dilute alkali gases, trapped by a harmonic potential, the situation is different. As shown in the pioneering work of [5, 6] the two key techniques of laser and evaporative cooling make it possible to cool down a small number of bosonic Rb or Na atoms (usually  $10^4 - 10^6$ ) to temperatures in the order of 100nK. As the gas is trapped by

a harmonic potential, the different susceptibility of condensate and thermal atoms to potential inhomogeneities results in qualitatively different density distributions that allow a clear experimental distinction of the two phases.

Figure 4.1 shows this change in the density across the phase transition as observed in the routine preparation of cold  $^{87}\text{Rb}$  atoms in the present work. The pictures show a projection of the three dimensional density distribution onto the observation plain. The thermal cloud smoothly covers a broad region of the potential, where as the condensate shows up as a sharp peak growing in the center of the cloud. The

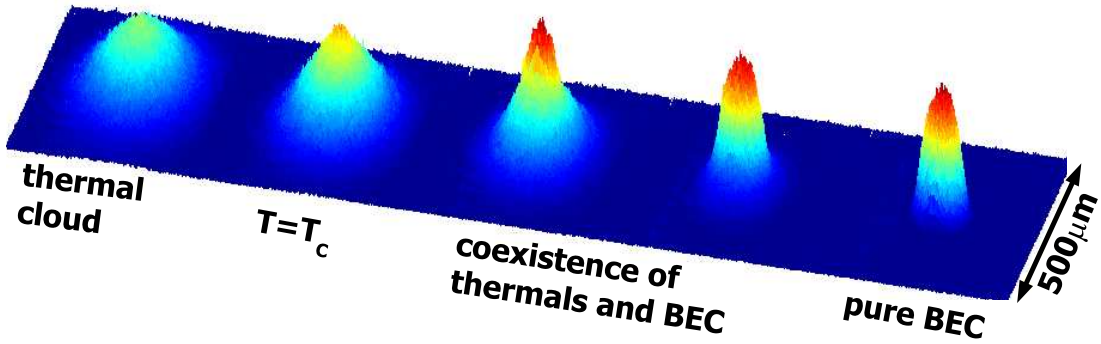


Figure 4.1: *Bose-Einstein-Condensation of  $^{87}\text{Rb}$  atoms.* The series of pictures show the atomic density distribution projected onto the plain of observation after  $t = 7\text{ms}$  of free expansion from a standard harmonic trap used in the experiments (trapping frequencies  $\omega_x = 21 \times 2\pi\text{Hz}$ ,  $\omega_y = \omega_z = 840 \times 2\pi\text{Hz}$ ). The resulting column density is encoded in the height level and the color map of the pictures. From left to right the temperature is reduced from above to below the critical temperature  $T_c \approx 660\text{nK}$ .

temperature regime where this transition takes place may be obtained by estimating the number of thermally accessible states from the product of the number of states below the energy  $E$  [7]

$$G(E) = \frac{E^3}{6(\hbar\bar{\omega})^3} \quad (4.1)$$

(where  $\hbar\bar{\omega} = \hbar(\omega_x\omega_y\omega_z)^{\frac{1}{3}}$ ) and the thermally allowed energy range of approximately  $k_B T$ . Equating this product to the number of particles  $N$  results in the degeneracy condition

$$k_B T_c \approx \hbar\bar{\omega} N^{\frac{1}{3}} \quad (4.2)$$

where factors of order one have been neglected. (This approximation is close the exact result of  $k_B T_c = \hbar\bar{\omega} N^{\frac{1}{3}} / \zeta(3)^{1/3}$ .) For the trapping potentials and densities employed in the experimental work to this thesis the critical temperature has been

in the range of  $T_c \approx (50 - 700)\text{nK}$ .

The different response behavior of thermal or condensate atoms to spatial changes in the potential marks the two regimes of operation in which ultracold  $^{87}\text{Rb}$  atoms can operate as a potential sensor. Both, the experimental handling and accessibility of parameters, as well as the theoretical description is largely simplified when using either completely thermal or completely condensed clouds.

For temperatures well above the critical temperature the density distribution of a gas, confined by the potential  $V(\mathbf{x})$ , is simply given by Boltzmann statistics

$$n(\mathbf{x}) = \exp \left[ -\frac{V(\mathbf{x}) - \mu}{k_B T} \right] \quad (4.3)$$

In the other limit, all particles have condensed to the same single particle wave function  $\psi$  which is described by the Gross-Pitaevskii equation

$$\mu\psi = \left( -\frac{\hbar^2 \nabla^2}{2m} + V(\mathbf{x}) + g|\psi(\mathbf{x})|^2 \right) \psi \quad (4.4)$$

The non-linear term that is added to a single particle Schrödinger equation accounts for repulsive interaction in the mean field approximation. At the high densities achieved in the condensate this contribution to the energy cannot be neglected. The interaction strength  $g$  is related to the s-wave scattering length  $a$  by  $g = \frac{4\pi\hbar^2 a}{m}$ . For  $^{87}\text{Rb}$  in the  $F = 2$   $m_F = 2$  ground state the former has been measured to be  $a = 5.6\text{nm}$ . The wavefunction is normalized such that the absolute square yields the particle density  $n(\mathbf{x}) = |\psi(\mathbf{x})|^2$ .

In the remainder of this chapter the fundamental experimental techniques and their theoretical background to probe and characterize a cloud of ultracold atoms in either regime will be presented.

## 4.2 Detection

All information on an atomic cloud is finally retrieved from a measurement of the particle density distribution. The detection procedure is therefore an integral part of any experiment. In the present work the detection scheme has been based on resonant absorption imaging.

The underlying idea of this technique is that an atom that is resonantly excited by a weak laser beam decays back into its ground state by emitting the photon into a random direction. Looking at the laser beam after it has passed through the atomic

cloud this fluorescence light is missing in the beam i.e. the atoms cast a shadow. Figure 5.1 shows how this principle is implemented in an imaging system. As long as

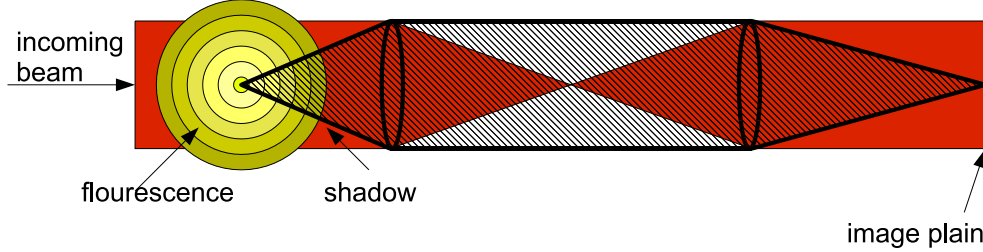


Figure 4.2: Absorption imaging of an atomic cloud.

the shadow covers a solid angle that is much smaller than the full  $4\pi$  into which the fluorescence light is emitted, the two signals can be discerned by its different angle spread. A telescope, that is used for imaging the plain containing the atomic cloud, effectively images the shadow and the laser light only, as long as the accepted solid angle is small compared to  $4\pi$ . In the presented experiments the first lens, having the atoms in its focus, has been a  $f = 100\text{mm}$  lens with a diameter of  $D = 30\text{mm}$ . The captured solid angle is  $\Omega = 5\% 4\pi$  so that even for the smallest resolved objects of approximately  $3\mu\text{m}$  the fluorescence contribution makes only a small effect. The strength of the shadow is linked to the parameters of the atomic transition that is used for imaging. In general the amount of power  $P_{sc}$  scattered by a single atom is quantified by the absorption cross section  $\sigma$

$$P_{sc} = \sigma I \quad (4.5)$$

where  $I$  is the intensity of the exciting light field. If the atomic number density is denoted by  $n(\mathbf{x})$  the intensity of the beam after travelling a small distance  $dy$  through the cloud is attenuated by

$$\Delta I = -\sigma I n(\mathbf{x}) \Delta y \quad (4.6)$$

. As long as the scattering cross section does not depend on the intensity, this equation can be integrated to give Beer Lambert's law

$$I(x, z) = I_0 \exp[-\sigma d(x, z)] \quad (4.7)$$

where  $d(x, z)$  is the projected particle or column density

$$d(x, z) = \int dy' n(x, y', z) \quad (4.8)$$

and  $I_0$  is the intensity of the incident beam. By this fundamental relation the shadow can be related quantitatively to the traversed column density.

In order for the assumption of a constant scattering cross section to hold, the intensity may not exceed a certain limit that is determined by the properties of the atomic transition. In general, for a resonant transition between two levels it has the form

$$\sigma = \sigma_0 \frac{1}{1 + \frac{I}{I_{\text{sat}}}} = \sigma_0 \left( 1 - \frac{I}{I_{\text{sat}}} + \left( \frac{I}{I_{\text{sat}}} \right)^2 - \dots \right) \quad (4.9)$$

where  $I_{\text{sat}}$  is the saturation intensity. In this work the intensity has been kept around  $I = 10\%I_{\text{sat}}$  and the nonlinear terms have been neglected. The parameters  $\sigma_0$  and  $I_{\text{sat}}$  depend on the transition used for imaging. For a  $^{87}\text{Rb}$  cloud prepared in the  $F = 2$  groundstate there are three dipole allowed transitions to the excited states  $F' = 1$ ,  $F' = 2$  or  $F' = 3$ . The level scheme of the  $D_2$  line is shown in figure 4.3. Out of these possibilities, the  $F = 2 \rightarrow F' = 3$  transition has the major advantage

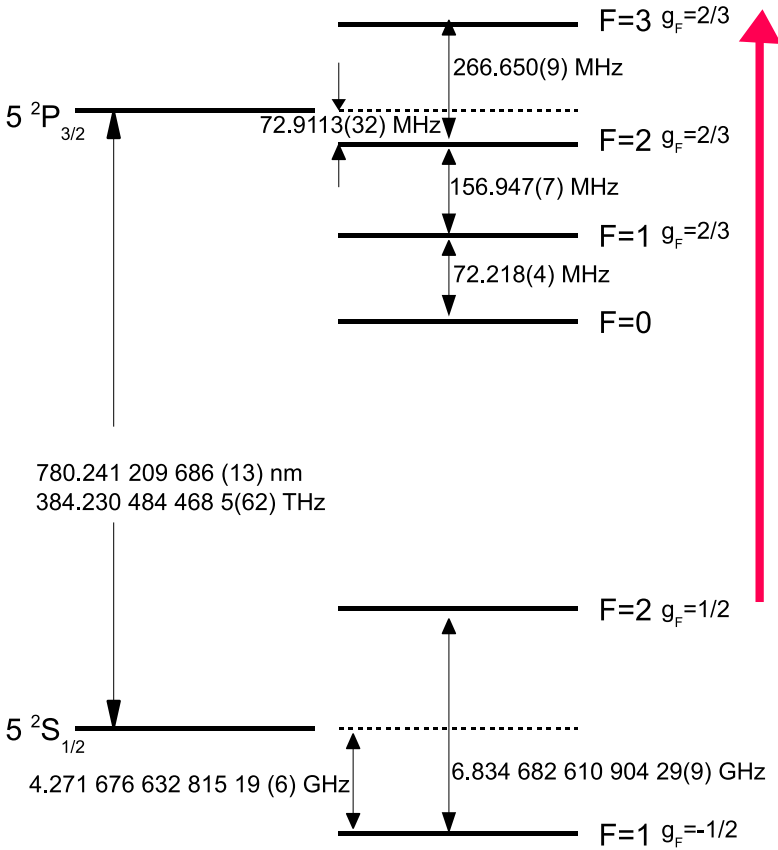


Figure 4.3: Transitions within the  $^{87}\text{Rb}$   $D_2$  line. The values for the excited and ground state are according to [8] and [9]. The Lande factors are taken from [10]

that is closed. An atom in the  $F' = 3$  state can only fall back into the initial  $F' = 2$ .

A single atom can therefore participate in a large number of fluorescence cycles. The largest cross section occurs for circular polarized light where  $I_{\text{sat}} = 1.669 \frac{\text{mW}}{\text{cm}^2}$ , and  $\sigma = 2.90710^{-9} \text{cm}^2$ . However this line cannot be used for imaging close to a metallic surface. Only for linear polarization, the polarization state can be adjusted to be equal, before and after reflection by a mirror surface. For this reason, plane polarized light with  $I_{\text{sat}} = 2.503 \frac{\text{mW}}{\text{cm}^2}$  and  $\sigma = 1.93810^{-9} \text{cm}^2$  has been used. Apart from the limit on the usable intensity also the exposure time cannot be made arbitrarily long. During each fluorescence cycle a recoil momentum is transferred to the atom. On the average this leads to a diffusive motion of the atoms where the rms distance  $r_{\text{rms}}$  after the absorption of  $N$  photons is given by [11]

$$r = \sqrt{\frac{N}{3}} v_{\text{rec}} \Delta t \quad (4.10)$$

The recoil velocity due to a single photon for  $^{87}\text{Rb}$  on the  $D_2$  line is given by  $v_{\text{rec}} = 5.89 \frac{\text{mm}}{\text{s}}$ . For an imaging intensity  $I = 0.1 I_{\text{sat}}$  the number of scattered photons is given by  $N = 0.1 \frac{\Gamma}{2} \Delta t^{\frac{3}{2}}$  which leads to

$$r = \sqrt{0.1} \sqrt{\frac{\Gamma}{6}} v_{\text{rec}} \Delta t \quad (4.11)$$

The imaging duration has been chosen to yield a diffusion radius that is smaller than the optical resolution of approximately  $3 \mu\text{m}$ . For the applied value of  $\Delta t = 50 \mu\text{s}$  the radius is  $r_{\text{rms}} = 1.7 \mu\text{m}$ .

The detection of the imaged shadow has been performed by a CCD camera (Andor DV 435-BV958). With such a detector there are two different sources of noise that imply a limit for the achievable atomic sensitivity. One part is given by the dark noise level that exists independently of whether the detector is illuminated or not. With the camera used in this work this noise is only connected to the readout of the CCD bins. The dark current that would lead to a noise that is proportional to the acquisition time, is negligible as the detector has been cooled down to  $T = -45^\circ\text{C}$ . The measured dark noise level is  $\sigma_D = 3.3 \text{cts}$  on each pixel.

The dominating noise source is due to the photon detection process. In each detection event of a photon an electron is generated on the CCD pixel. This detection is an all or nothing process. With the probability  $e = 0.75$  a photon is converted into an electron. However, it is not possible to generate a non integer number of photo-electrons. This leads to Poissonian noise, where the standard deviation  $\sigma_e$  is proportional to the square root of the mean number of photoelectrons  $N_e$

$$\sigma_e^2 = N_e = e N_{\text{ph}} \quad (4.12)$$

In order to use the full resolution of the following AD converter, the photo-electron signal is scaled by the gain  $G$  to yield the count signal. The noise level for the count

signal is thereby scaled to

$$\sigma_c^2 = G^2 \sigma_e^2 = G^2 N_e = GN_c \quad (4.13)$$

This noise model has been checked by extracting noise and mean value from the difference and mean of two successive pictures showing a nearly constant intensity distribution. The resulting linear dependence of the standard deviation on the mean number of counts is shown in figure 4.4. The validity of the Poissonian noise model

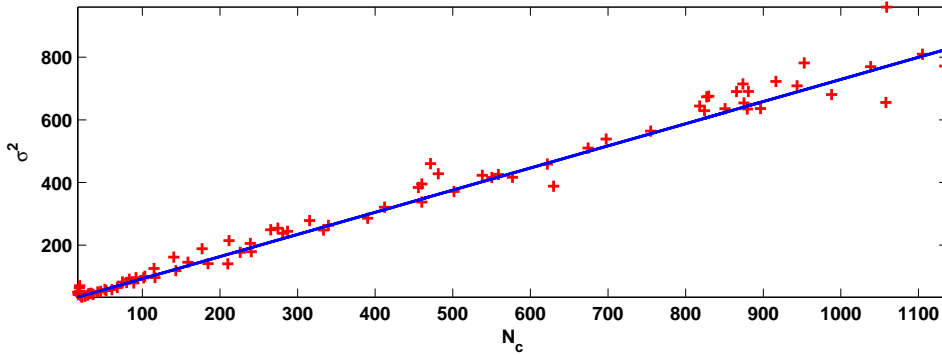


Figure 4.4: *Photon detection shot noise*. Noise and standard deviation extracted from two successive pictures. For each pixel, the difference and mean value between the two pictures have been computed. An estimate of mean value and standard deviation is then extracted by computing a local standard deviation and averaging over many distinct 20 by 10 pixel regions. The resulting noise value is by a factor of  $\sqrt{2}$  larger than that of a single picture. From the slope of the straight line a gain of  $G = 2$  has been extracted.

for the difference of two successive pictures shows that vibrations or fluctuations in the imaging beampath have no significant influence. Otherwise a noise contribution that is proportional to the intensity would appear.

By using the gain  $G = 2$ , the quantum efficiency  $e = 0.75$ , the acquisition time  $\Delta t = 50 \mu s$  and the pixel size in the imaged plain  $\Delta x = 1.70 \cdot 10^{-6} \mu m$ , the number of detector counts can be converted to an intensity.

$$I = N_c \times G / (e(\Delta x)^2 \Delta t) = 0.47 \frac{\text{mW}}{\text{cm}^2 \text{cts}} N_c \quad (4.14)$$

When acquiring two successive pictures in a row, one with and one without atoms, Beer-Lambert's law (4.7) can be used to extract the column density from the

ratio of the two pictures

$$d = -\log [I/I_0] / \sigma = -\log [N/N_0] / \sigma \quad (4.15)$$

where  $N$  and  $N_0$  denote the counts per pixel acquired by the camera. In order to estimate the influence of shot noise on the thereby calculated column density a gaussian error propagation may be used

$$\begin{aligned} \Delta d &= \frac{1}{\sigma} \left( \frac{\Delta N_0^2}{N_0^2} + \frac{\Delta N^2}{N^2} \right)^{\frac{1}{2}} \\ &= \frac{1}{\sigma \sqrt{N_0}} \left( 1 + \frac{N_0}{N} \right)^{\frac{1}{2}} \\ &= \frac{1}{\sigma \sqrt{N_0}} (1 + \exp[\sigma d])^{\frac{1}{2}} \end{aligned} \quad (4.16)$$

The errors  $\Delta N$  and  $\Delta N_0$  have been associated with the standard deviation. The important experimental figure of merit is the signal to noise ratio which is given by

$$\text{SNR} = \frac{\bar{d}}{\Delta d} = \frac{\bar{d}}{\sqrt{N_0}} \left( 1 + \sqrt{\frac{N_0}{N}} \right)^{-1} \quad (4.17)$$

Figure 4.5 shows the approximate analytical result together with a monte carlo simulation for  $N_0 = 400$ cts. This count level corresponds to the typical imaging situation of the experiments, where the countrate corresponds to an intensity of approximately  $8\% I_{\text{sat}}$ . As can be seen from this comparison, the analytical formula

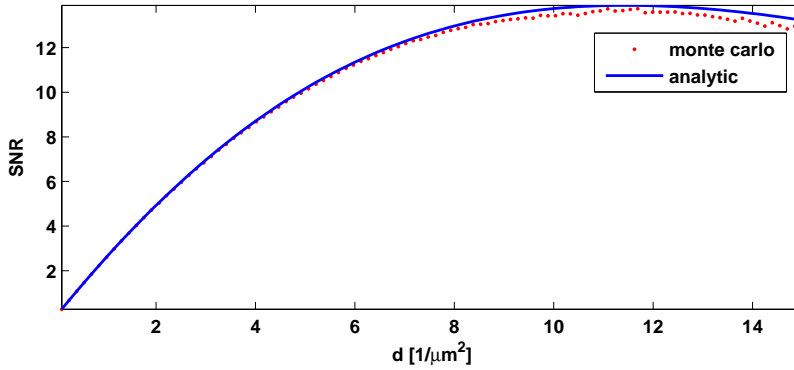


Figure 4.5: *Signal to noise ratio for density detection.* 400cts,  $\sigma$  for the unsaturated linear polarized case. The 400 cts correspond approximately  $8\% I_{\text{sat}}$ .

gives an excellent estimate of the error. A possible statistical bias of the estimated

mean value has been found in the simulation to be smaller than 1%.

The typical column density for absorption images in the magnetometry scans has been around  $d \approx 10^5 / (600\mu m \times 10\mu m) \approx 15 / \mu m^2$  which results in a signal to noise ratio close to the maximum value of about  $\bar{d} / \Delta d = 13$ .

## 4.3 Density distribution

As shown in the introduction, the atomic density is qualitatively different for a harmonically trapped thermal cloud and a condensate. The two types of the distribution will now be deduced.

The trapping potential produced by a static magnetic field necessarily shows a cylindrical symmetry (see section 6.3). The harmonic oscillator potential therefore has to be of the form

$$V(\mathbf{x}) = \frac{m}{2} (\omega_{\perp}^2 r^2 + \omega_x^2 x^2) \quad (4.18)$$

where  $r^2 = y^2 + z^2$ . The distribution of a thermal cloud in this potential is given by the Gaussian distribution

$$n(\mathbf{x}) = n_0 \exp \left[ -\frac{r^2}{w_{\perp}^2} - \frac{x^2}{w_x^2} \right] \quad (4.19)$$

where the width parameters are

$$w_{\perp} = \left( \frac{2k_B T}{m\omega_{\perp}^2} \right)^{\frac{1}{2}} \quad w_x = \left( \frac{2k_B T}{m\omega_x^2} \right)^{\frac{1}{2}} \quad (4.20)$$

and the constant  $n_0$  is determined by the normalization condition  $\int d^3\mathbf{x} n(\mathbf{x}) = N$

$$n_0 = \frac{1}{\pi^{\frac{3}{2}} w_{\perp}^2 w_x} N \quad (4.21)$$

For the condensate distribution the situation is more difficult. In the cases of either very small or very large densities, the interaction energy can either be neglected or becomes completely dominant. In the first case, which is the single particle regime, the ground state is like in the thermal case given by a Gaussian distribution. The width of the cloud however is not determined by thermal energy but by the ground state energy of the oscillator

$$w_{\perp} = \left( \frac{\hbar}{m\omega_{\perp}} \right)^{\frac{1}{2}} \quad w_x = \left( \frac{\hbar}{m\omega_x} \right)^{\frac{1}{2}} \quad (4.22)$$

. In the opposite regime of the Thomas-Fermi limit, the quantum mechanical ground state energy can be neglected compared to the interaction energy. Under these conditions the density distribution becomes an inverted parabola

$$n(\mathbf{x}) = \begin{cases} n_0 \left(1 - \frac{r^2}{w_\perp^2} - \frac{x^2}{w_x^2}\right) & \text{for } \frac{r^2}{w_\perp^2} + \frac{x^2}{w_x^2} \leq 1 \\ 0 & \text{else} \end{cases} \quad (4.23)$$

where the width of the cloud is now caused by the repulsive interaction energy

$$w_\perp = \left(\frac{2gn_0}{m\omega_\perp^2}\right)^{\frac{1}{2}} \quad w_x = \left(\frac{2gn_0}{m\omega_x^2}\right)^{\frac{1}{2}} \quad (4.24)$$

. The normalization condition delivers again the maximum density  $n_0$

$$n_0 = \frac{\mu}{g} = \left(\frac{15}{\pi}\right)^{\frac{2}{5}} \frac{1}{2} \frac{1}{2^{\frac{4}{5}}} \left(\frac{m}{g}\right)^{\frac{3}{5}} N^{\frac{2}{5}} (\omega_\perp^2 \omega_x)^{\frac{2}{5}} \quad (4.25)$$

The Thomas-Fermi density profile opens up the possibility to clearly discern a thermal cloud from a condensate.

In between these two limiting cases, an approximate expression that nicely reproduces the radially integrated line density  $n_1(x) = \int dy \int dz n(\mathbf{x})$  for elongated clouds can be found by a variational procedure.

Following [12] one makes the Gaussian Ansatz

$$\psi(r, x) = \sqrt{\frac{n_1}{\pi w_\perp^2}} e^{-\frac{r^2}{2w_\perp^2}} \quad (4.26)$$

for the ground state wave function and neglects kinetic energy terms connected with derivatives of the wave function along the x-direction. The remaining kinetic energy due to the transverse confinement is given by

$$\frac{\psi^* \nabla^2 \psi}{\psi^* \psi} = \frac{\psi^* \left(\frac{\partial^2}{\partial r^2} + \frac{1}{r} \frac{\partial}{\partial r}\right) \psi}{\psi^* \psi} = \frac{r^2 - 2w_\perp^2}{w_\perp^4} \quad (4.27)$$

For finding the approximate ground state, the energy functional

$$\begin{aligned} \mu[n_1] &= 2\pi \int r dr \left( -\frac{\hbar^2}{2m} \frac{r^2 - 2w_\perp^2}{w_\perp^4} + \frac{m}{2} \omega_\perp^2 r^2 + V(x) \right) \rho + g\rho^2 \\ &= \left( \frac{\hbar^2}{2mw_\perp^2} + \frac{m}{2} w_\perp^2 \omega_\perp^2 + V(x) \right) + \frac{g}{2\pi w_\perp^2} n_1 \end{aligned} \quad (4.28)$$

has to be minimized. The smallest value is obtained for

$$w_\perp = a_0 (1 + 4an_1(z))^{\frac{1}{4}} \quad (4.29)$$

where  $a_0 = \sqrt{\frac{\hbar}{m\omega}}$  is the harmonic oscillator length of a single particle and  $a$  is the s-wave scattering length. Using this optimized width, the equation of state that relates the line density to the potential is given by

$$n_1(x) = \frac{1}{4a} \left[ \left( \frac{\mu - V(x)}{\hbar\omega_\perp} \right)^2 - 1 \right] \quad (4.30)$$

## 4.4 Time of flight measurements

Under usual trapping conditions the width of the density distributions is too small to monitor the density reliably inside the trap. A way to circumvent this problem is to allow the gas to expand for some time after turning off the trapping potential. For an ideal gas, each particle just keeps the initial velocity that it had at the moment when the potential was removed and travels on in a straight trajectory. If the switching process is fast compared to the characteristic time scales of the gas' internal motion the energy is conserved during this process and can be measured from the expansion speed of the cloud. This is also true if the trapped gas is not in the classical ideal gas limit. If the initial density is high, some energy may be stored in the form of interactions between the atoms. Also the quantum mechanical ground state energy may give a significant contribution if the confinement is strong. As long as the expansion characteristics are measured after a long enough time that these effects do not play a role anymore, all the energy will be converted to kinetic energy of the expansion.

### 4.4.1 Expansion of a thermal Cloud

For an ideal classical gas collisions between particles are negligible. Each particular atom follows a straight line trajectory

$$\mathbf{x}(t) = \mathbf{x}_i + \mathbf{v}_i t \quad (4.31)$$

where  $\mathbf{x}_i$  is the initial position and  $\mathbf{v}_i$  the initial velocity. The particle density at the point  $\mathbf{x}$  and time  $t$  after switching off the potential is given by all atoms that have

the right velocity  $\mathbf{v}$  to move from the initial point  $\mathbf{x} - \mathbf{v}t$  to the observation point  $\mathbf{x}$

$$n(\mathbf{x}, t) = \int d^3\mathbf{v} p(\mathbf{v}) n(\mathbf{x} - \mathbf{v}t, 0) \quad (4.32)$$

The probability  $p(\mathbf{v}) = p(v_x)p(v_y)p(v_z)$  to find a particle of velocity  $\mathbf{v}$  is given by

$$p(v_i) = \sqrt{\frac{m}{2\pi kT}} e^{-\frac{mv_i^2}{2kT}} \quad (4.33)$$

For the Gaussian distribution of a thermal cloud the integral can be calculated directly with the result that the expanded distribution is just a scaled version of the initial distribution. The scaled width parameters are given by

$$w_i^2(t) = w_i^2(0) (1 + \omega_i^2 t^2) \quad (4.34)$$

where  $i$  indicates either the transverse or the longitudinal coordinate. For an expansion time that is long compared to the respective transverse or longitudinal oscillator period, the different initial positions of the particles may be neglected and the expansion speed can be directly related to the temperature of the initial configuration

$$\frac{m}{2} \left( \frac{dw_i}{dt} \right)^2 \approx \frac{m}{2} w_i^2 \omega_i^2 = k_B T \quad (4.35)$$

As already mentioned above, the detection by absorption imaging gives only access to the column density  $d(x, z) = \int dy n(x, y, z)$ . Due to the factorization property of the Gaussian function the column density is also a Gaussian

$$d(x, z) = (n_0 \sqrt{\pi} w_\perp) \exp \left[ -\frac{z^2}{w_\perp^2} - \frac{x^2}{w_x^2} \right] \quad (4.36)$$

The width of the optical density can be easily detected and may be used for the measurement of the temperature (see section 2.5.1).

## 4.4.2 Expansion of a Thomas-Fermi Condensate

In the Thomas-Fermi limit all quantum mechanic contributions to the kinetic energy are neglected and the condensate therefore very much behaves like a classical fluid. Following [13] the evolution after switching off of a harmonic trap can be described by the scaling ansatz

$$n(\mathbf{x}, t) = \frac{1}{\lambda_\perp^2(t) \lambda_x(t)} n \left( \frac{x_i}{\lambda_i}, t \right) \quad (4.37)$$

where the scaling factors have to obey the equations

$$\ddot{\lambda}_\perp = \frac{\omega_\perp^2}{\lambda_\perp^3 \lambda_x} \quad \ddot{\lambda}_x = \frac{\omega_x^2}{\lambda_\perp^2 \lambda_x^2} \quad (4.38)$$

which result in

$$\lambda_\perp(t) \approx \sqrt{1 + (\omega_\perp t)^2} \quad (4.39)$$

$$\lambda_z(t) \approx 1 + \left(\frac{\omega_x}{\omega_\perp}\right)^2 \left[ (\omega_\perp t) \arctan(\omega_\perp t) - \log \sqrt{1 + (\omega_\perp t)^2} \right] \quad (4.40)$$

These expressions are valid in the limit of  $\omega_x/\omega_\perp \ll 1$  which is fulfilled in the experiments for all the potentials that have been used ( $\omega_x/\omega_\perp < 2.5\%$ ).

The transverse expansion follows the same scaling law as for a thermal cloud. In this case however, the asymptotic expansion speed is related to the chemical potential instead of a temperature

$$\frac{m}{2} \left( \frac{dw_\perp}{dt} \right)^2 \approx \frac{m}{2} (w_\perp \omega_\perp)^2 = \mu \quad (4.41)$$

The width parameter can be extracted again from the column density which is given now by

$$d(x, z) = \frac{4}{3} w_\perp n_0 \left( 1 - \left( \frac{z}{w_\perp} \right)^2 - \left( \frac{x}{w_x} \right)^2 \right)^{\frac{3}{2}} \quad (4.42)$$

The expansion dynamics that has been just derived can be used as an experimentally accessible standard for the energy scales of a condensate. As the internal energy is dominated in the Thomas-Fermi regime by the density dependent interaction energy this measurement also allows the determination of the number of atoms in the atomic cloud. Figure 4.6 shows a series of pictures of an expanded condensate for increasing time of flight after the switch off of the trap. By a two dimensional fit of the Thomas-Fermi density model to the data the transverse width and the center of mass position can be extracted. These parameters and fitted model curves are shown in figures 4.7 and 4.8. The observed expansion speed corresponds to a chemical potential of  $\mu = (6.6 \pm 0.7) 2\pi\hbar\text{kHz}$ . Using equation 4.25 and the trap frequencies  $\omega_\perp = 838 \times 2\pi\text{kHz}$  and  $\omega_z = 21 \times 2\pi\text{Hz}$  this chemical potential corresponds to a total number of  $N = (1.7 \pm 0.5) 10^5$  atoms. This is a typical value for the clouds that have been used in the scanning experiments. The center of mass evolution shows a free fall parabola in the gravitational field. A comparison of this curve with the well known gravitational acceleration can be used for a calibration of the length scale.

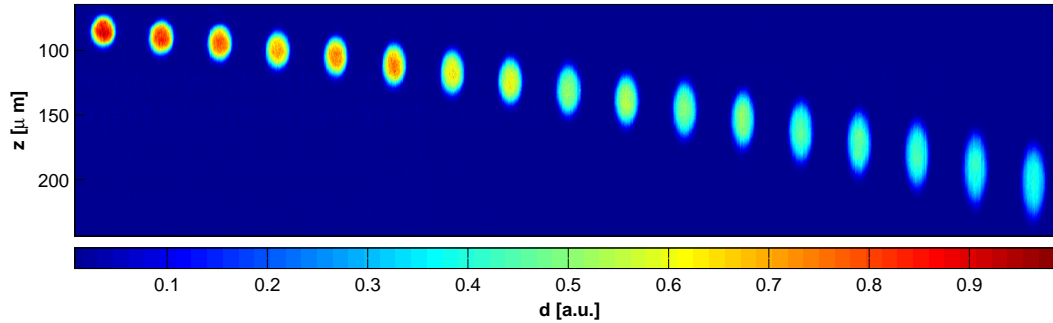


Figure 4.6: *Expansion of a Thomas Fermi condensate.* The series shows the density evolution with increasing expansion time.

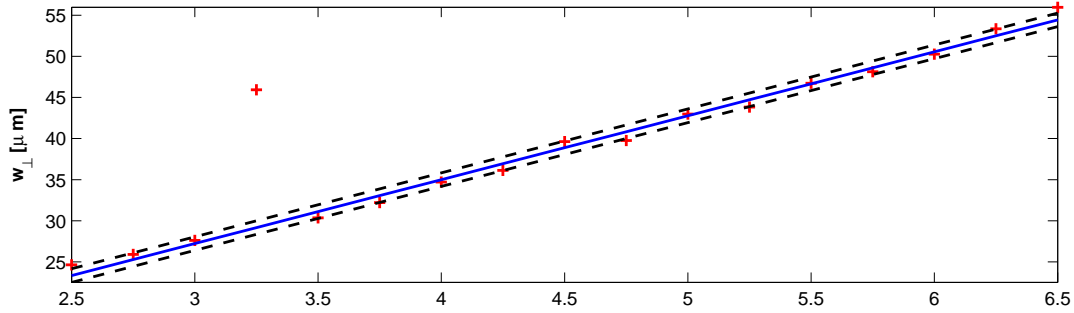


Figure 4.7: *Expanding width.* Transverse Thomas Fermi width with a linear fit. The extracted expansion speed is  $\frac{dw_{\perp}}{dt} = 7.8 \pm 0.4 \frac{\mu\text{m}}{\text{ms}}$ .

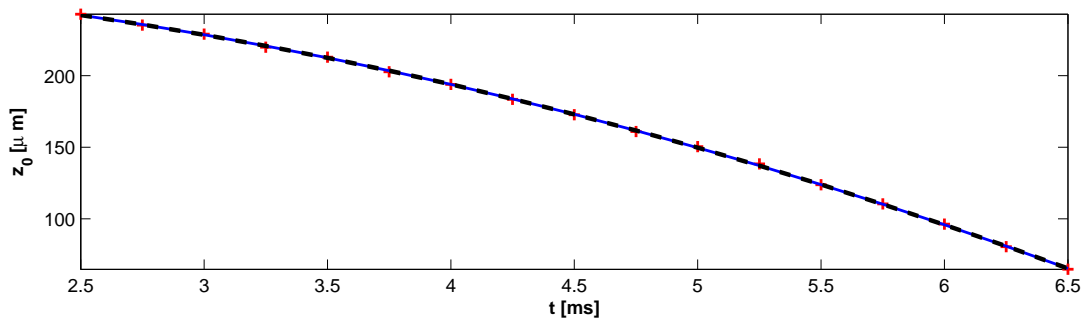


Figure 4.8: *Center of mass position.* Free fall center of mass motion. The fitted parabola gives a gravitational constant of  $g = 9.6 \pm 0.5 \frac{\text{m}}{\text{s}^2}$ .

## 4.5 Oscillations

One of the most fundamental parameter for a harmonically trapped cloud is the oscillator or trapping frequency. In a cylindrically symmetric magnetic trap both, transverse and longitudinal frequencies can be measured by exciting an oscillation through a small time dependent change in the trap parameters. A transverse center of mass oscillation can be directly excited by slightly displacing the trap center. The longitudinal frequency has to be inferred from width oscillations that are excited by a small change in the transverse trap frequency.

### 4.5.1 Center of mass oscillation

According to [14] the center of mass motion in a harmonically shaken trap is decoupled from the relative motion. The solution to the Gross-Pitaevskii equation for a condensate in a harmonically shaken potential

$$V(\mathbf{x}, t) = \sum_{i=x,y,z} \frac{m}{2} \omega_i^2 (x_i - x_{i0}(t))^2 \quad (4.43)$$

can be written as

$$\psi(\mathbf{x}, t) = \psi_0(\mathbf{x} - \mathbf{R}(t), t) \exp(i[\mathbf{P}(t) \cdot \mathbf{x}/\hbar - \phi(t)]) \quad (4.44)$$

where  $\ddot{\mathbf{R}}_i + \omega_i^2(t)(R_i - x_{i0}(t)) = 0$ . For a cloud initially at rest at the trap center position, velocity and the total energy are determined from this equation by

$$\begin{aligned} R(t) &= \int_0^t d\omega t' x_0(t') \sin \omega(t - t') \\ \dot{R}(t) &= \omega \int_0^t d\omega t' x_0(t') \cos \omega(t - t') \\ E &= \frac{m}{2} \omega^2 \left[ \left( \int_0^t d\omega t' x_0(t') \sin \omega(t - t') \right)^2 + \left( \int_0^t d\omega t' x_0(t') \cos \omega(t - t') \right)^2 \right] \end{aligned} \quad (4.45)$$

These expressions allow to calculate the response of the condensate motion to a shift in the cloud center. Experimentally, the excitation of an oscillation can be performed most easily by moving the trap center position in a linear ramp. This movement is performed by a change of the homogenous bias field that adjusts the

trap center. Using two linear ramps, half a period of a harmonic excitation can be approximated by a triangle excitation

$$x(t) = \begin{cases} a\frac{4t}{T'} & \text{for } 0 < t < T'/4 \\ a\frac{4t}{T'} & \text{for } T'/4 < t < T'/2 \end{cases} \quad (4.46)$$

The oscillation energy that is transferred to the cloud by this scheme is shown in figure 4.9 in comparison to a harmonic excitation of the same length. Usually the

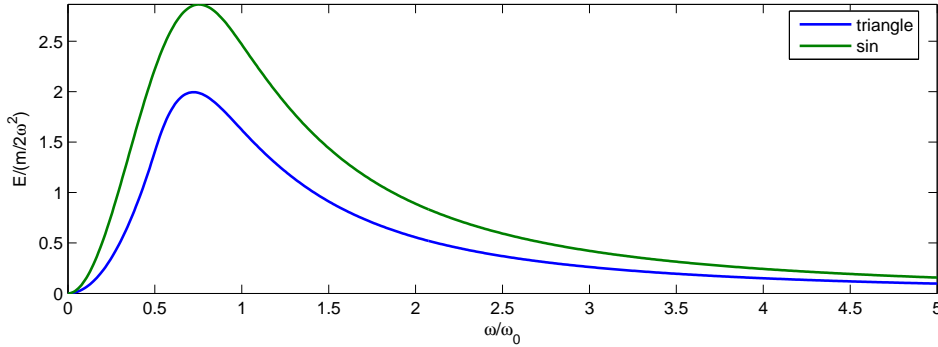


Figure 4.9: *Transferred energy after a  $T/2$  excitation pulse.*

The efficiency of the triangle excitation is nearly as high as that of a real harmonic excitation.

In an experiment the resulting center of mass oscillation can be best resolved after time of flight. The periodic change in the velocity is then translated to a periodic change in position. The figure 4.10 shows a typical example of such an oscillation measurement with a condensate in the standard magnetic trap used for the pre cooling of the atomic clouds. The extracted transverse oscillator frequency of this trap is  $\omega = (838 \pm 3)2\pi\text{Hz}$ .

transverse oscillation mode has an extremely high quality factor. This is a consequence of the exact decoupling of the center of mass degree of freedom from the relative motion even for a many body system that is confined by a harmonic trap [14]. This high quality permits several precise test measurements of parameters that directly influence the transverse trap frequency. As one example, the position of the wire center has been detected in the magnetometry scans by the small symmetric change of the trapping frequency with the distance to the wire center (see section 2.5.2).

A different example is the minute change of the transverse frequency with modulations in the magnetic Ioffe field  $B_i$  along longitudinal trap direction. The trap

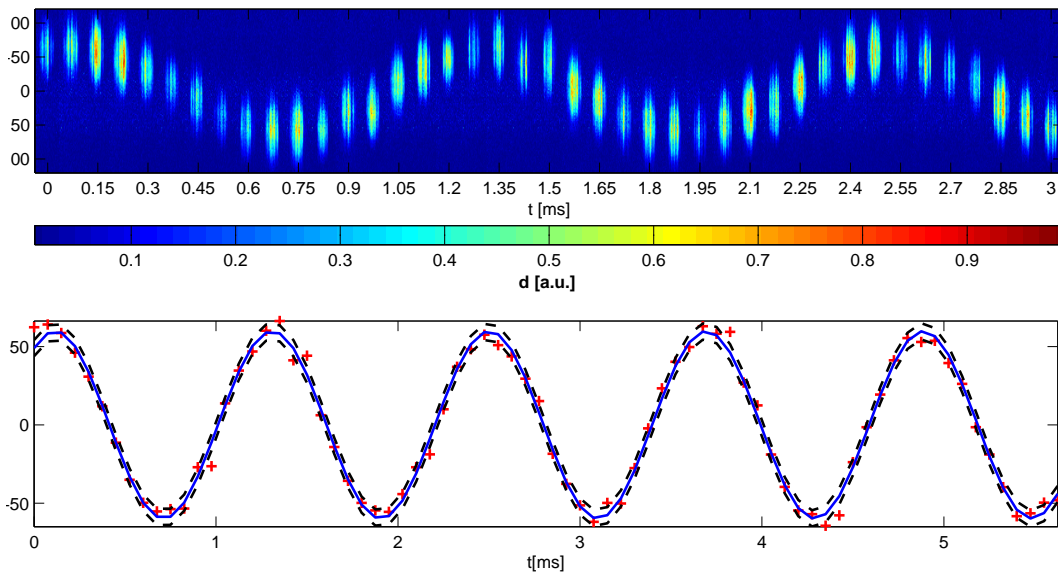


Figure 4.10: *Center of mass oscillation.* **Top:** Column density after time of flight for increasing oscillation time. **Bottom:** Extracted center of mass position, together with a harmonic fit  $\Delta z = A \sin(\omega t + \phi)$  to the data.  $A = 34 \pm 1 \mu\text{m}$ ,  $\omega = (838 \pm 3)2\pi\text{Hz}$ ,  $\phi = (-0.35 \pm 0.01)2\pi$ ,  $\sigma = 3 \mu\text{m}$

frequency depends on this parameter by

$$\omega_{\perp} = \sqrt{\frac{\mu_B}{B_i m}} g \quad (4.47)$$

, where  $g$  is the gradient strength of the trap quadrupole. For the magnetometry scans this change has been neglected as a second order effect. And indeed, it has no measurable influence on the density distribution. However, if two condensates are separated in small regions of slightly different Ioffe field  $B_i$  and  $B_i + \Delta B_i$  this difference can be measured by a phase change between two concurrently excited oscillations. Figure 4.11 shows the result of an experiment where this sensitivity has been used. Two separated clouds have been excited in phase and the oscillation amplitude has been measured after  $T = 90\text{ms}$  which corresponds to  $\approx 82$  periods of oscillation. Then, the mean value of the Ioffe field ( $B_i = 2h\nu_{\text{rf}}/\mu_B$ ) has been increased and the phase of both oscillations has been measured at a fixed oscillation hold time of 90ms. By this technique changes of about 10mG are directly resolved by the changing oscillation phase.

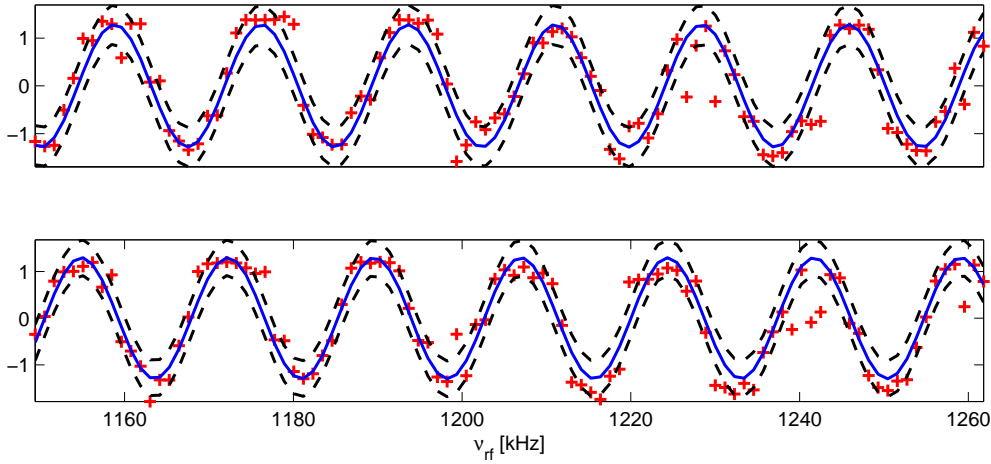


Figure 4.11: *Phase change with the Ioffe field.* The two panels show the center of mass position (a.u.) after 90ms of oscillation for two separated condensates in slightly different Ioffe fields. The increase of the mean Ioffe field  $B_i = 2h\nu_{\text{rf}}/\mu_B$  shows up as a harmonic variation of the oscillation phase at fixed oscillation time. The absolute calibration of the frequency scale is  $\Delta\nu = \pm 10\text{kHz}$  the linearity is better than 0.01. The model  $a \cos \omega\nu - \phi$  has been fitted to the center of mass positions **upper panel**:  $a = 1.28 \pm 0.1$ ,  $\omega = (5.75 \pm 0.05)10^{-2} \frac{2\pi}{\text{kHz}}$ ,  $\phi = -437 \pm 7$ , **lower panel**:  $a = 1.3 \pm 0.1$ ,  $\omega = (5.76 \pm 0.04)10^{-2} \frac{2\pi}{\text{kHz}}$ ,  $\phi = -443 \pm 3$ . Hold time 90ms.

### 4.5.2 Width oscillation

As already noted, the longitudinal frequency  $\omega_x$  can not easily be measured by a center of mass oscillation. In order to shake the magnetic trap in the longitudinal direction, an additional gradient field in this direction that can be controlled separately would be needed. However, the ratio of transverse and longitudinal frequency can be deduced from a width oscillation of the condensate.

Like in the treatment of a free expansion the width oscillation can be described in terms of a scaling solution [13] where the scaling parameters are determined by

$$\ddot{\lambda}_\perp = \frac{\omega_\perp^2(0)}{\lambda_\perp^3 \lambda_x} - \omega_\perp^2 \lambda_\perp \quad (4.48)$$

$$\ddot{\lambda}_x = \frac{\omega_x^2(0)}{\lambda_x^2 \lambda_\perp^2} - \omega_x^2 \lambda_x \quad (4.49)$$

Linearizing this set of equations for small amplitudes  $\lambda = 1 + \delta\lambda$  results in

$$\frac{d^2}{dt^2} \begin{pmatrix} \lambda_\perp \\ \lambda_x \end{pmatrix} = -\omega_\perp^2 \begin{pmatrix} 4 & 1 \\ 2\epsilon^2 & 3\epsilon^2 \end{pmatrix} \begin{pmatrix} \lambda_\perp \\ \lambda_x \end{pmatrix} - \begin{pmatrix} \omega_\perp(t) - \omega_\perp^2 & 0 \\ 0 & 0 \end{pmatrix} \begin{pmatrix} \lambda_\perp \\ \lambda_x \end{pmatrix} \quad (4.50)$$

where the ratio  $\epsilon = \omega_x/\omega_\perp$  has been introduced. The eigenmodes and frequencies of this system can be determined by substituting the ansatz  $\lambda_{\perp/x} = a_{\perp/x} \exp[i\Omega t]$  in the equations. To leading order in  $\epsilon$  the resulting modes and frequencies  $\Omega$  are given by  $(a_\perp, a_x) = (1, 0)$  for  $\Omega = 2\omega_\perp$  and  $(a_\perp, a_x) = (1, -4)$  for  $\Omega = \sqrt{\frac{5}{2}}\omega_x$ . In the slow mode the scaling parameters along the transverse and the longitudinal mode are coupled. This means that this mode can be excited by a modulation of the transverse trapping frequency. The oscillation frequency of the slow mode is however directly related to the longitudinal trapping frequency by  $\Omega = \sqrt{\frac{5}{2}}\omega_x$ . As the transverse trapping frequency depends on the Ioffe by  $\omega_\perp \propto 1/\sqrt{B_i}$  the excitation of the oscillation can be accomplished in a similar way to the transverse center of mass oscillation by a small triangular excitation pulse now on the Ioffe field. The resulting width-oscillation is shown in figures 4.12 and 4.13. From the observed frequency  $\Omega = (33.7 \pm 0.3)2\pi\text{Hz}$  the longitudinal trapping frequency is deduced  $\omega_x = \sqrt{2/5}\Omega = (21.3 \pm 0.2)2\pi\text{Hz}$ .

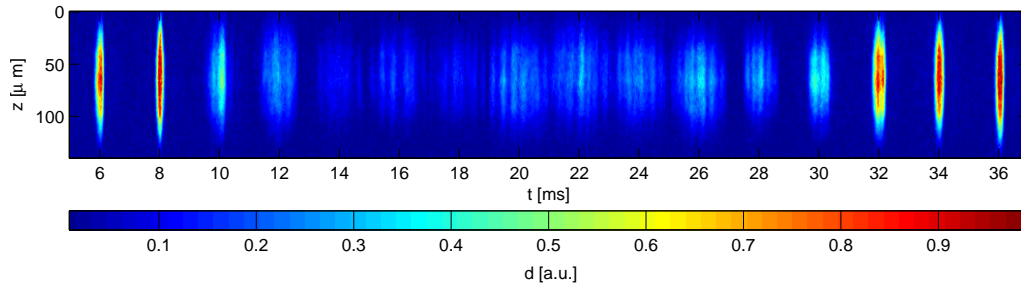


Figure 4.12: *Cloud deformation during a width oscillation.* The pictures show the column density  $d$  in relative units of an excited condensate after expansion.

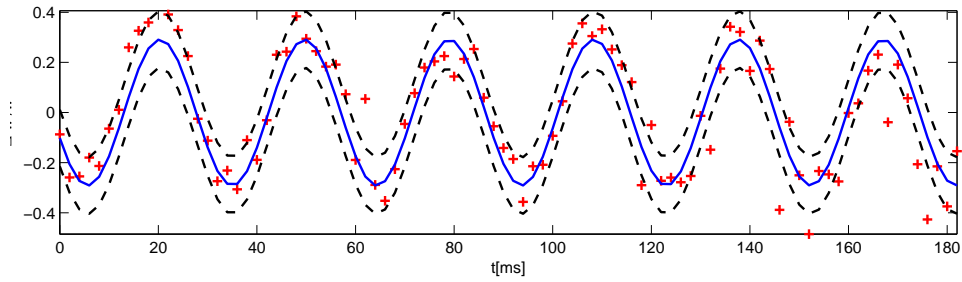


Figure 4.13: *Relative width during a quadrupole oscillation.* Relative width  $(w - \bar{w})/\bar{w}$ , where  $\Delta w = \sqrt{\langle (w - \bar{w})^2 \rangle} = 2.8\mu m$ .  $\bar{w} = 15.4\mu m$ . Fitted model  $\frac{\Delta w}{\bar{w}} = A \sin(\sin \Omega t + \phi)$ . Extracted parameters  $A = 1.3 \pm 0.1$ ,  $\Omega = (33.7 \pm 0.3)2\pi \text{ Hz}$ ,  $\phi = (-0.43 \pm 0.03)2\pi$

## 4.6 Rf-Spectroscopy

In the previous section it has been shown, that the Ioffe-field  $B_i$  can be measured by its direct influence on the transverse oscillator frequency. A different independent method for this purpose that is usually more precise is rf-spectroscopy.

Close to the trap center, the magnetic field direction is dominated by the Ioffe field  $B_i \mathbf{e}_x$  that is aligned with the longitudinal trap axis. In the adiabatic trapping scheme the atoms occupy the  $|F = 2, m_F = 2\rangle$  state in a local coordinate system that is aligned with the Ioffe-field. If now an additional rf-field is applied, which is linearly polarized in the plane perpendicular to the Ioffe field direction, an NMR-configuration is realized. If the rf-frequency  $\nu_{rf}$  is close to the Lamor frequency  $\nu_L = g_F \mu_B B / h$ , where  $g_F = 1/2$  is the Lande-factor, a resonance condition occurs and a small rf-amplitude is able to rotate the spin direction into an untrapped state where the atom is repulsed by the field. Not all the atoms of cloud sit directly at the trap center where  $B = B_i$ . Some occupy positions of higher potential energy and therefore of higher magnetic field. Therefore, there is not a unique resonance condition for all the atoms but a whole range that corresponds to the occupied field magnitudes.

There are two slightly different ways how such a resonance scheme can be used to measure the Ioffe field. In the first, the rf is swept from frequencies far above the resonance condition of the Ioffe field  $\nu_{rf} \gg \mu_B B_i / 2h$  to some final frequency  $\nu_f$  closer to it. Depending on the value of the final frequency the resonance condition has been met during this sweep for a certain part of the cloud. If the rf-amplitude is adjusted to be large enough, that all the atoms are lost during such a sweep over the resonance condition, only those atoms will remain trapped that occupy magnetic field values below  $B < h\nu_f / g_F \mu_B$ . Setting the final frequency closer and closer to the resonance condition of the Ioffe field, the corresponding resonance frequency can be extrapolated as the point, where all atoms are lost by the rf sweep. Figure 4.14 shows how the total number of atoms in the trap decreases with decreasing rf-frequency. The absolute accuracy in the Ioffe field that has been obtained by this method is  $\Delta B_i = 5\text{kHz} \times 2h / \mu_B$ .

In a second slightly different variant of this method, the rf-amplitude is adjusted low enough that not all the atoms are lost from the trap, once they have met the resonance condition. In this way a complete rf-sweep down to the Ioffe field couples out a continuous beam from the condensate. Such an atom laser experiment [15] is shown in figure 4.15. For the determination of the Ioffe-field this method has no immediate advantage compared to the first one. In principle a higher frequency

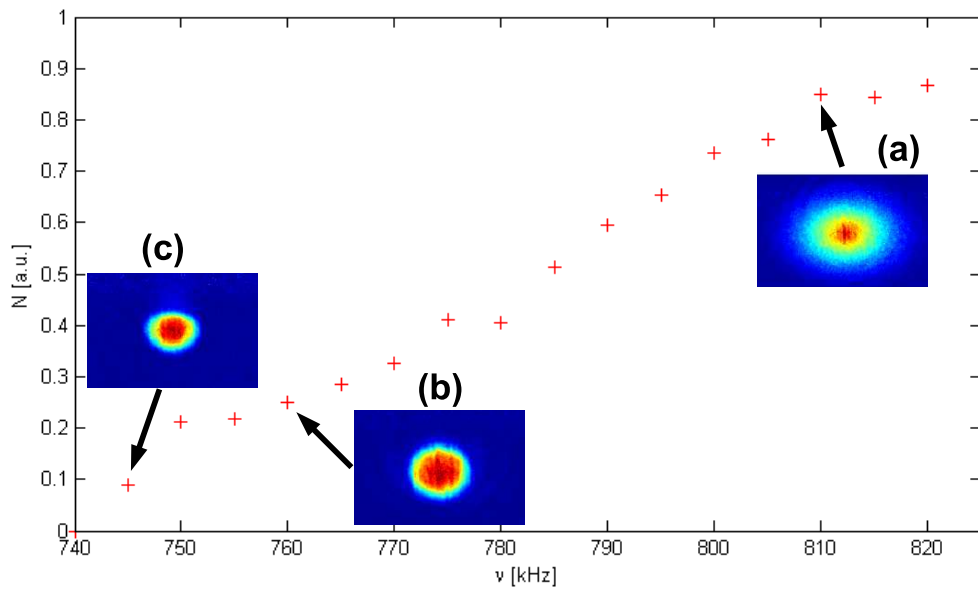


Figure 4.14: *Rf-Spectroscopy*. The rf-frequency is swept from a value far above the resonance condition of the Ioffe field to some final value  $\nu$  closer to it. The remaining number of atoms in the trap  $N$  is plotted in arbitrary units. During this sweep the cloud is cooled evaporatively from a thermal regime (a) to a condensate (b)/(c). The images show the density distributions that respectively correspond to the total atom number values.

resolution can be achieved, but it can only be realized if the interaction energy of the atoms remaining inside the trap is properly taken into account. For the calibrations in this work the first method has therefore been used.

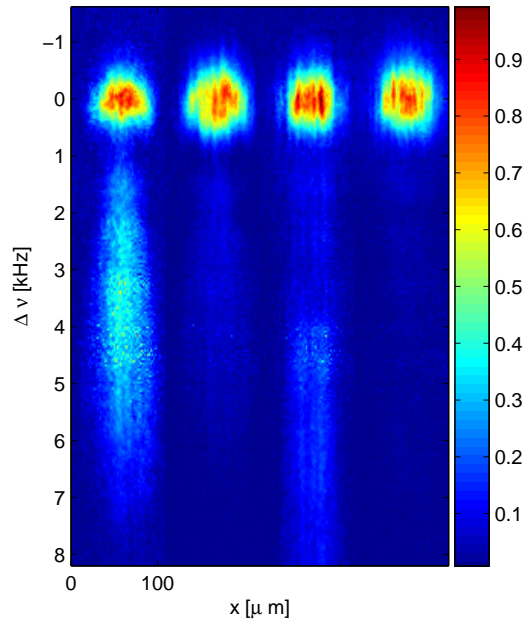


Figure 4.15: *Atomlaser for increasingly weaker outcoupling rf.* The pictures show the column density  $8ms$  after turning off the trapping potential. In all pictures the frequency was swept at approximately  $0.5 \frac{\text{kHz}}{\text{ms}}$  over the trap bottom ( $B = B_i$ ). The trap bottom was on average at  $785\text{kHz}$ . Its typical shot to shot fluctuations were around  $1\text{kHz}$ . The rf-amplitude is decreased from left to right. (In relative units  $1, 0.7, 0.6, 0.4$ )

# Bibliography

- [1] Bose,S. Plancks Gesetz und Lichtquantenhypothese. *Z. Phys.* **26**, 178 (1924)
- [2] Einstein,A. Quantentheorie des einatomigen idealen Gases. *Berl. Akad.*, **3** (1925)
- [3] London,F. On the Bose-Einstein condensation. *Phys. Rev.*, **54**, 947 (1938)
- [4] Bardeen,J. Cooper,N. Schrieffer,J.R. Theory of superconductivity. *Phys. Rev.*, **108**, 1175 (1957)
- [5] Davis,K.B. et. al. Bose-Einstein condensation in a gas of sodium atoms. *Phys. Rev. Lett.* **75**, 3969 (1995)
- [6] Anderson,M.H. et. al. Observation of Bose-Einstein condensation in a dilute atomic vapor. *Science* **269**, 198 (1995)
- [7] Pethick,C.J. Smith,H. Bose-Einstein condensation in dilute gases. *Cambridge University Press* ISBN 0 521 66580 9 (2002)
- [8] Ye,J. Swartz,S. Jungner,P. Hall,J.L. Hyperfine structure and absolute frequency of the  $^{87}\text{Rb}$   $5P_{3/2}$  state. *Opt.Lett.* **21**, 1280 (1996)
- [9] Bize,S. et. al. High-accuracy measurement of the  $^{87}\text{Rb}$  ground-state hyperfine splitting in an atomic fountain. *Europhys. Lett.* **45**, 558 (1999)
- [10] Steck,D.A. Rubidium 87 D line data. <http://steck.us/alkalidata> (2003)
- [11] Ketterle,W. Durfee,D.S. Stamper-Kurn,D.M. Making, probing and understanding Bose-Einstein condensates. *arXiv.org*, cond-mat/9904034v2 (1999)
- [12] Gerbier,F. Quasi-1D Bose-Einstein condensates in the dimensional crossover regime. *Europhys. Lett.* **66**, 771
- [13] Castin,Y. Dum,R. Bose-Einstein Condensates in Time Dependent Traps. *Phys. Rev. Lett.* **77**, 5315 (1996)
- [14] Japha,Y. Band,Y.B. Motion of a condensate in a shaken and vibrating harmonic trap. *J. Phys. B: At. Mol. Opt. Phys.* **35**, 2383 (2002)
- [15] Bloch,I. Hänsch,T.W. Esslinger,T. Atom Laser with a cw Output Coupler. *Phys. Rev. Lett.* **82**, 3008 (1999)

---

# 5 Imaging Close to a Mirror

---

## 5.1 Introduction

Magnetic microtraps [1] opened up the possibility to exploit the sensitivity of ultracold alkali atoms as a probe for surface related potentials and magnetic noise [2, 3, 4, 5, 6]. Some of these applications depend very critically on a precise measurement of the atoms height above the surface. In the usual case where most of the surface is covered by a reflective metal film, the standard technique to determine the height [7] uses the distance between image and mirror image of the atomic cloud. Here it is shown, that close to the surface two effects may lead to a departure from what is expected by geometrical optics.

The basic mechanism of absorption imaging has already been introduced in section 4.2. Atoms that are illuminated by a collimated, resonant laser beam absorb a certain fraction of the incident intensity and re-emit it with equal probability into any spatial direction. This scattered light is missing from the laser beam and produces a shadow on it, after it has passed the atomic cloud. When a lens system (see figure 5.1) is used to image the laser beam with its focus in the plane containing the atomic cloud, an image of the wavefront, directly after passing through the atoms can be retrieved. From the intensity, that is reduced from the value  $I_0$  to  $I'$  the column density  $d(x, z) = \int dyn(x, y, z)$  can be extracted by Beer-Lambert's law

$$I'(x, z) = I_0 \exp[-\sigma d(x, z)] \quad (5.1)$$

. In the imaging of atoms close to a mirror the ideal conditions, where the imaging beam propagates in free space before and behind the absorbing cloud, can not be implemented. For the analysis of the problem, the propagation of the light wave in

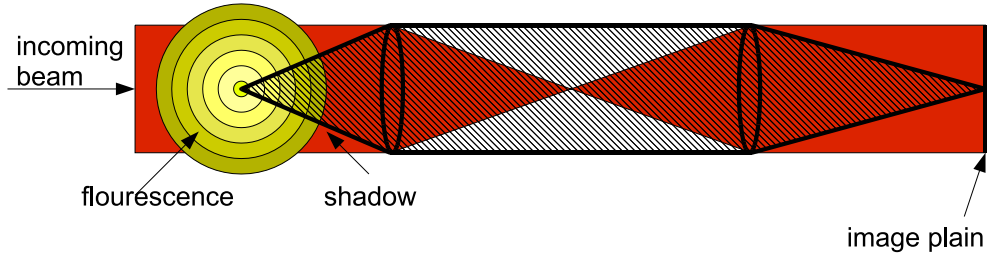


Figure 5.1: Absorption imaging of an atomic cloud.

presence of mirror boundary conditions has to be considered. In the propagation of a wave, the fundamental quantity obeying the wave equation is not the intensity, but the electric field. As the superposition principle holds for waves, the electric field  $E'$  directly behind the cloud may be represented as the difference of the electric field  $E_0$  that would be there in absence of the atoms and some scattered field  $E_{sc}$  that describes the shadow cast by the absorber. However, care has to be taken when performing such a decomposition. In general  $\sqrt{\epsilon_0 c / 2 E_{sc}} \neq \sqrt{I_0 - I'}$ . For assuring consistency between intensities and electric field amplitudes the following requirements have to be met

$$\begin{aligned}
 I' &= I_0 - I_{sc} & (5.2) \\
 E' &= E_0 - E_{sc} \\
 \frac{1}{2} \epsilon_0 c E_0^2 &= I_0 \\
 \frac{1}{2} \epsilon_0 c E'^2 &= I'
 \end{aligned}$$

From these, the scattered field can be computed to be

$$E_{sc} = E_0 \sqrt{1 + (1 - a) - 2\sqrt{1 - a}}, \quad (5.3)$$

where the relative absorption  $a = I_{sc}/I_0$ , that can assume values between 0 and 1, has been introduced. The complicated form of the scattered field is due to the presence of interference terms between the two electric fields used in the decomposition. In particular, the square of the scattered field is in general not proportional to the intensity computed from this field alone

$$\begin{aligned}
 I_{sc} &\neq \frac{\epsilon_0 c}{2} E_{sc}^2 \text{ for } 0 < a < 1 & (5.4) \\
 I_{sc} &= \frac{\epsilon_0 c}{2} E_{sc}^2 \text{ for } a = 0 \text{ or } a = 1
 \end{aligned}$$

Two exceptions are found for complete absorption or complete transmission. These special are known as Babinet's principle. In the case of a weak absorber, that will

be of concern in the following analysis, the expression for the scattered electric field may be simplified to

$$E_{sc} \approx \frac{1}{2} a E_0 \text{ for } a \ll 1 \quad (5.5)$$

## 5.2 Absorption Imaging Close to a Mirror

When applying the scheme of absorption imaging close to a mirror surface, some changes to this method necessarily have to be made. The illumination by a beam running parallel to the surface and having its focus centered on the atoms quickly becomes impossible. At a height  $h$  above the surface, the length of the mirror  $l$  limits the usable numerical aperture to  $NA = 2h/l$ . The minimum spot radius on the other hand should be smaller than  $h$  to avoid a beam that is touching the surface. For a Gaussian beam this leads to the limit of  $h \geq \sqrt{\lambda l/\pi}$ . In the case of  $^{87}\text{Rb}$  atoms ( $\lambda = 780\text{nm}$ ) and  $l = 1\text{cm}$  the limit is reached already at  $h = 50\mu\text{m}$ .

In order to allow a controlled illumination below this height, the simplest solution is to incline the beam by a small angle  $\theta$  to the mirror surface. This setup is depicted schematically in figure 5.2 (a). In contrast to the usual absorption imaging setup there are now two beam paths that traverse the cloud. Beam (1) is being reflected before passing through the cloud and beam (2) afterwards. A lens system that is used to form an image from the reflected light images the shadow cast on beam (1) to a real image and that of beam (2) on the mirror image. Such an image is shown in 5.2 (b). The distance between the cloud and the mirror cloud equals twice the height above the on surface. As the absorbing clouds usually are very elongated in the experiments, the imaging problem may be simplified by assuming a slowly varying absorption profile along the long axis ( $y$ ) and treating only the change in absorption along the transverse direction ( $x$ ).

The simple geometrical picture neglects two important wave effects. First, in the overlap region, where the incoming and the reflected part of the imaging beam interfere, a standing wave field with its wavefront parallel to the chip surface is formed. Second, the mirror acts as an asymmetric aperture and the image formed by the lens may differ significantly from the original distribution. These two effects will now be estimated for the simplified case of an infinitely long, perfectly reflecting, plane mirror surface.

The electric field of the incoming wave  $E_i$  and the wave reflected at  $x = 0$   $E_r$

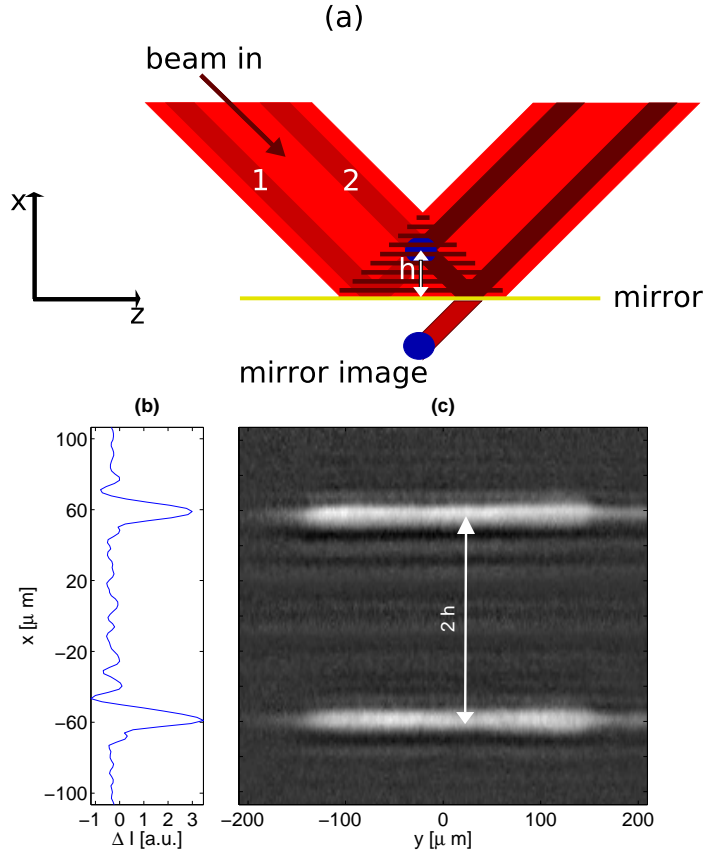


Figure 5.2: *Mirror imaging.* (a) Reflection imaging above a mirror surface. The absorbing cloud (blue disc) is passed by two different beam paths. For (1) the incoming is reflected before passing through the cloud for (2) it is reflected afterwards. Path (1) is mapped by a focused lens to a real image, path (2) to a mirror image. In addition to this geometric effect, the reflected beam forms a standing wave pattern in the overlap region with the incident beam. (b/c) (c) shows a focused image of the absorbed intensity  $I_{sc}$ . The modulation in intensity is caused by diffraction from the mirror geometry and is not a defocus. The distance between image and mirror image is equal to twice the height above the surface. In (b) a cross section of the image in (c) is shown. Due to the longitudinal symmetry, it is sufficient to treat only the variations along the transverse direction .

may be adequately approximated by the plain waves

$$\begin{aligned} E_i &= E_0 \exp [i (k(\sin \theta_i x - \cos \theta_i z) - \omega t)] \\ E_r &= -E_0 \exp [i (k(\sin \theta_i x + \cos \theta_i z) - \omega t)]. \end{aligned} \quad (5.6)$$

The total field  $E = E_i + E_r$  vanishes at the surface and therefore fulfills the boundary condition for an ideal metallic mirror. The two components interfere in a region of overlap, to form a standing wave pattern.

$$I_{\text{sw}}(x) = 4I_0 \sin^2(k_x x) \quad (5.7)$$

where  $I_0 = \epsilon_0 c E_0^2 / 2$  is the intensity of a single beam and  $k_x = \sin \theta_i 2\pi / \lambda$  the wavevector component perpendicular to the surface.

This illumination by a standing wave is highly inhomogeneous and in stark contrast to the usual absorption imaging. The effect of this inhomogeneity very much depends on the size of the absorber. If the scattered intensity  $I_{\text{sc}}$  behind the cloud is approximated by a Gaussian profile

$$I_{\text{sc}}(x) = I_{\text{sw}} A \exp [-(x - h)^2 / w^2] \quad (5.8)$$

the total power scattered out of the standing wave is given by

$$P_{\text{sc}} = \int dx I_{\text{sc}}(x) = 2P_0 \left[ 1 - \cos 2k_x h e^{-k_x^2 w^2} \right] \quad (5.9)$$

where  $P_0$  is the power that would be scattered by the same absorber in a single plain wave of intensity  $I_0$ . As the cloud is moved through the standing wave, it probes the local intensity. Depending on the size of the cloud, it truly samples the intensity, or averages over a broader range. The fringe visibility  $V$  reflects this size dependent spatial resolving power of the cloud

$$V = \frac{P_{\text{sc,max}} - P_{\text{sc,min}}}{P_{\text{sc,max}} + P_{\text{sc,min}}} = e^{-k_x^2 w^2}. \quad (5.10)$$

There are basically two different regimes depending on the width of the cloud. For  $k_x w \gg 1$  the scattered power is twice the amount obtained from plain wave illumination. This is the regime of geometric optics that has been addressed in [7]. The light passing through the cloud can be thought of as coming from two beams (see figure 5.2 (a)) where one is hitting the cloud directly and the other one is first reflected by the mirror. For a cloud size much larger than  $1/k_z$  this setup is equivalent to an incoherent illumination by two beams, which explains the doubling of the scattered power compared to a single plain wave. In the other extreme limit, where the cloud is small compared to the standing wave ( $k_z w \ll 1$ ) the scattered power is determined by the local intensity at the position of the atoms. This intensity is modulated between complete darkness and twice the mean intensity, depending on

the position within the standing wave. As the phase of the standing wave is fixed by the surface, this modulation of the scattered power could be used as a reference ruler for the distance to the mirror surface.

By varying the position  $z_0$  and counting the minima and maxima of the detected scattered power it is possible in principle to determine the absolute position above the surface. Figure 5.3 shows the result of such an experiment. The total scattered

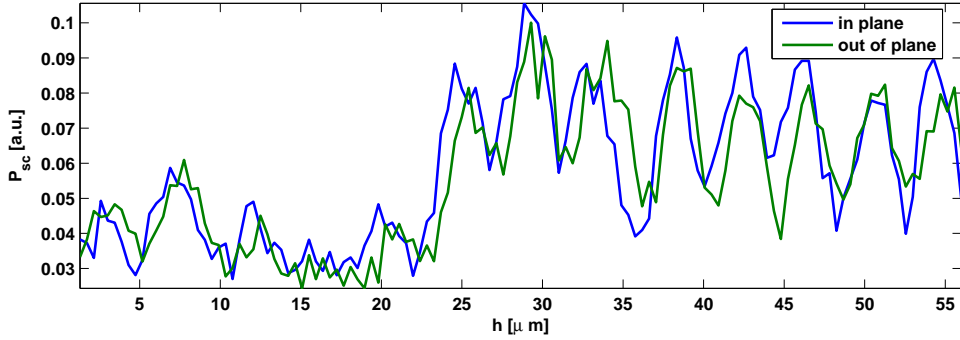


Figure 5.3: *Standing wave*. The total scattered power is shown for trapped condensates at different heights above wire **a**. The blue and green curve shows the result for in plane and out of plane linear polarization of the imaging beam. These have a small relative phaseshift which is caused by the different boundary conditions of the standing wave at the mirror surface. The inclination of the imaging beam is  $\theta \approx 4.2^\circ$ .

power has been measured for trapped condensates at different height levels above the surface of wire **a**. The blue curve shows the result for an imaging beam which is linearly polarized in the plane of incidence, whereas the green curve corresponds to perpendicular polarization. As can be seen clearly, the power does not simply follow a harmonic modulation on the large scale. Several phase shifts and changes in the modulation amplitude appear. These artefacts are caused by the wire structures on the chip surface. The dominant effects can be explained by the different height levels of the wires. These cause a phase shift of the reflected beam that is proportional to the local surface corrugation. As the reflected beam has to propagate a significant distance to reach the position of the atomic cloud, diffraction has a large influence on the observed patterns.

A second effect that is independent of the surface structure is connected to the non-ideal boundary conditions of a real gold surface. The phase shift that occurs during reflection is not exactly equal to  $\pi$  and depends on the polarization of the reflected wave. Different phaseshifts of the reflected beams translate into a phase-shift of the standing wave. It can be observed between the curves for linear in-plane

and out-of-plane polarization. (The experimental findings have been compared to numerical calculations using the methods of section 5.4.1 and 5.4.2 and found to be consistent with a phaseshift-model based on the known chip structure. However, as the full presentation of these calculations is very lengthy and no additional physical information may be obtained from them, they will not be presented here.)

All the effects taken together make the idea of using the standing wave periodicity for an exact height determination impractical. For the microscopy scans of this work, the imaging beam has been inclined by a large enough angle, that the typical standing wave periodicity is much smaller than the transverse sizes under interest. Under this condition the fringe visibility is very low and the detection efficiency becomes independent of the height position above the surface.

A different effect, that is largely independent of the modulation on the total scattered power is a kind of diffraction that is present even for an ideal mirror. Difficulties arise because the mirror plane acts similar to an aperture.

For an ideal metallic mirror, the wave amplitude is zero at the mirror surface. This boundary condition may always be imposed by complementing an arbitrary wavefront above the surface by its mirror image. The principle of this procedure is depicted graphically in figure 5.4. A symmetric absorber that is illuminated by a

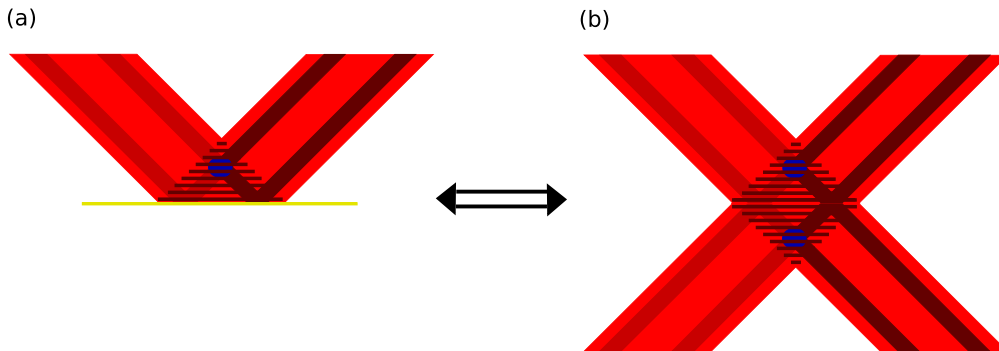


Figure 5.4: *Method of mirror image.* **(a)** The imaging beam is reflected from the mirror and forms a standing wave in the overlap region. The absorber is modulated by this pattern. **(b)** The mirror can be replaced by an antisymmetric mirror image of the wavefront above the surface.

standing wave may be modelled in the plane of the absorber by

$$\psi(z) = [a(x - h) + a(x + h)] \sin(k_x x) \quad (5.11)$$

where  $a(x)$  is a symmetric, real valued function and the mirror surface is assumed to be at  $x = 0$ .

If a lens would be able to collect all the light from the real and the mirror source, it would just produce a focused image of the initial wavefront. However, as the lens can in reality never have access to plain wave components staying below the

mirror plane these are effectively blocked as by an edge. Within the Fraunhofer approximation, diffraction due to this effect can be easily computed in Fourier space. When decomposing the initial wavefront into plain waves, only those components will finally propagate out from the mirror that have a wavevector component  $k_z > 0$ . The effect of the mirror can therefore be described by setting  $\psi(k_z < 0) = 0$ . A comparison of this simple model with the observed diffraction above wire **a** is given in figure 5.5. The model calculation does not include the shadowing and apparent

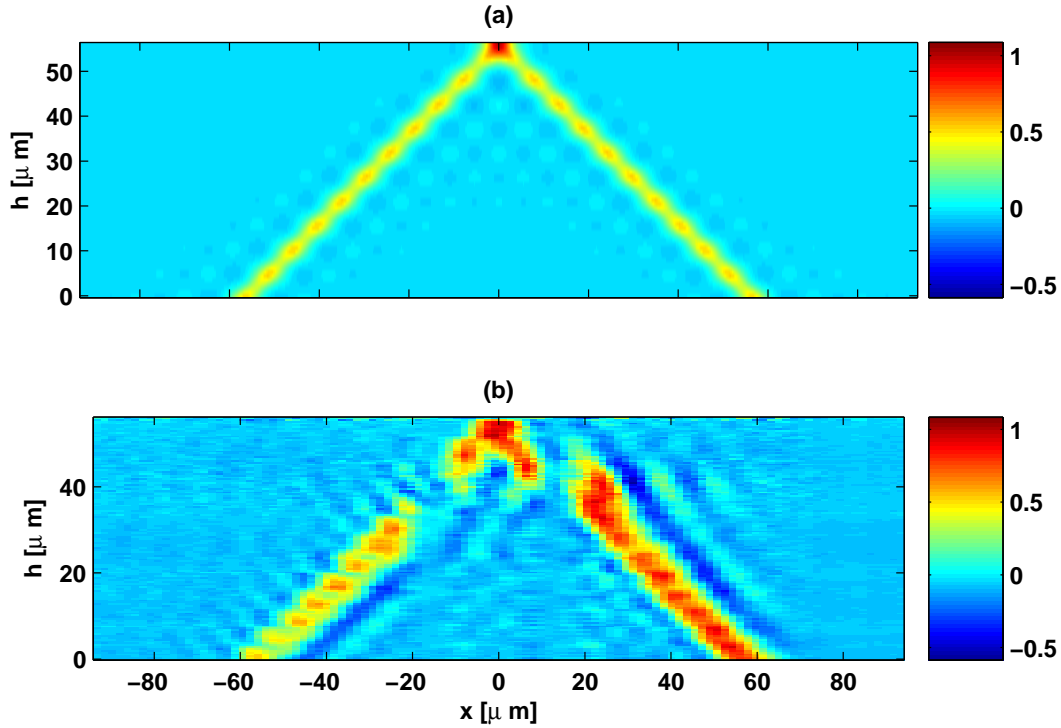


Figure 5.5: *Diffraction by the mirror.* The pictures show the scattered intensity  $I_{\text{sc}}$  for trapped condensates at different height above the surface compiled into a single picture. The colormap encodes  $I_{\text{sc}}$  in arbitrary units. **(a)** Simulation of the diffraction assuming a Gaussian absorber  $E_{\text{sc}} \propto \exp -(x-h)^2/w^2$  of width  $w = 3\mu\text{m}$  and an imaging angle of  $\theta = 4.2^\circ$ . **(b)** Measured intensity above wire **a**.

jump of the cloud position which is caused in the measured pictures by reflection from wires of different surface height. If these artefacts are neglected, there is a good qualitative agreement between the two pictures. Diffraction smears out the scattered wavefront  $E_{\text{sc}}$  over a range that is inversely proportional to the linear size of the absorbing cloud. The illuminating plain wave however is unaffected. In

the total intensity  $I \propto |E_0 - E_{sc}^d|^2$  the diffracted wave  $E_{sc}^d$  interferes with the plain imaging wave  $E_0$ . This leads to the typical interference fringes around the central maxima. Their spatial extent is consistent with an effective width of the cloud of approximately  $3\mu m$ . In reality, the width is smaller. The finite aperture of the imaging telescope however limits the spatial resolution to  $\approx 3\mu m$ .

## 5.3 Extraction of the Cloud Position

The modulation of the scattered power by the standing wave can be sufficiently suppressed by using a high enough angle of incidence. When the standing wave period becomes significantly smaller than the transverse size of the cloud the modulation practically vanishes. Diffraction effects however, can not be suppressed easily in this way. Therefore, they have to be taken into account for an exact determination of the cloud's center position. The problem, that has to be addressed can be understood by the drawing of figure 5.6. Here, the light path that leads to the mirror image

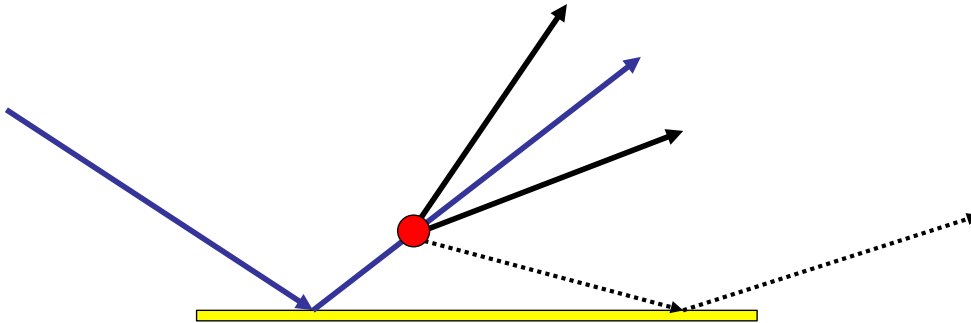


Figure 5.6: *Angular aliasing*. The atomic absorber (red disc) is illuminated by a plain wave that is reflected from the mirror surface before passing through the cloud (blue lines). The scattered wave  $E_{sc}$  propagates into a cone where the opening angle depends inversely proportional on the width of the cloud. If a plain wave component is reflected by the surface (dotted line), it exits the mirror under an angle that is already occupied by a wave component the directly travels away from the mirror.

of the atomic cloud is sketched. The discussion for the direct image can than be inferred analogously.

The illuminating plain wave is reflected by the mirror surface and then passes through atomic cloud. If the size of this cloud is large, there is only a geometric shadow that propagates along the same direction as the plain wave. However,

as the cloud becomes smaller, the scattered wave  $E_{\text{sc}}$  occupies a larger and larger angle spread around the direction of the plain wave. As long as this spread is small compared to the angle of incidence, all the light directly propagates away from the mirror. A lens will reconstruct the true wavefront in the object plane. This situation changes when the angle spread of the scattered wave becomes large enough, that a significant amount is propagating in a direction towards the mirror surface. This part of the wave is reflected and thereby wrongly mapped to an angle under which another part of the wave travels directly away from the mirror. This aliasing effect is most important in the regime of large scattering angles. For small angles, the spectrum more and more resembles that of the correctly mapped image.

This understanding can now be used for the extraction of the cloud position. An experimentally determined profile of the scattered intensity  $I_{\text{sc}}(x)$  can be decomposed into its plain wave components  $I_{\text{sc}}(x) = \frac{1}{2\pi} \int dk_x e^{ik_x x} I_{\text{sc}}(k)$ . For each plain wave

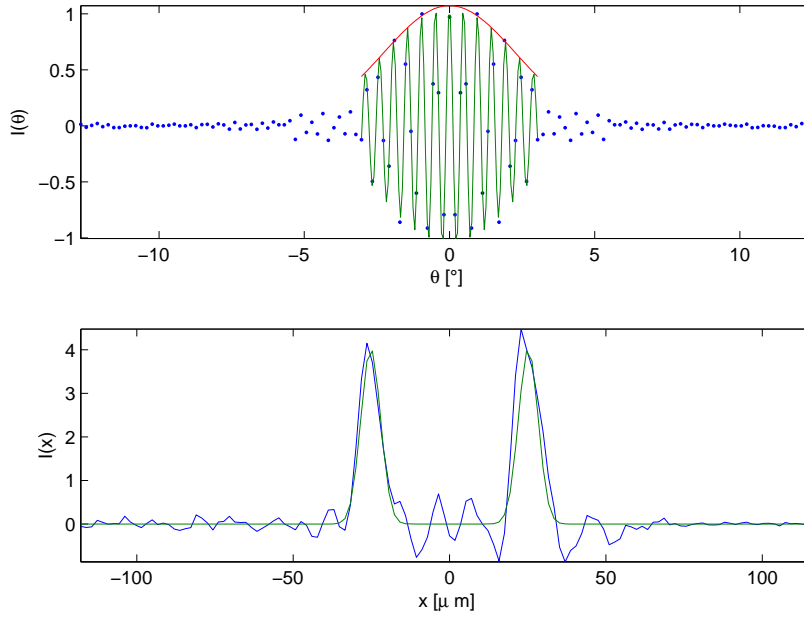


Figure 5.7: *Position extraction in Fourier space.* **top panel:** Fourier transform of the scattered intensity profile  $I(x)$ . The transverse wavevector  $k_x$  has been translated to the propagation angle of the corresponding plain wave component, measured relative to the plain wave direction. The green curve shows a fit of the model  $\cos k_x h \exp -k_x^2 w^2 / 4$  to the data. **bottom panel:** Scattered intensity profile  $I(x)$  together with the transform of the Fourier space fit (green line).

component the relative angle that the outwards propagating wave includes with the

illuminating plain wave can be computed by  $\theta = \arcsin k_x \lambda / 2\pi$ . For relative angles  $\theta$  that are small compared to the incident angle of the plain wave  $\theta_i$  the spectrum is well approximated by that of two Gaussian curves, separated by the distance  $2h$ . This spectrum is given by

$$I_{sc} \propto \cos k_x h \exp -k_x^2 w^2 / 4 \quad (5.12)$$

From a fit of this modulated Gaussian model, the distance  $h$  can be extracted, using only the small  $k_x$  component of the spectrum that is little affected by the aliasing problem of angles. Figure 5.8 shows a typical example of a scattered intensity profile  $I(x)$  and its Fourier transform. An alternative, but essentially equivalent way of extracting the height, proceeds by using the autocorrelation function of  $I(x)$ . This function is just the Fourier transform of the spectral power density  $|I(k)|^2$ . As the latter is well approximated by a modulated Gaussian, the correlation function can be fitted by a shifted Gaussian function. This formulation has been used for the height calibration in the magnetometry scans (see section 2.5.2).

In comparison to a simple evaluation of the center of mass position of the peaks corresponding to image and mirror image, the correlation method is significantly more stable. Figure 5.8 shows a direct comparison of these two methods. The

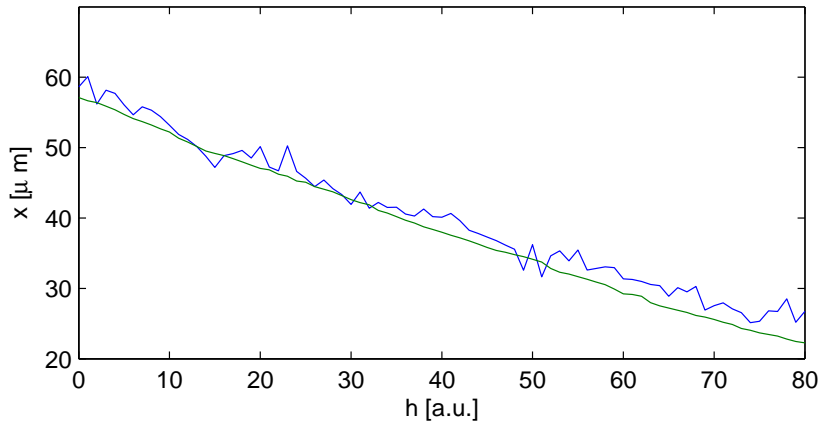


Figure 5.8: *Comparison of methods for the height estimation.* The blue curve has been obtained by taking the distance between the center of mass position of the image and mirror image. The green curve is the result of the Fourier space method. The height parameter  $h$  is an experimentally adjusted parameter that is nearly linear in the actual height.

height parameter  $h$  is an experimentally adjusted parameter that is nearly linear in the actual height. Histograms of the residuals obtained from a quadratic fit to the data are shown in figure 5.9. Both histograms follow a Gaussian distribution.

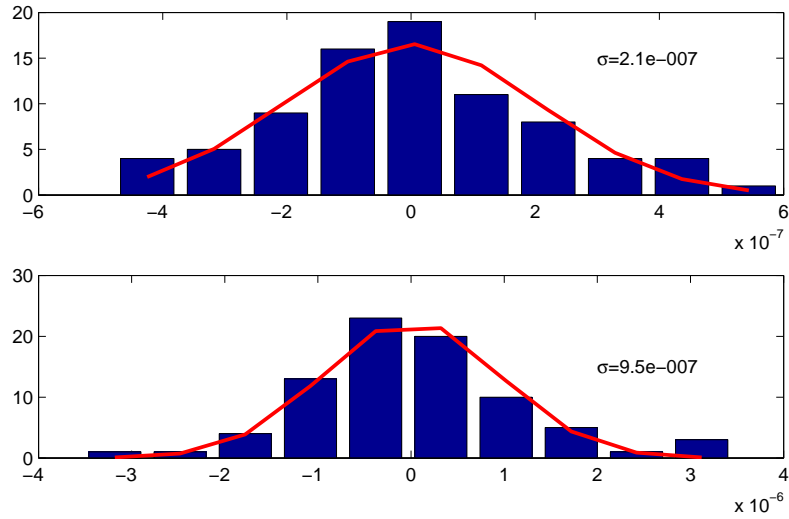


Figure 5.9: *Comparison of residuals.* The residuals are obtained from a quadratic least square fit to the data of figure 5.8 **top panel**: Residuals for the Fourier space analysis. **bottom panel**: Residuals for the center of mass based analysis.

However, the rms statistical uncertainty of a single height measurement is reduced from  $0.95\mu m$  for the center of mass based analysis to  $0.21\mu m$  for the correlation based analysis method. This clearly demonstrates the advantage of the presented scheme.

## 5.4 Appendix

### 5.4.1 Wavefront-Propagation

In free space, the propagation of an electromagnetic wave may be carried out most easily in Fourier space. The implementation will be presented here for the two dimensional case, the generalization to the 3D case is however obvious. The wavefront is assumed to be known in the plain  $z = 0$  and denoted there by

$E_0(x)$ . For a plain wave, the propagation is extremely simple. The wave

$$A_k e^{i(kx + \sqrt{\kappa^2 - k^2}z)} \quad (5.13)$$

fulfills the Helmholtz equation for  $\kappa = \frac{2\pi}{\lambda}$  and is therefore a valid wave function. As any wavefront can be decomposed into its plain wave contributions, the propagation of a general wave function can be formulated using this decomposition

$$E_z(x) = \frac{1}{\sqrt{2\pi}} \int dk E_0(k) e^{i(kx + \sqrt{\kappa^2 - k^2}z)} \quad (5.14)$$

It fulfills the Helmholtz equation and for  $z = 0$  reduces to the initial field  $E_0(x)$ . For the practical implementation, the Fourier transform can be evaluated using the FFT-algorithm.

### 5.4.2 Reflection by a Corrugated Mirror

A plain wave  $E = E_0 e^{-ik_0 z}$  that is incident on a mirror with small surface corrugations  $h(x)$  will acquire a phaseshift  $\Delta\phi(x) \approx \phi_0 + 2h(x)k_0$  during the reflection. The outgoing wave at  $z = 0$  is given by

$$E = E_0 e^{ik_0 z} a(x) \quad (5.15)$$

where  $a(x) = e^{i\Delta\phi(x)}$ . When propagated upwards from the surface, the phase modulation on the reflected wave leads to diffraction. At a distance  $z$  from the surface the field of the reflected wave is given by

$$E(x, z) = E_0 \int e^{i\sqrt{\kappa^2 - k^2}x} a(k - k_0) e^{-ikz} dk \quad (5.16)$$

, where  $\kappa = 2\pi/\lambda$ . Some care has to be taken when performing this diffraction integral under the special circumstances of grazing incidence. The spectrum of the surface phase profile  $a(k)$  will not be propagated out completely. As  $k_0$  is close to  $\kappa$ , a significant part of the spectrum is propagated as evanescent modes. For an observation point far from the surface, these modes can be neglected. The propagating field is given therefore in the  $z = 0$  plain by

$$E_r(x, z = 0) = E_0 \int_{-\kappa}^{\kappa} e^{i\sqrt{\kappa^2 - k^2}x} a(k - k_0) dk \quad (5.17)$$

In order to facilitate the numerical evaluation, the integral can be cast into the form a Fourier transform by the substitution  $k'^2 = \kappa^2 - k^2$

$$\begin{aligned} E_r(x) &= E_0 \int_0^\kappa dk' e^{ik'x} \frac{k'}{\sqrt{\kappa^2 - k'^2}} \\ &\times \left( a(-\sqrt{\kappa^2 - k'^2} - k_0) + a(-\sqrt{\kappa^2 - k'^2} - k_0) \right) \end{aligned} \quad (5.18)$$

# Bibliography

- [1] Fortagh, J. Zimmermann, C. Magnetic microtraps for ultracold atoms. *Rev. Mod. Phys.* **79**, 235 (2007)
- [2] Lin, Y. et al, Impact of the Casimir-Polder Potential and Johnson Noise on Bose-Einstein Condensate Stability Near Surfaces. *Phys. Rev. Lett.* **92**, 050404 (2004)
- [3] Obrecht, J.M. et al. Measurement of the Temperature Dependence of the Casimir-Polder Force. *Phys. Rev. Lett.* **98**, 063201 (2007)
- [4] McGuirk, J.M. et al. Alkali-metal adsorbate polarization on conducting and insulating surface probed with Bose-Einstein condensates. *Phys. Rev. A* **69**, 062905 (2004)
- [5] Wildermuth, S. et al. Microscopic magnetic-field imaging. *Nature* **435**, 440 (2005)
- [6] Jones, M.P.A. et al. Spin Coupling between Cold Atoms and the Thermal Fluctuations of a Metal Surface. *Phys. Rev. Lett.* **91**, 080401 (2003)
- [7] Schneider, S. et al. Bose-Einstein condensation in a simple microtrap. *Phys. Rev. A* **67**, 023612 (2003)

---

# 6 Magnetic Trapping and Spin Dynamics

---

## 6.1 Classical Motion of a Spin Particle

$^{87}\text{Rb}$  in the  $F = 2$  groundstate have a magnetic moment of  $m = g_F \mu_B$  which is intimately connected to the angular momentum  $\hbar F$  of the hyperfine state

$$\mathbf{m} = \mu_B g_F \mathbf{F} \tag{6.1}$$

In this equation  $\mu_B$  is the Bohr magneton and  $g_F = \frac{1}{2}$  the Lande factor for this specific ground state. When placing the atom into an external magnetic field, the magnetic moment can interact with the field by the usual dipole potential. For a single, atom the Hamiltonian including this interaction is given by [1]

$$H = \frac{p^2}{2M} - \mathbf{m} \cdot \mathbf{B} \tag{6.2}$$

The magnetic field dependent term acts in two ways on the dynamics of the atom. On the one hand it controls the evolution of the magnetic moment, which is the internal dynamics. On the other hand it acts as an effective potential for the center of mass motion. This interplay between the two aspects becomes clearer when the time evolution of the position and magnetic moment operators is considered within

the Heisenberg picture

$$\begin{aligned}\frac{d\mathbf{m}}{dt} &= \frac{i}{\hbar}[H, \mathbf{m}] = \mathbf{m} \times \Omega \\ \frac{d\mathbf{p}}{dt} &= \frac{i}{\hbar}[H, \mathbf{p}] = \nabla(\mathbf{m} \cdot \mathbf{B}) \\ \frac{d\mathbf{x}}{dt} &= \frac{i}{\hbar}[H, \mathbf{x}] = \frac{\mathbf{p}}{M}\end{aligned}\quad (6.3)$$

where  $\Omega = \frac{\mu_B g_F}{\hbar} \mathbf{B}$ .

For the first equation, the relation (6.4) and the usual angular momentum commutation rules

$$[F_x, F_y] = iF_z; [F_z, F_x] = iF_y; [F_y, F_z] = iF_x$$

have been used. The center of mass equations use the momentum position commutator  $[\mathbf{x}, \mathbf{p}] = i\hbar$  and  $[\mathbf{m}, \mathbf{p}] = 0$ .

Taking the expectation values of each equation a closed system for the evolution of the center of mass and the magnetic moment can be obtained

$$\begin{aligned}\frac{d \langle \mathbf{m} \rangle}{dt} &= \langle \mathbf{m} \rangle \times \Omega \\ \frac{d^2 \langle \mathbf{x} \rangle}{dt^2} &= \frac{1}{M} \nabla \langle \mathbf{m} \rangle \cdot \mathbf{B}\end{aligned}\quad (6.4)$$

It has to be mentioned that the existence of a closed system of equations for the expectation values is non trivial. This property makes it possible to treat the reduced dynamics in the way of a classical system.

In the equations (6.4) magnetic moment and center of mass are still linked in a very complicated way. The evolution of the magnetic moment depends on the center of mass trajectory as the movement goes through regions of changing magnetic field. On the other hand, the orientation of the magnetic moment sets the sensitivity of the effective potential

$$V(\mathbf{x}, t) = - \langle \mathbf{m}(t) \rangle \cdot \mathbf{B}(\mathbf{x}, t) \quad (6.5)$$

to the magnetic field. In order to use the magnetic interaction for the control of the center of mass motion a situation has to be achieved where the effective potential becomes independent of the history of the motion and where it is only a function of the momentary local state of the magnetic field

$$V(\mathbf{x}, t) \stackrel{!}{=} - \langle \mathbf{m}(\mathbf{B}) \rangle \cdot \mathbf{B}(\mathbf{x}, t) \quad (6.6)$$

## 6.2 The effective potential

### 6.2.1 Adiabatic Potential

The most simple case where a decoupling of the spin from the center of mass motion is possible, is that of a constant magnetic field  $\mathbf{B} = B_0 \mathbf{n}$ , where  $\mathbf{n}$  is a unit vector that indicates the direction of the field vector. The spin evolution of such a system is described by a pure rotation around the constant magnetic field direction. The effective potential for this case can be computed equally easily in the classical and the quantum picture.

The expectation value of the magnetic moment describes according to equation (6.4) a rotation around the magnetic field axis at the angular frequency  $\omega_L$ . During this rotation, the projection of the magnetic moment onto the field axis does not change

$$\frac{d \langle \mathbf{m} \rangle \cdot \Omega}{dt} = (\langle \mathbf{m} \rangle \times \Omega) \cdot \Omega = 0 \quad (6.7)$$

the effective potential is therefore constant

$$V = - \langle \mathbf{m} \rangle_0 \cdot \mathbf{B} \quad (6.8)$$

where  $\langle \mathbf{m} \rangle_0$  is the initial value. The same situation can be analyzed in the quantum mechanical picture. The time evolution of any operator  $O$  may be calculated from the time evolution operator  $U$  by  $O(t) = U(t, t_0)^\dagger O(t_0) U(t, t_0)$ . This operator is calculated from

$$i \frac{dU}{dt} = \frac{1}{\hbar} H U = -\mathbf{F} \cdot \Omega U \quad (6.9)$$

For the case of a constant magnetic field this equation can be directly integrated by the exponential

$$U(t, t_0) = \exp(i\mathbf{F} \cdot \Omega t) = \exp(i\mathbf{F} \cdot \mathbf{n} \omega_L t) \quad (6.10)$$

. Also a pure change of the field magnitude makes no major difference. Only the acquired phase  $\omega_L t$  has to be replaced by an integral

$$U(t, t_0) = \exp\left(i\mathbf{F} \cdot \mathbf{n} \int_{t_0}^t dt' \omega_L(t')\right) \quad (6.11)$$

Like in the classical case, this evolution operator performs a rotation around the magnetic field axis  $\mathbf{n}$  with the angular velocity  $\omega_L$  [2].

Difficulties start to arise when the direction of the magnetic field changes with time. The adiabatic approximation [3] handles this case in the limit of a slowly changing direction. The idea is to consider the spin evolution in a co-moving coordinate frame where the  $z$  axis is always aligned with the momentary magnetic field direction. This picture can be expressed by describing the spin Hamiltonian as the combined action of a rotation  $R$  and the Lamor precession in the rotating frame

$$\omega_L(t)\mathbf{F} \cdot \mathbf{n}(t) = \omega_L(t)R^\dagger(t)F_zR(t) \quad (6.12)$$

the spin evolution in the co moving frame is then described by  $U' = RUR^\dagger$  according to

$$\begin{aligned} i\frac{dU'}{dt} &= \omega_L(t)F_zU' + i\left(\frac{dR}{dt}R^\dagger U' + U'R\frac{dR^\dagger}{dt}\right) \\ &= \omega_L(t)F_zU' + i\left[\frac{dR}{dt}R^\dagger, U'\right] \end{aligned} \quad (6.13)$$

The adiabatic limit is the case where the commutator can be neglected. This is justified as long as the angular velocity associated with the rotation of the coordinate axis  $\omega_C$  is small compared to the Lamor frequency. To see this one can assume that the rotation of the coordinate frame can be described for a small time interval by a constant angular velocity  $\mathbf{n}_C\omega_C$ . The derivative term of the rotation matrix is then given by

$$i\frac{dR}{dt}R^\dagger = \omega_C\mathbf{n}_c \cdot \mathbf{F} \quad (6.14)$$

. This term makes a small contribution as long as  $\frac{\omega_C}{\omega_L} \ll 1$ .

In the adiabatic limit, the projection of the magnetic moment on the instantaneous magnetic field stays constant.

$$V = \langle \mathbf{m} \rangle \cdot \mathbf{B}(\mathbf{x}, t) \quad (6.15)$$

This relation decouples the spin evolution from the center of mass motion, that is an explicit function of position and time.

## 6.2.2 Floquet Potential

An additional degree of freedom for the effective potential can be introduced by using a periodic magnetic field

$$\mathbf{B}(t + T) = \mathbf{B}(t) \quad (6.16)$$

Similar to the quasi-momentum conservation in a potential that is periodic in space, there exists a conserved quasi energy for the time periodic case. The states that correspond the Bloch-states in the spatially periodic case are the Floquet states in the time periodic case.

In Floquet theory, the time is not treated as a parameter but on the same footing as the other coordinates. One defines the Hamiltonian [5]

$$\mathcal{H} = i \frac{d}{dt} + \mathbf{F} \cdot \Omega \quad (6.17)$$

This operator on the product space of time and spin coordinates is again Hermitian. In analogy to the stationary states of a time independent Hamiltonian there exist the so called Floquet states  $\phi_n(t)$  that are the eigenfunctions to  $\mathcal{H}$

$$\left( i \frac{d}{dt} + \mathbf{F} \cdot \Omega \right) \phi_n(t) = \frac{\epsilon_n}{\hbar} \phi_n(t) \quad (6.18)$$

The  $\phi_n$  form an orthogonal basis and are periodic  $\phi_n(t+T) = \phi_n(t)$ . Each of these functions corresponds to a solution

$$\Psi_n(t) = \phi_n(t) e^{-\frac{i}{\hbar} \epsilon_n t} \quad (6.19)$$

of the Schrödinger equation. As  $\phi_n(t)$  is periodic  $\Psi_n(t)$  and  $\Psi_n(t+mT)$  only differ by a phase factor. Any expectation value calculated on such a state and especially the magnetic moment will be periodic functions. If the period  $T$  is small compared to the typical time scales associated with the center of mass motion of the atom, only the average value of the effective potential has an effect on it. For a Floquet state  $\phi_n$  this average potential can be obtained from the quasienergy  $\epsilon_n$  by [7]

$$\begin{aligned} \bar{V}_n &= \frac{1}{T} \int_{t_0}^{t_0+T} dt' \langle \Psi_n(t') | \mathbf{m} | \Psi_n(t') \rangle \cdot \mathbf{B}(t') \\ &= \epsilon_n(\omega) - \omega \frac{\partial \epsilon_n(\omega)}{\partial \omega} \end{aligned} \quad (6.20)$$

This relation allows a simple application of the Floquet formalism to the computation of effective potentials.

There are two possible routes towards the computation of the quasienergies. The classical strategy [6] is to expand the periodic Floquet states into its Fourier modes. This results into an eigenvalue equation for an infinite dimensional matrix which can be treated by the standard techniques of time independent perturbation theory. However, for the numerical evaluation the matrices have to be truncated in some way. Such a truncation in Fourier space can introduce badly controllable errors. Therefore a time domain approach following [8] will be used here for practical applications. It

relies on the property that Floquet states may be obtained as eigenvectors to the single period time evolution operator

$$U(t_0 + T, t_0)\Psi_n(t_0) = \Psi_n(t_0 + T) = \Psi_n(t_0)e^{-\frac{i}{\hbar}\epsilon_n T} \quad (6.21)$$

. The following section shows how this relation may be conveniently implemented.

### 6.2.3 Computation of quasi energies

If no analytic solution for the single period time evolution operator is known, a simple quasi analytical method that approximates the time dependence of the magnetic field by piecewise constant sections can be applied.

As has been shown above, the evolution in a constant magnetic field is given by

$$U(t_2, t_1) = \exp[i\mathbf{F} \cdot \mathbf{n}\omega_L(t_2 - t_1)] \quad (6.22)$$

A time dependent field may be approximated by piecewise constant parts within the time intervals  $[t_n; t_{n+1}]$  of the subdivided period  $t_n = \frac{n}{N}T$  and  $n = 0 \dots N - 1$

$$\begin{aligned} \omega_L(t) &\approx \frac{\omega(t_{n+1}) + \omega(t_n)}{2} \text{ for } t_n < t < t_{n+1} \\ \mathbf{n}(t) &\approx \frac{\mathbf{n}(t_{n+1}) + \mathbf{n}(t_n)}{|\mathbf{n}(t_{n+1}) + \mathbf{n}(t_n)|} \text{ for } t_n < t < t_{n+1} \end{aligned} \quad (6.23)$$

The corresponding approximation of the time evolution is then given by the product of the single time-interval operators

$$U(T, 0) = \prod_{n=0}^{N-1} \exp\left[i\mathbf{F} \cdot \mathbf{n}(t_n)\omega_L(t_n)\frac{T}{N}\right] \quad (6.24)$$

In comparison to standard integration schemes for differential equations, this approach has the large advantage that the approximated time evolution is by construction unitary.

If only the eigenvalues and the quasi energies shall be calculated the particular dimension of the specific spin state is unimportant. The single period evolution operator is itself as a product of successive rotations a rotation operator. In the Eigen system of this operator it has therefore the form

$$U(T, 0) = \begin{pmatrix} e^{iF\phi} & & & \\ & e^{i(F-1)\phi} & & \\ & & \ddots & \\ & & & e^{-iF\phi} \end{pmatrix} \quad (6.25)$$

The angle  $\phi$  itself depends not on a specific spin system. This makes it possible to calculate it for the simplest possible case namely for a spin 1/2 particle. From a knowledge of the trace alone  $\phi$  can be calculated by

$$\phi = 2 \arccos \left( \frac{1}{2} \text{Tr} \left[ U_{\frac{1}{2}}(T, 0) \right] \right) \quad (6.26)$$

This angle is related to the quasi energies of the  $F = 2$  case by

$$\epsilon_{m_F} = m_F \frac{\hbar \phi}{T} \quad (6.27)$$

For calculations within the spin 1/2 system the spin matrices are given explicitly by

$$S_x = \frac{1}{2} \begin{pmatrix} 0 & 1 \\ 1 & 0 \end{pmatrix} \quad S_y = \frac{1}{2} \begin{pmatrix} 0 & -i \\ i & 0 \end{pmatrix} \quad S_z = \frac{1}{2} \begin{pmatrix} 1 & 0 \\ 0 & -1 \end{pmatrix} \quad S_0 = \frac{1}{2} \begin{pmatrix} 1 & 0 \\ 0 & 1 \end{pmatrix} \quad (6.28)$$

where the matrix  $S_0$  has been included additionally as this set of matrices is an orthogonal basis for all  $2 \times 2$  matrices. The expansion coefficients for an arbitrary matrix  $m$  can be calculated as

$$m = 2 \sum_{i=0,x,y,z} \text{Tr}[S_i m] S_i \quad (6.29)$$

## 6.2.4 Resonant Rf Potential

The paradigm for a non trivial cyclic spin evolution is the nuclear magnetic resonance (NMR) configuration. In this situation a static magnetic field induces a Larmor precession around the field axis. A small second field that is applied periodically perpendicular to the static field is able to rotate the precessing spin around its own axis if the rotation is applied in phase with the Larmor precession. This phase matching condition produces a resonant behavior in the coupling to the time dependent field and introduces an independent parameter to influence the effective potential.

The magnetic field consists of a static part  $\mathbf{B}_0 = B_0 \mathbf{e}_z = \beta \frac{\hbar}{g_F \mu_B} \mathbf{e}_z$  along the  $z$ -direction and a harmonic circular polarized field in the  $x - y$  plain

$$\Omega(t) = \beta (\mathbf{e}_x \cos \omega t - \mathbf{e}_y \sin \omega t) + \omega_0 \mathbf{e}_z \quad (6.30)$$

The classic solution [4] for the spin evolution caused by this field uses a co-moving frame that rotates together with the circular polarized field around the  $z$  axis. The rotation

$$U' = e^{-i\omega t F_z} U e^{i\omega t F_z} \quad (6.31)$$

transforms the spin equation into

$$i \frac{dU'}{dt} = - \left( e^{-i\omega t F_z} \Omega(t) \cdot \mathbf{F} e^{i\omega t F_z} - \omega \mathbf{e}_z \right) U' = - (\Omega' - \omega \mathbf{e}_z) \cdot \mathbf{S} U' \quad (6.32)$$

where

$$\Omega' = \beta \mathbf{e}_x + (\omega_0 - \omega) \mathbf{e}_z \quad (6.33)$$

. In the co-rotating frame the time evolution is given by an effective constant magnetic field. The complete single period time evolution in the non-rotating frame is then given by

$$U(T) = e^{-i\omega S_z T} \exp [i\Omega' \cdot \mathbf{S} T] e^{i\omega S_z T} \quad (6.34)$$

from which the rotation angle

$$\phi = |\Omega'| T = \sqrt{\beta^2 + (\omega - \omega_0)^2} T \quad (6.35)$$

and the quasienergy

$$\epsilon_m = m_F \hbar \sqrt{\beta^2 + (\omega - \omega_0)^2} \quad (6.36)$$

are obtained. Finally the mean potential can be extracted

$$\bar{V} = \epsilon - \frac{\partial \epsilon}{\partial \omega} = m_F \hbar \frac{\beta^2 - \omega_0 (\omega - \omega_0)}{\sqrt{\beta^2 + (\omega - \omega_0)^2}} \quad (6.37)$$

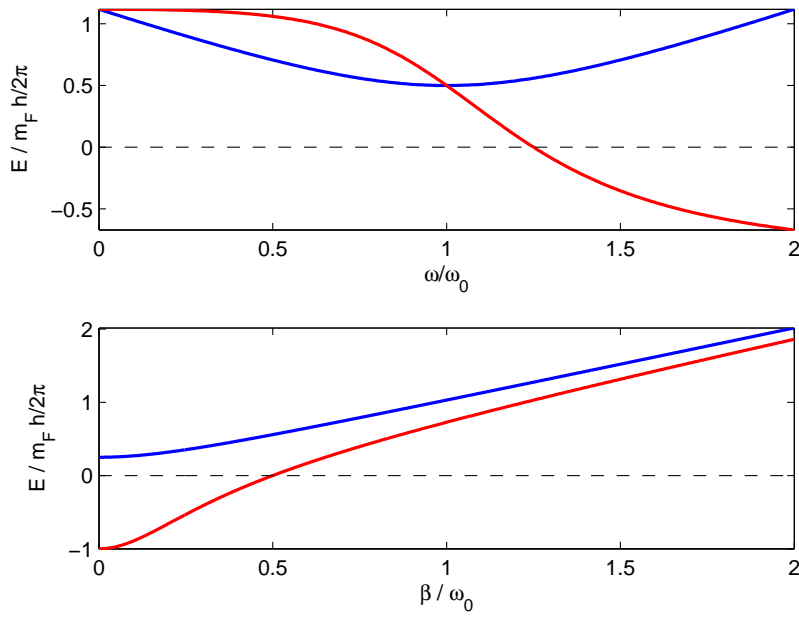
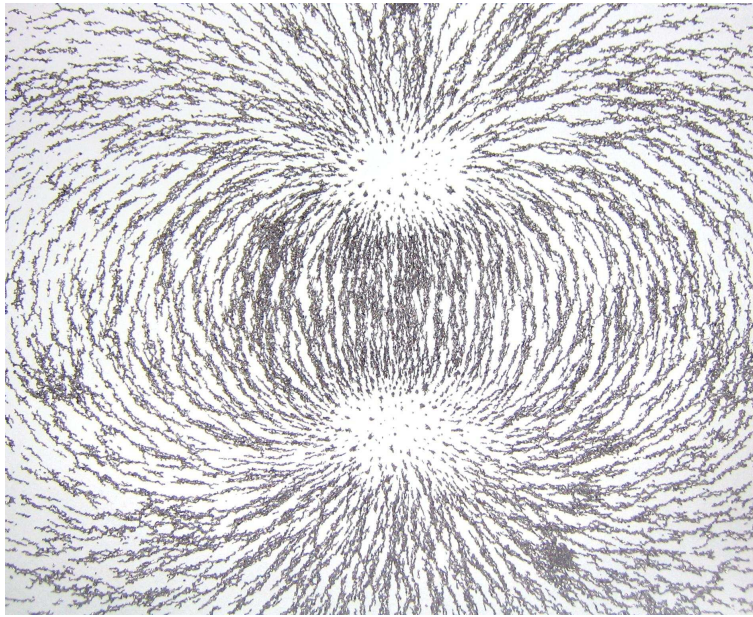


Figure 6.1: *Comparison of quasi energy and mean energy:* The curves show the dependence of quasienergy (blue lines) and mean potential (red lines) on the rf-frequency (top panel) and rf-amplitude (bottom panel). All energies are converted to an angular frequency by the normalization factor  $1/m_F\hbar$

## 6.3 Gradient Fields On An Atom Chip

The idea behind integrated wire traps is to use the high gradient magnetic fields close to thin wires to provide a strong trapping force and flexible design. On an atom chip such wires are integrated by a micro-structured gold film on a silicon waver. The two dimensional symmetry that is enforced by the chip geometry induces certain restrictions for the magnetic field.

### 6.3.1 Symmetries the field



The magnetic field outside a current distribution has zero divergence and curl. From the latter it follows, that the field can be derived from a scalar magnetic potential

$$\mathbf{B} = -\nabla\phi_M \quad (6.38)$$

The zero divergence condition implies a Laplace equation for the magnetic potential

$$\nabla^2\phi_M = 0 \quad (6.39)$$

In order to characterize those field configurations that are possible close to a minimum in the absolute field value  $\mathbf{B}$ , the potential and magnetic field will now be expanded into a power series.

As the magnetic potential fulfills the Laplace equation it can be approximated locally by a combination of spherical Harmonics [9, 10, 11]

$$\phi_M = \sum_{l=0} \sum_{m=-l}^l c_{lm} Y_{lm}(\theta, \phi) r^l \quad (6.40)$$

each term  $r^l Y_{lm}(\theta, \phi)$  fulfills the Laplace equation separately and therefore also the total sum. Using this expansion the magnetic field may be written as

$$\mathbf{B} = \sum_{l=0} \sum_{m=-l}^l c_{lm} \nabla \left( Y_{lm}(\theta, \phi) r^l \right) \quad (6.41)$$

This expansion still contains modes that are not allowed in a current free region of space. The reason is that despite the property

$$\nabla \times \mathbf{B} = 0 \quad (6.42)$$

is fulfilled by construction, the stronger integral form

$$\int_C d\mathbf{s} \cdot \mathbf{B} = 0 \quad (6.43)$$

where the integral runs over a closed curve that includes no current is not necessarily fulfilled yet. For a circle of radius  $r$  around the origin in the  $x - y$  plain reads

$$\begin{aligned} \int d\mathbf{s} \cdot \nabla \left( Y_{lm}(\theta, \phi) r^l \right) &= r^{l+1} \int_0^{2\pi} d\phi \frac{\partial}{\partial \phi} Y_{lm}(\theta, \phi) \\ &= r^{l+1} 2\pi m \sqrt{\frac{2l+1}{4\pi} \frac{(l-m)!}{(l+m)!}} P_l^m(\cos \theta) \end{aligned} \quad (6.44)$$

apart from the case  $m = 0$  the integral does not vanish. However as the expression is antisymmetric with respect to  $m$  an expansion in terms of the symmetrized modes

$$\mathbf{Z}_{lm}(\theta, \phi) r^l = \nabla \left[ r^l \frac{1}{2} (Y_{lm}(\theta, \phi) + Y_{l-m}(\theta, \phi)) \right] \quad (6.45)$$

$$\mathbf{B} = \sum_{l=0} \sum_{m=0}^l s_{lm} \mathbf{Z}_{lm}(\theta, \phi) r^l \quad (6.46)$$

will also respect the zero curl condition in its integral form. The first two non-constant sets  $l = 2$  and  $l = 3$  are tabulated in table (6.1) in cartesian coordinates.

$l$	$m$	$\mathbf{Z}_{lm}(\theta, \phi)r^l$
2	2	$x\mathbf{e}_x - y\mathbf{e}_y$
	1	$x\mathbf{e}_z + z\mathbf{e}_x$
	0	$2z\mathbf{e}_z - x\mathbf{e}_x - y\mathbf{e}_y$
3	3	$(x^2 - y^2)\mathbf{e}_x - 2xy\mathbf{e}_y$
	2	$2xz\mathbf{e}_x - 2yz\mathbf{e}_y + (x^2 - y^2)\mathbf{e}_z$
	1	$(-3x^2 - y^2 + 4z^2)\mathbf{e}_x - 2xy\mathbf{e}_y + 8xz\mathbf{e}_z$
	0	$(z^2 - \frac{1}{2}(x^2 + y^2))\mathbf{e}_z - zx\mathbf{e}_x - zy\mathbf{e}_y$

Table 6.1: Expansion polynomials for the magnetic field.

In the design of atom chip potentials it is very convenient to think of the separate action of different current density components. For the plain geometry of an atom chip, the current is restricted to only two current components in the chip plane. This plane is assumed to be the  $x - y$  plain. As can be seen from

$$\nabla^2 \mathbf{B} = \mu_0 \nabla \times \mathbf{j} \quad (6.47)$$

the current component along the  $x$ -direction can produce a field that has  $y$  and  $z$  components and a current density along the  $y$  direction will result into  $x$  and  $z$  components of the magnetic field.

In the polynomial expansion of a field due to an unidirectional current density along the  $x$  direction  $\mathbf{j} = j_x \mathbf{e}_x$  only two different types of modes can make a contribution.

$l$	$ m $	$\mathbf{Z}_{lm}(\theta, \phi)r^l$
2	2	$r(\cos \phi \mathbf{e}_y - \sin \phi \mathbf{e}_z) \quad   \quad y\mathbf{e}_y - z\mathbf{e}_z$
3	3	$r^2(\cos 2\phi \mathbf{e}_y - \sin 2\phi \mathbf{e}_z) \quad   \quad (y^2 - z^2)\mathbf{e}_y - 2yz\mathbf{e}_z$

## 6.4 The Stern Gerlach Beam Splitter

In their seminal 1922 paper [12] Stern and Gerlach experimentally verified the spin quantization. In their experiment, a beam of unpolarized, thermal silver atoms has been split by the strong gradient of a permanent magnet into two clearly separated beams. Where as this experiment showed the existence of a discrete internal degree of freedom, it does not directly proof that this splitting process is coherent. The outcome is the same for an incoherent mixture of particles and a beam that is coherently prepared in a superposition state. In this section, the result of an experiment is presented, where a succession of two orthogonal stern Gerlach splittings is used to implement an interferometer that uses the spin degree of freedom. The observed interference contrast directly proofs, that the Stern-Gerlach experiment presents a coherent beam splitter.

The complete state of an atom in the  $F = 2$  ground-state can be described by a product wavefunction of center of mass state  $\phi(z)$  and the spin state  $|\chi\rangle$

$$\psi(z) = \phi(z)|\chi\rangle \quad (6.48)$$

If a wavepacket, that has been initially prepared in the  $m_F = 2$  state is exposed to a gradient field  $\mathbf{B}(z) = gz\mathbf{e}_y$  which is polarized orthogonally to the z-direction in which the spin polarization points the spin starts to rotate locally around the y-direction. After a certain time  $T$ , that is assumed to be small compared to the time scale of any center of mass motion, a spatial gradient in the rotation angle  $\gamma_y = \alpha z$  has been imprinted on the wavepacket

$$\psi(T, z) = \phi(z) \begin{pmatrix} \cos^4 \gamma_y/2 \\ 1/2(1 + \cos \gamma_y) \sin \gamma_y \\ 1/2\sqrt{3/2} \sin \gamma_y^2 \\ 2 \cos \gamma_y/2 \sin^3 \gamma_y/2 \\ \sin^4 \gamma_y/2 \end{pmatrix} \quad (6.49)$$

When expanding the different harmonic functions into exponentials it can be seen that each component of the wavefunction is a superposition of five different wavepackets that each have a different linear phase imprint. For the  $m_F = 2$  component for example, the explicit form is given by

$$\psi_2(z) = \phi(z) \frac{1}{16} (e^{i2\alpha z} + 4e^{i\alpha z} + 6 + 4e^{-i\alpha z} + e^{-i2\alpha z}) \quad (6.50)$$

After an appropriate time-span of free evolution, the different momentum components separate and give rise to the typical Stern-Gerlach splitting. Interestingly, the

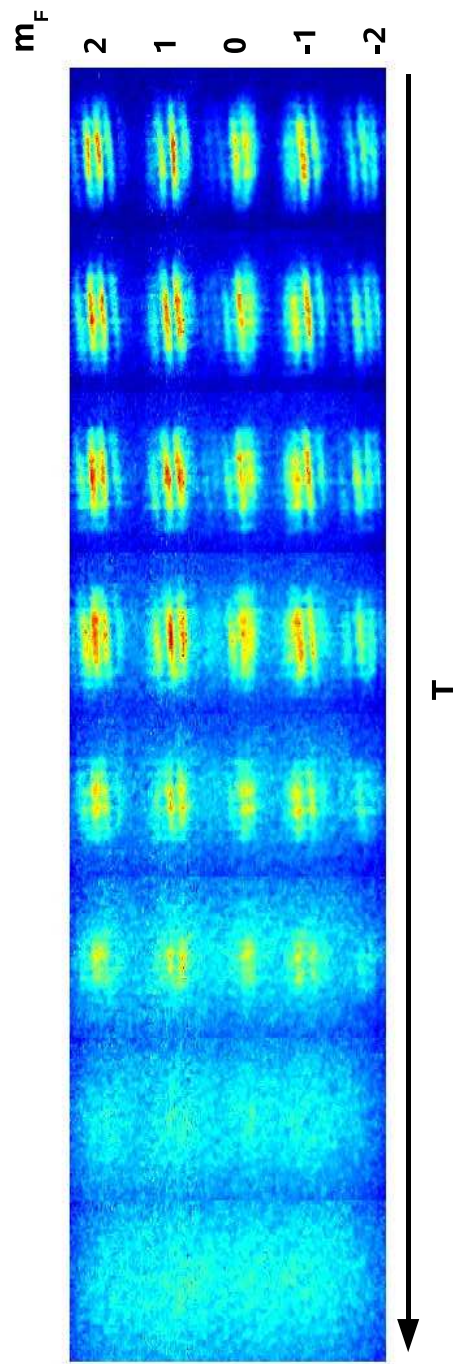


Figure 6.2: *Stern-Gerlach interferometry with Thermal atoms and condensates.* Implementation of the double Stern-Gerlach pulse scheme described in the text, for different cloud temperatures. The interference contrast vanishes with increasing temperature.

separated momentum components do not directly map to the spin components of the original state. Each of the  $m_F$  components is a superposition of five different momentum states. By the expansion process, the state is projected onto the momentum eigenstates, which are not at the same time spin eigenstates.

The local spin rotation can however be visualized not only in momentum space, but also directly in real space. For this purpose two gradient pulses are applied. The first induces a small spin rotation where the associated momentum transfer is very small compared to that of the second pulse. The second pulse has a magnetic field that is orthogonal to the first, which converts the spin rotation to an amplitude modulation in the basis of this second pulse. After an interval of free expansion, the amplitude modulated  $m_F$  components are separated in real space.

An experimental realization of this scheme is shown in figure 6.2. The same pulse scheme has been applied to clouds of different temperature from above, to below the critical temperature. It can be clearly observed that below the transition temperature, typical interference fringes appear on each of the separated components. The phase gradient of these modulations directly relates to the gradient in the angle of the spin rotation, induced by the first pulse.

# Bibliography

- [1] Pauli,W. Zur Quantenmechanik des magnetischen Elektrons. *Z. Phys. A* **43**, 601 (1927)
- [2] Sakurai,J.J. Modern Quantum Mechanics *The Benjamin/Cummings Publishing Company Inc., Menlo Park, California* ISBN 0-8053-7501-5 (1985)
- [3] Born,M. Fock,V. Beweis des Adiabatenatzes. *Z. Phys. A* **51**, 165 (1928)
- [4] Rabi,I.I. Ramsey,N.F. Schwinger,J. Use of Rotating Coordinates in Magnetic Resonance Problems. *Rev. Mod. Phys.* **26**, 167 (1954)
- [5] Sambe,H. Steady States and Quasienergies of a Quantum-Mechanical System in an Oscillating Field. *Phys. Rev. A* **7**, 2203 (1973)
- [6] Shirley,J.H. Solution of the Schrödinger Equation with a Hamiltonian Periodic in Time. *Phys. Rev.* **138**, B979 (1965)
- [7] Grifoni,M. Hänggi,P. Driven quantum tunneling. *Phys. Rep.* **304**, 229 (1997)
- [8] Grondalski,J. Alsing,P.M. Deutsch,I.H. Phase diffusion as a model for coherent suppression of tunneling in the presence of noise. *Phys. Rev. E* **63**, 016114 (2000)
- [9] Gray,C.G. Simplified derivation of the magnetostatic multipole expansion using the scalar potential. *Am. J. Phys.* **46**, 582 (1978)
- [10] Gray,C.G. Multipole expansion of electromagnetic fields using Debye potentials. *Am. J. Phys.* **46**, 169 (1978)
- [11] Barrera,R.G. Estevez,G.A. Giraldo,J. Vector spherical harmonics and their application to magnetostatics. *Eur. J. Phys.* **6**, 287 (1985)
- [12] Gerlach,W. Stern,O. Der experimentelle Nachweis der Richtungsquantelung im Magnetfeld. *Z. Phys.* **9**, 25 (1922)



# Acknowledgements

I acknowledge financial support through the Graduiertenförderung of the state Baden-Württemberg and the German-Israeli project of the German Federal Ministry of Education and Research (BMBF-DIP).

I want to thank Yonathan Jaffa for the fruitful collaboration, the interesting discussions and that he was always willing to enter, as a theorist, into the gory details of experimental grass root work.

Many thanks also to the clean room staff, who implemented the sample chip with an excellent precision and to all the people in Ron Folman's group who have worked together with me on this project.

I want to especially thank Leonardo Della Pietra, who shared good and bad times at the experiment with me.

I want to thank Christoph von Hagen for general assistance as a friend and for always having an open ear for solid physical discussions.

Many thanks to Mauritz Anderson who introduced me to the power of FFt for wave propagation problems.

I want to thank my supervisor Jörg Schmiedmayer for his patience and that he gave me free access to a setup and the equipment that allowed me to delve into some of the most fascinating facets of nature.

Most important, I want to thank my wife Katja and my daughter Amelie for their love, the continued endurance of much too long working hours and for keeping me in contact with the real world.